Editorial corner – a personal view
Hype about High Internal Phase Emulsion templating: Adding particles makes all the difference
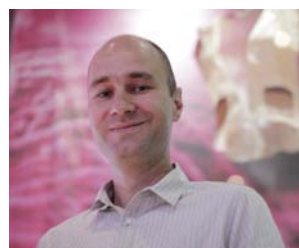
A. Bismarck[*]

Polymer & Composite Engineering (PaCE) Group, Department of Chemical Engineering, Imperial College London, South Kensington Campus, London, SW7 2AZ, UK

High porosity, interconnected porous polymers are attractive materials for numerous applications from supports for cell cultures, solid-state chemistry and setting retarded cements. Macroporous polymers can be prepared by various methods, such as chemical and physical blowing, but also by emulsion templating; first reported by von Bonin and Bartl in 1962 (DOI: 10.1002/macp.1962.020570105), emulsion templating has now emerged as effective method to synthesise porous polymers with tailored pore morphology and physical properties. High or Medium Internal Phase Emulsions (H/MIPEs) with a continuous phase consisting of or containing monomers are used as templates for the preparation of interconnected macroporous polymers, called poly(merised)M/HIPEs. PolyH/MIPEs are synthesised from emulsion templates stabilised by large amounts of surfactants. The resulting polymers are interconnected and have porosities of up to 99%. However, applications of polyHIPEs remain limited mainly because of their poor mechanical properties but also their low permeability. In the last decade much research focused on improving the mechanical properties, which was achieved by incorporating reinforcements, increasing the foam density or by using different monomers and polymerisation routes. Improving the permeability of porous polymers while maintaining sufficient mechanical properties was more challenging; increasing the porosity of interconnected porous polymers results in higher permeability but lower mechanical properties. Maximum pore throat sizes of polyM/HIPEs produced from surfactant stabilised emulsion templates are limited, which also limits the permeability.

We introduced a new class of porous polymers called poly-Pickering-M/HIPEs, produced from particle stabilised (Pickering) M/HIPEs. These porous polymers have pore sizes of up to 1.5 mm and porosities of up to 90% (DOI: 10.1039/B708935J) but are typically closed-cell. However, this new class of polyHIPEs with large pores should allow for very permeable polyHIPEs if the pores could be made interconnected. This was possible by introducing a surfactant to pre-made Pickering emulsion templates (DOI: 10.1002/adma.201000729). The resulting open-porous poly-Pickering-HIPEs had a maximum gas permeability of 2.6 Darcy. Alternatively, if particles and surfactant were simultaneously used as emulsifiers, porous polymers with a hierarchical pore structure with enhanced mechanical properties and high permeability were produced (DOI: 10.1002/marc.201100382).

Now that we have a tool kit for new polyM/HIPE architectures, we believe that this can be combined with different polymer chemistries to produce a whole raft of novel interconnected porous polymers. By selecting appropriate particulate emulsifiers we could create functional porous polymers, which by virtue of the liquid template can be given any shape making this a versatile approach for the future.

Prof. Dr. Alexander Bismarck
Member of the International Advisory Board

[*]Corresponding author, e-mail: a.bismarck@imperial.ac.uk

High performance polyethylene nanocomposite fibers

M. D'Amato, A. Dorigato[*], L. Fambri, A. Pegoretti

University of Trento, Department of Materials Engineering and Industrial Technologies and INSTM Research Unit, Via Mesiano 77, 38123 Trento, Italy

Abstract. A high density polyethylene (HDPE) matrix was melt compounded with 2 vol% of dimethyldichlorosilane treated fumed silica nanoparticles. Nanocomposite fibers were prepared by melt spinning through a co-rotating twin screw extruder and drawing at 125°C in air. Thermo-mechanical and morphological properties of the resulting fibers were then investigated. The introduction of nanosilica improved the drawability of the fibers, allowing the achievement of higher draw ratios with respect to the neat matrix. The elastic modulus and creep stability of the fibers were remarkably improved upon nanofiller addition, with a retention of the pristine tensile properties at break. Transmission electronic microscope (TEM) images evidenced that the original morphology of the silica aggregates was disrupted by the applied drawing.

Keywords: nanocomposites, high density polyethylene, fibers, silica

1. Introduction

In the last two decades it has been widely proven that the mechanical properties (such as elastic modulus, strength, fracture toughness, creep stability and fatigue resistance) of various polymeric matrices can be remarkably improved through the addition of very small amounts (less than 5 wt%) of nanostructured fillers [1]. In particular, a substantial improvement of the thermo-mechanical properties of polymer matrices has been reached by the introduction of high aspect ratio fillers, such as carbon nanotubes [2–4] and layered silicates [5–10]. Compared to the extended literature concerning these kinds of nanofillers, relatively few attention has been devoted to nanocomposites filled with metal oxide nanoparticles, such as fumed titania [11, 12] and fumed silica [13–15]. For instance, Chaichana *et al.* [16] developed a novel route to synthesize linear low density polyethylene (LLDPE)/nanosilica systems via *in situ* polymerization with a zirconocene/methyl alumoxane (MAO) catalyst, in order to study the effect of particle size on the cat-

alytic properties of the resulting materials. The effect of silica and zirconia nanoparticles on the microstructure of LLDPE nanocomposites synthesized via *in situ* polymerization with zirconocene was investigated by Jongsomjit *et al.* [17], while Wang *et al.* [18] analyzed the dispersion behaviour of titania (TiO$_2$) nanoparticles in polyolefin nanocomposites.

In recent years an extended investigation was carried out by this research group on the viscoelastic and the fracture behavior of polyolefin based nanocomposites [19–23]. It was found that the addition of small quantities of fumed silica nanoparticles could substantially improve both the failure properties and the creep stability of the investigated matrices. High-density polyethylene (HDPE) is a widely applied thermoplastic polymer, characterized by good tensile properties, flexibility, low cost and chemical resistance. For this combination of properties it is used in several industrial applications, such as piping systems, bags, bottles, ropes and fibers. The production of high stiffness and high strength

---

[*]Corresponding author, e-mail: andrea.dorigato@ing.unitn.it

polyethylene fibers has been one of the challenges for polymer scientist and engineers for a very long time [24, 25]. One possible way to obtain high performance polyethylene fibers is through melt spinning and subsequent drawing. However, the applications of such fibers have been often limited by their relatively poor creep resistance and low shear modulus and strength. Even if theoretical stress at break values of polyethylene fibers are very high (close to 25 GPa) [26], the strength of highly drawn PE is generally limited to around 1.0–1.3 GPa [27, 28]. Very recently, Toyobo company developed an innovative high strength melt spinning polyethylene fiber (Tsunooga®) with superior lightness and cut resistance, with tenacity of 14 cN/tex and specific gravity of 0.97 g/cm^3, corresponding to a tensile strength of 1.36 GPa. Moreover, it was recently found that the introduction of small amounts of layered silicates in polyethylene matrices may lead to substantial improvements of the mechanical performances of the resulting fibers, in terms of elastic modulus and tensile properties at break [29]. Many efforts were devoted by La Mantia and his group in the investigation of the influence of the elongational flow on the morphology of PE/clay nanocomposite drawn fibers [30]. It was demonstrated how an increase of the elastic modulus and of tensile strength with respect to the neat matrix could be obtained when elevated draw ratios are reached. The observed increase of the mechanical properties was related to the exfoliation and orientation of nanoplatelets induced by the applied flow. Mezghani *et al.* studied the effect of carbon nanotubes (CNT) added to linear low-density polyethylene nanocomposite fibers, prepared by melt extrusion and subsequent cold drawing [31]. The observed improvements of the tensile strength and fiber ductility were attributed to the alignment and distribution of CNT in the organic matrix. Ruan *et al.* [32] reported the use of multi-walled carbon nanotubes (MWCNT) to reinforce and toughen gel-spun ultra high molecular weight polyethylene (UHMWPE) fibers, evidencing some beneficial effects on the tensile strength and strain at break values. The authors explained how nanofiller alignment along the tensile draw direction induced a stronger interfacial load transfer at the interface, enhancing therefore the stiffness and tensile strength of the composite fibers.

Regarding the use of silica nanoparticles to reinforce polyethylene fibers, only Zhang *et al.* [33] recently reported on the morphological, adhesive and mechanical properties of UHMWPE/silica nanocomposite fibers. Nano-silica was able to promote lower crystal sizes and higher crystallinity with respect to the neat fibers, with a remarkable enhancement of their mechanical properties and beneficial effects on the interfacial adhesion with an epoxy matrix. In a preliminary work of this group [23], a high density polyethylene matrix was melt compounded with various untreated (hydrophilic) and surface treated (hydrophobic) fumed silica nanoparticles, having different surface areas. The homogeneous distribution of fumed silica aggregates at low filler contents led to remarkable improvements of the thermal stability and of the ultimate tensile mechanical properties, both under quasi-static and impact conditions. On the basis of these preliminary indications, in the present paper organo-treated fumed silica nanoparticles (Aerosil® R974) were added at a given filler amount (2 vol%) to a HDPE matrix to prepare highly drawn nanocomposite fibers. The influence of fumed silica nanoparticles on the thermo–mechanical behavior of the resulting fibers, with particular attention to their quasi-static tensile and creep behaviour, was investigated.

2. Experimental section
2.1. Materials
High density polyethylene Eltex® A4009 (melt flow rate at 190°C and 2.16 kg = 0.8 dg·min^{-1}, density at 23°C = 0.96 g·cm^{-3}) was supplied in the form of fine powder by BP Solvay (Bruxelles, Belgium). According to the producer's datasheet, the supplied powder has a granulometric distribution comprised between 30 and 1500 μm. Fumed silica nanoparticles Aerosil® R974 were kindly supplied by Evonik (Essen, Germany). Aerosil® R974 is an hydrophobic silica (surface treated with dimethyldichlorosilane) with a specific surface area of 170 m^2·g^{-1} and a bulk density of 1.99 g·cm^{-3} at 23°C. According to the producer's information, this nanofiller is composed by equiaxic nanoparticles with a mean size of 12 nm fused together during the manufacturing operations, forming aggregates of completely amorphous nanoparticles having a mean diameter between 50 and 100 nm. The aggregates are organized in physical

agglomerates that can be partially destroyed during the mixing operations.

Fumed silica nanoparticles were mechanically mixed with HDPE powder at a constant concentration of 2 vol% through a Dispermat F1 mixer, operating at 500 rpm for 5 minutes. The mixture was then melt-compounded in a Thermo-Haake Polylab Rheomix PTW 16p co-rotating intermeshing twin-screw extruder (screw diameter = 16 mm, L/D ratio = 25, rod die diameter = 1.65 mm). A constant screws speed of 3 rpm was set, while the temperature profile, from hopper to rod die, was as follows: 130, 200, 210, 220 and 220°C. The spun fibers were cooled in water at room temperature and collected on a glass drum (40 mm diameter) rotating at 67 rpm. This speed was kept as low as possible, in order to reduce orientation and drawing of the fibers immediately after the extrusion. In this way filaments having a mean diameter of about 500 μm were produced and were subsequently drawn in air at 125°C at various collecting rate. The differently drawn fibers were distinguished in dependence on the draw ratio (*DR*), that is defined as the ratio between the initial (A_i) and the final cross sectional area (A_f) of the fibers, according to Equation (1):

$$DR = \frac{A_i}{A_f} = \left(\frac{D_i}{D_f}\right)^2 \tag{1}$$

where D_i and D_f indicate the equivalent diameter of the fibers before and after the drawing process, respectively. Neat HDPE fibers were drawn in a stable way up to *DR* values of 45 (diameter = 75 μm), while nanofilled fibers showed an improved drawability, and draw ratios up to 54 (diameter = 68 μm) were reached in a stable manner. The diameter of each fiber was measured by using an optical microscope connected to an image processing software (ImageJ®). Moreover, a draw ratio up to 100 was reached on short segments of nanocomposite fibers in an unstable condition.

2.2. Experimental techniques

Differential scanning calorimetry (DSC) tests were performed by a Mettler DSC30 calorimeter (Schwerzenbach, Switzerland). Samples of about 15 mg were sealed in aluminum pan of 160 microliter and were heated from 0°C up to 200°C at 10°C·min^{-1} flushing nitrogen at 100 mL·min^{-1} and then cooled to 0°C at the same rate. A second heating stage up to

200°C was then carried out. Melting temperature (T_m) and crystalline content (X_c) of the fibers were evaluated. As previously shown in the representative DSC thermograms of compounded HDPE plates and reported in a preliminary work on these nanocomposite systems [23], the melting temperature (T_m) was taken as the peak temperature of the endothermic signal in the DSC plots. Crystallinity (X_c) values were computed by integrating the melting endothermic peaks (ΔH) and considering a reference value of 293 J·g^{-1} for the fully crystalline polyethylene (ΔH_0) [26], i.e. (Equation (2)):

$$X_c = \frac{\Delta H}{\Delta H_0 \cdot W_{HDPE}} \cdot 100 \tag{2}$$

where W_{HDPE} is the weight fraction of HDPE in the composites. A single specimen of fiber at selected equivalent draw ratio of both virgin and nanofilled HDPE was tested.

Dynamical mechanical thermal analysis (DMTA) tests were conducted by a Polymer Laboratories MKII machine in tensile configuration. The tested fibers were folded in an aluminum foil in the grip zone, in order to prevent the slippage of the specimens during the application of the dynamic displacement, and a gage length of 15 mm was set for all the specimens. Mono-frequency tests were performed from –135 to 60°C at a heating rate of 3°C·min^{-1} and a frequency of 5 Hz. A peak to peak displacement of 64 μm was imposed to all the tested specimens, and a pre-stress ranging between 1 and 40 MPa was applied proportionally to the *DR*. Moreover, on neat and nanofilled fibers drawn at a ratio of 45 multi-frequency tests were conducted at 0.3, 1, 3, 5, 10 Hz, in a temperature range from –40 to 60°C at a heating rate of 0.5°C·min^{-1}. A pre-stress of 40 MPa and a peak to peak displacement of 32 μm was applied. According to a frequency-temperature superposition principle [34], storage modulus master curves at the reference temperature of 30°C were generated.

Quasi-static tensile mechanical properties of the fibers were performed by an Instron 4502 tensile testing machine, equipped with a 100 N load cell. According to ASTM C1557 standard, single filaments were cut from the bobbin and glued on paper mounting tabs, with a gage length of 30 mm. Before testing, each specimen was preliminary observed with an Ortholux II POL-BK optical microscope at

different magnifications, in order to determine its diameter. At least five specimens were tested for each sample at a cross-head speed of 50 mm·min^{-1}. Creep response of the fibers at room temperature was tested through the same tensile testing machine, equipped with a load cell of 10 N. Both pure and nanofilled fibers were tested at a constant stress equal to 10% of their quasi-static tensile stress at break. The creep compliance $D(t)$ was computed as the ratio between the deformation and the constant applied stress, and it was monitored over a time interval of 3600 s. Fibers drawn at a draw ratio of 45 were also tested under various creep stresses ranging from 5 to 25% of their tensile stress at break.

In order to have some insight on the microstructural behaviour of the prepared materials, ultramicrotomed cross sections of nanocomposite fibers undrawn ($DR = 1$) and at the maximum draw ratio ($DR = 100$) were observed by a Tecnai G2 transmission electron microscope (TEM), supplied by FEI Company (Hillsboro, Oregon, USA), operating at cryogenic temperature (lower than –70°C).

3. Results and discussion
3.1. DSC and DMTA results

In Figure 1a and in Figure 1b DSC thermograms of neat and nanofilled fibers at different DRs are respectively reported, while the most important results obtained from these tests are summarized in Table 1. As it commonly happens in semicrystalline polymers stretched above their glass transition temperature [35, 36], the melting temperature (T_m) increases with the draw ratio. Above a draw ratio of 25, T_m does not increase anymore and tends to level off at a value of about 142°C. At the same time, the crystallinity content increases with the draw ratio up to values in the range of 75–80%. Accordingly to literature [37], it can be hypothesized that the applied drawing induces an ordering of the crystalline phase along the strain direction. Comparing

Table 1. Melting temperature and crystallinity of neat and nanocomposite HDPE fibers from DSC tests (first heating stage)

	T_m [°C]		X_c [%]	
Draw ratio	HDPE	HDPE-2% AR974	HDPE	HDPE-2% AR974
1	134.6	131.0	53.5	50.5
7	136.5	138.6	59.3	67.3
25	141.9	142.5	74.0	77.6
40	141.4	142.3	79.9	78.4
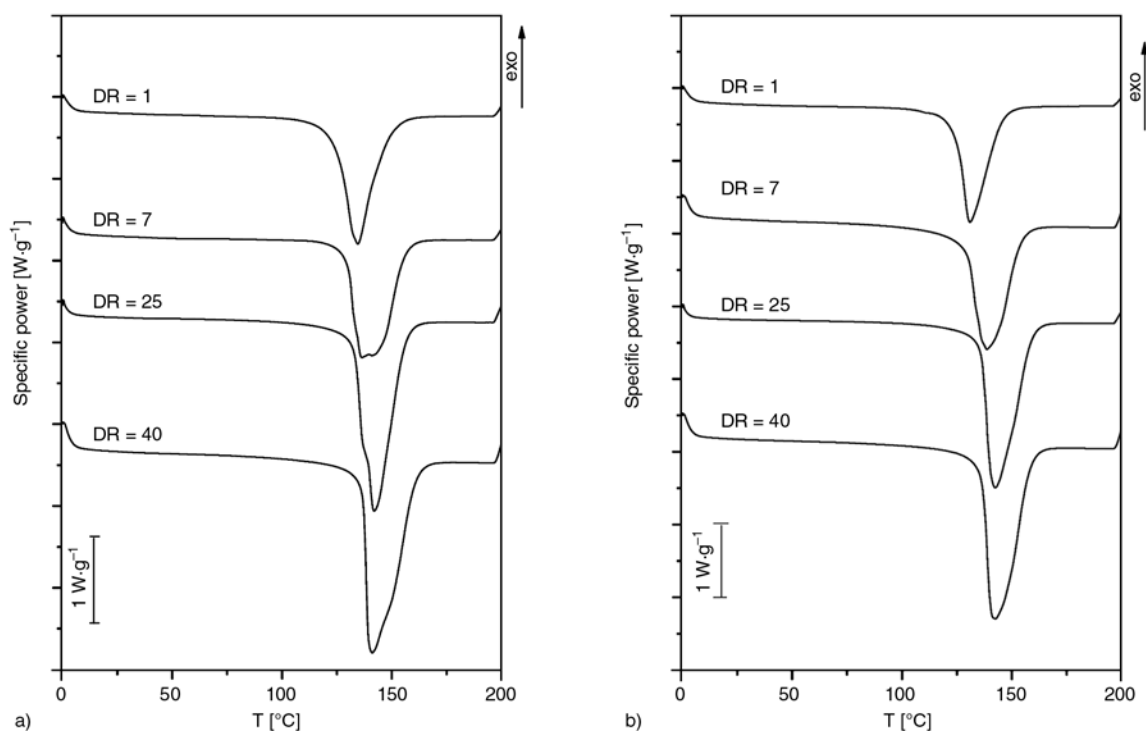
Figure 1. DSC thermograms of (a) neat HDPE and (b) nanocomposite fibers at different DR values (first heating stage)

the crystallinity degree and the melting temperature of pure and nanofilled fibers, it emerges that the introduction of fumed silica nanoparticles plays only a marginal effect on the crystallization behavior of the HDPE. Cooling thermograms evidenced that crystallization temperature of molten fiber range is between 116 and 111°C, directly proportional to the *DR* of the fiber, but in the same it was found independent on the composition. Also the DSC thermograms collected during the second heating stage (here omitted for the sake of brevity) evidenced an independency of both T_m and X_c from the presence of nanosilica. Comparing these results with the literature references, it is difficult to have a clear picture of the effects of nanofillers on the crystallization behaviour of polyethylene fibers. In fact, Zhang *et al.* [33] found an increase of the fiber crystallinity promoted by the addition of surface treated nanosilica in UHMWPE. Also Ruan *et al.* [32] reported that the addition of MWCNT at a concentration of 5 wt% had a nucleating effects on polyethylene crystals, particularly in the highly aligned fibers, but the crystallinity of the composite fibers was slightly lower than that of the pristine fibers. On the other hand, La Mantia *et al.* [30] found that organomodified layered silicates did not have any effect on the crystallization properties of LLDPE fibers and hypothesized that the orientation in both crystalline and amorphous phases were similar for filled and unfilled fibers. According to our previous works on polyethylene based nanocomposites [20, 21, 23], we can hypothesize that the limited influence played by fumed silica nanoparticles on the crystallization properties of our HDPE matrix could be probably ascribed to their dispersion state. However, further investigations are needed to reach a deeper comprehension on the role played by nanosilica on the crystallization behaviour of polyethylene.

It is important to note that the maximum draw ratio reached on nanofilled fibers during the hot stretching and continuous collecting process (*DR* = 54) is significantly higher than that achievable with neat fibers (*DR* = 45). This means that the presence of fumed silica nanoparticles improves fibers drawability. Storage modulus (*E′*) curves of neat polyethylene and nanocomposite fibers obtained in DMTA tests at a frequency of 5 Hz are reported in Figure 2. As expected, the molecular orientation induced by
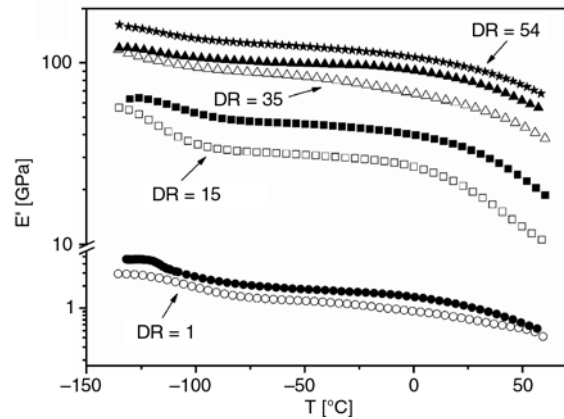
Figure 2. Storage modulus (*E′*) of neat HDPE fibers (open symbols) and nanocomposite fibers (filled symbols) at various draw ratios as determined in DMTA tests at a frequency of 5 Hz

stretching results in a noticeable increase of *E′* values over the whole range of investigated temperatures. The presence of nanosilica produces a remarkable stiffening effect on the resulting fibers. In fact, for any given draw ratio, nanocomposite fibers exhibit higher storage modulus values with respect to the neat ones. It is widely reported in literature how the increase of the elastic properties of the drawn fibers can be due both to the crystallinity increase induced by the molecular orientation and to possible changes in the crystal size/morphology promoted by the cold drawing process [38]. Also nanoparticles can alter crystallization behaviour of the nanofilled fibers [30, 32, 33]. In our case, DSC tests on the nanofilled fibers excluded any effect on the overall crystallinity degree due to the nanofiller introduction, but it is possible to hypothesize that crystal size could be altered by the presence of silica aggregates within the matrix. However, it is only an hypothesis, and only a detailed study on the crystallization properties of nanofilled fibers could provide a satisfactory answer to this point. In the future, further efforts will be made to better understand the crystallization behaviour of the investigated systems. In order to evaluate the dynamic behaviour over an extended frequency range, multi-frequency DMTA tests were also performed on high drawn neat and nanofilled fibers (*DR* = 45). Figure 3 reports the resulting master curves obtained on the basis of a frequency-temperature superposition principle at a reference temperature of 30°C. Over the entire frequency range, storage modulus values of nanofilled fibers are higher than those of unfilled fibers. From
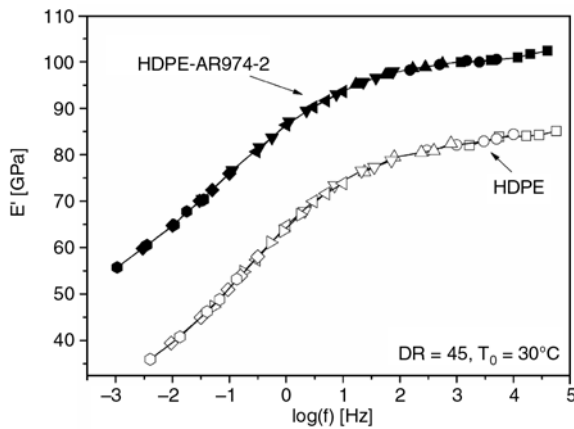
Figure 3. Storage modulus (E') master curves of neat HDPE fibers (open symbols) and nanocomposite (filled symbols) fibers at $DR = 45$ from DMTA multi-frequency tests ($T_0 = 30°C$)

the correspondent plot of the shift factors as a function of temperature (not reported for the sake of brevity) an Arrhenius type trend can be observed [34], characterized by an activation energy of the viscoelastic process of $147+2$ kJ·mol^{-1} for the neat specimens and $167+6$ kJ·mol^{-1} for nanofilled HDPE fibers.

3.2. Quasi-static and creep tensile properties

Elastic modulus (E) values of the tested fibers as a function of the draw ratio are summarized in Figure 4a, while stress (σ_B) and strain (ε_B) at break values are reported in Figure 4b and Figure 4c, respectively. According to DMTA results, it is evident that the presence of fumed silica nanoparticles produces a significant increase of the elastic modulus, especially at elevated draw ratios. Furthermore, the possibility of reaching higher draw ratios with the nanosilica introduction allows us to prepare fibers possessing higher elastic moduli (about 55 GPa for a DR of 54). Interestingly, the increase of the fibers stiffness can be obtained without impairing their tensile properties at break. In fact, both stress and strain at break values do not appear to be influenced by the presence of nanofiller. The better drawability of nanofilled fibers offers the possibility to reach higher stress at break values (about 1.65 GPa for a DR of 54).

Figure 5a displays creep compliance curves for neat and nanocomposite polyethylene fibers drawn at various DRs and loaded at a stress level equal to 10% of their stress at break values. Even if at $DR = 1$ the creep compliance of the nanocomposite fibers is
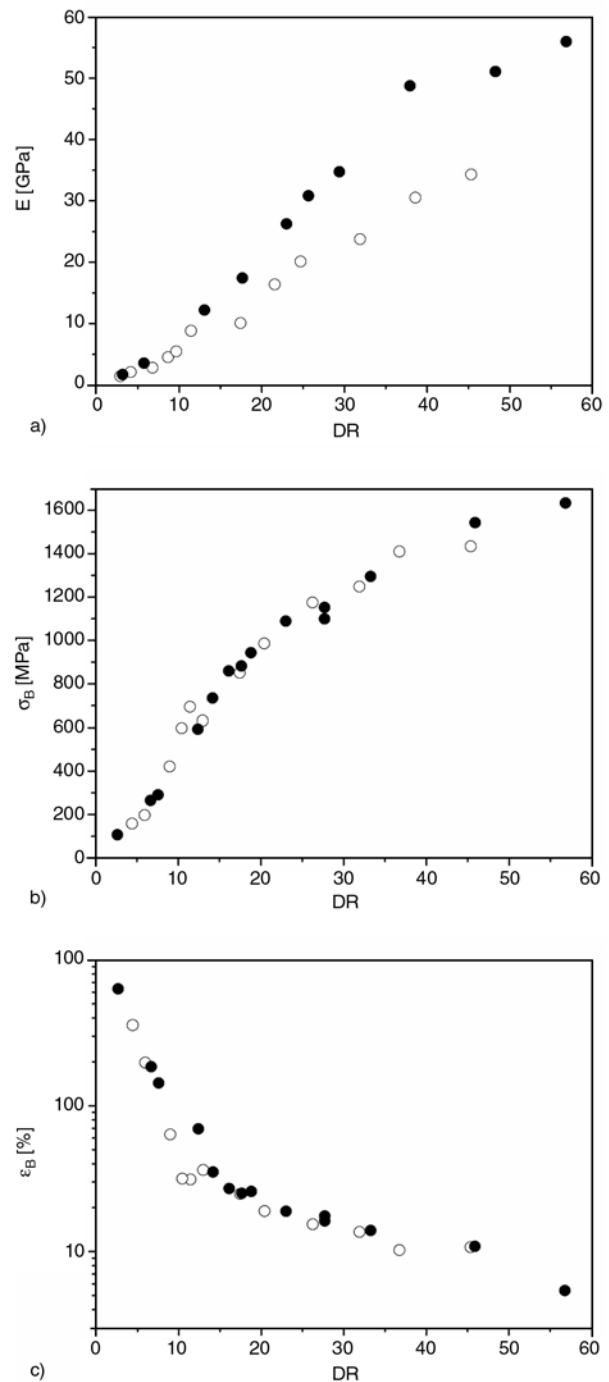

Figure 4. Mechanical properties of neat HDPE fibers (open symbols) and nanocomposite fibers (filled symbols) from quasi-static tensile tests: (a) Elastic modulus, (b) Stress at break, (c) Strain at break

practically equal to that of the unfilled ones, an interesting improvement of the creep stability due to the nanofiller introduction can be detected as the draw ratio increases. This trend can be clearly evidenced in the plot of creep compliance values at 3600 s as a function of the draw ratio (Figure 5b).
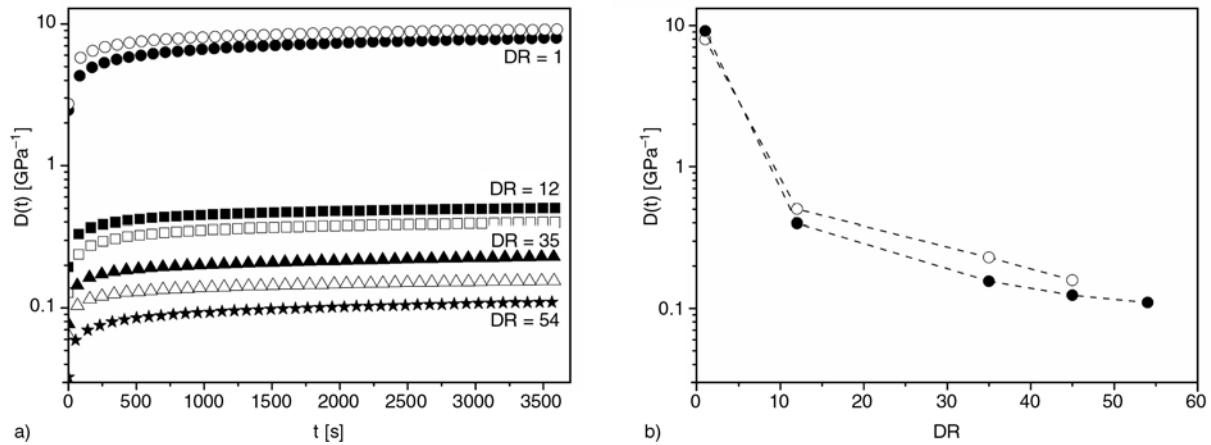
Figure 5. Creep tests on neat HDPE fibers (open symbols) and nanocomposite fibers (filled symbols) at $\sigma_0 = 10\%$ of σ_B: (a) creep compliance curves at various draw ratios, (b) creep compliance values at 3600 s as a function of the draw ratio
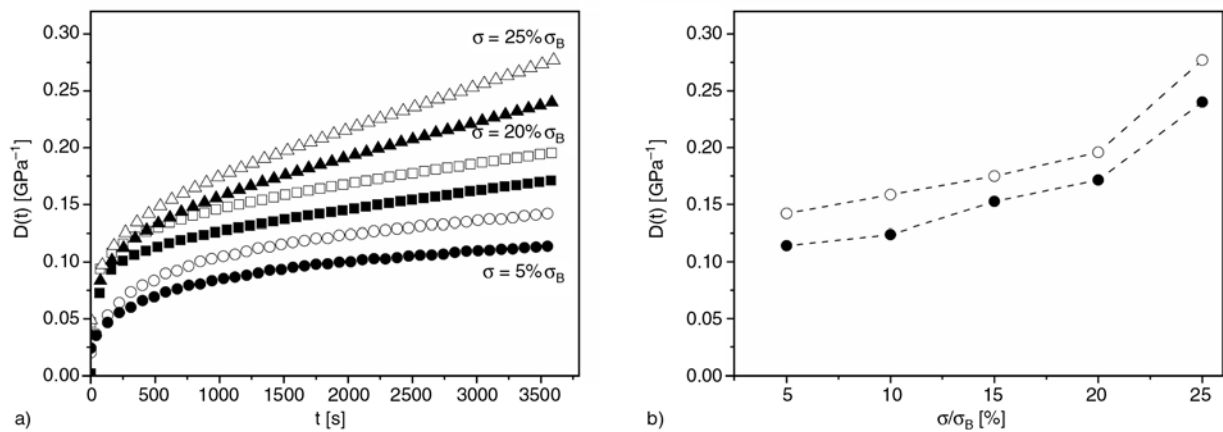
Figure 6. Creep tests on neat HDPE fibers (open symbols) and nanocomposite fibers (filled symbols) at *DR* = 45: (a) creep compliance curves at various stress levels, (b) creep compliance after 3600 s as a function of the normalized stress

In order to evaluate the effect of the applied stress on the creep behaviour of the tested fibers, creep compliance curves of neat and nanocomposite fibers processed at *DR* = 45 are reported in Figure 6a for various stress levels. Once again, the presence of the nanofiller produces an interesting decrease of the creep compliance values with respect to the neat HDPE fibers for all the investigated stress levels. Furthermore, if creep compliance values at 3600 s are compared for various stress levels (Figure 6b) it emerges that, in absolute value, the stabilizing effect provided by nanosilica introduction is not substantially influenced by the stress level.

3.3. Microstructure

Concerning the polymer microstructure in the fibers, considering that DSC evidenced how both melting temperature and crystallinity degree are about the same for both materials (see Table 1), it is reason-

able to hypothesize that the orientation of HDPE macromolecules both in crystalline and in amorphous phases is similar for neat and nanocomposite fibers. These results are in good agreement with the conclusions reported by La Mantia *et al.* [30]. Therefore, the experienced increase of the mechanical properties due to nanosilica introduction cannot be attributed to different chain orientation in the tested materials. In our previous work on the fracture behavior of LLDPE/fumed silica nanocomposites [39], the enhancement of mechanical properties observed for nanocomposites was explained as an effect of the progressive alignment of nanofiller aggregates along the strain direction. In order to support this hypothesis, TEM images of the ultramicrotomed cross sections of nanofilled fibers at *DR* = 1 (undrawn fibers) and at *DR* = 100 are respectively reported in Figure 7a and in Figure 7b. Undrawn fibers are characterized by the presence of fumed
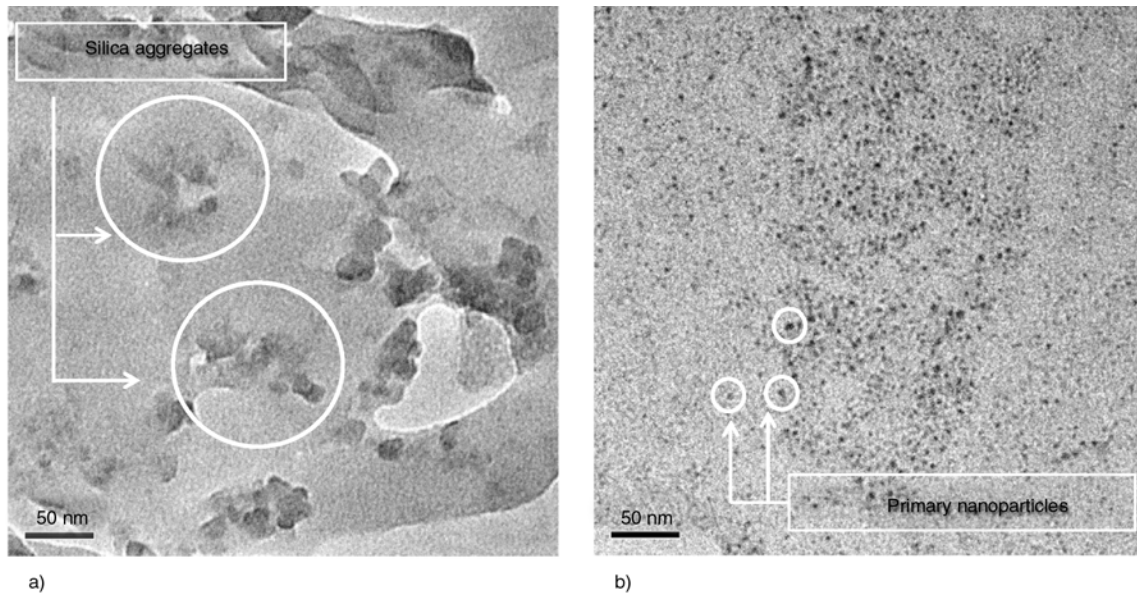
Figure 7. TEM images of ultra-microtomed cross-sections of (a) undrawn (*DR* = 1) and (b) highly drawn (*DR* = 100) nanocomposite fibers

silica nanoparticles uniformly dispersed in the matrix forming isodimensional clusters of aggregated primary nanoparticles having a mean size lower than 100 nm. It is difficult to assess whether the clusters are constituted by aggregation of primary nanoparticles fused together during the manufacturing process or if they are formed by physical agglomeration of aggregates. However, it is evident that agglomerates are relatively small and apparently well dispersed within the matrix. This could justify the retention of the tensile properties at break experienced in quasi-static tests. A similar microstructure was observed for HDPE/fumed silica composites obtained by melt compounding and compression molding [23]. This means that melt spinning process has a negligible effects on the microstructural behaviour of the prepared materials, because chain alignment along the flow direction is not followed by a deformation and/or rupture of silica aggregates. This could explain why at *DR* = 1 the tensile properties of nanofilled fibers are very near to those of the unfilled ones. The microstructure is very different when an elevated draw ratio is applied to the fibers (Figure 7b). In this case the drawing process produces the rupture of silica aggregates and, most probably, their alignment along the cold drawing direction. In the cryofractured sections it is possible to detect the presence of individual primary nanoparticles having a mean size of about 10 nm, in good agreement with the indication reported in the

datasheet by the producer. Unfortunately, due to the experimental difficulties in preparing thin sections of the fiber along their axis, no direct evidence of the alignment phenomenon can be experimentally provided. Nevertheless, we recently reported a direct experimental evidence of alignment of streams of nanoparticle along the drawing direction in a similar system consisting of an LLDPE matrix filled with fumed silica nanoparticles [39]. This means that the agglomerates of fumed metal oxides nanoparticles, once exposed to an elongational flow in the solid state, orient themselves along the strain direction. Unlike conventional microfillers, fumed silica aggregates can be deformed and fractured to form long streams of nanoparticles dispersed within the polymer matrix. This process is very similar to the exfoliation process induced by the flow in polymer/clay nanocomposites with a good affinity between the two components [40]. Therefore, the larger enhancement of the elastic modulus observed for the nanofilled samples at elevated filler contents cannot be attributed solely to the orientation of the polyethylene macromolecules. The elongational flow, unlike the shear flow, is able to break and orient the dispersed nanoparticle aggregates even if the viscosity ratio of the two phases is very different, and the dramatic increase of the filler-matrix interfacial area could be thus responsible of the observed increase of the mechanical properties. As explained in Paragraph 3.1, nanofiller introduction

could alter the crystal size/morphology of the oriented matrix, with important consequences on the mechanical behaviour of the resulting material. Therefore, the stiffening effect due to silica nanoparticles experienced in this work can be probably ascribed both to an increase of the filler-matrix interfacial area due to the aggregates elongation, and to possible changes in the crystalline morphology of the matrix. However, these two effects play a synergistic role in polymer processing expecially for fiber production, where the phenomenon of crystallization-induced-orientation affects mechanical properties, and the amorphous phase orientation is also involved.

4. Conclusions

Surface treated fumed silica nanoparticles were melt compounded with a high density polyethylene matrix in order to produce nanocomposite fibers in a double step process of extrusion and drawing. Fibers stiffness was remarkably improved by nanofiller introduction, especially at elevated draw ratios, without affecting tensile properties at break of the pristine fibers. DSC tests evidenced how both the melting temperature and the crystallinity degree of the fibers are not substantially affected by the nanosilica introduction. Also creep tests evidenced a certain reduction of the creep compliance with respect to the neat HDPE fibers over the whole range of investigated draw ratios and applied stresses. TEM images revealed how the experienced improvements of the mechanical properties could be probably related to the strong alignment of silica aggregates along the strain direction and to the consequent increase of the filler-matrix interfacial area. Moreover, the stiffening effect of the nanofiller in drawn fiber is also confirmed from dynamical mechanical analysis, as evidenced from the higher storage modulus in the range of temperature (–40°C/+60°C) and the higher master curve of storage modulus at 30°C in the range of frequency (10^{-3}–10^5 Hz).

Acknowledgements

References

[1] Hussain F., Hojjati M., Okamoto M., Gorga R. E.: Review article: Polymer-matrix nanocomposites, processing, manufacturing, and application: An overview. Journal of Composite Materials, **40**, 1511–1575 (2006).
DOI: 10.1177/0021998306067321

[2] Chrissafis K., Paraskevopoulos K. M., Tsiaoussis I., Bikiaris D.: Comparative study of the effect of different nanoparticles on the mechanical properties, permeability, and thermal degradation mechanism of HDPE. Journal of Applied Polymer Science, **114**, 1606–1618 (2009).
DOI: 10.1002/app.30750

[3] Li S., Chen H., Cui D., Li J., Zhang Z., Wang Y., Tang T.: Structure and properties of multi-walled carbon nanotubes/polyethylene nanocomposites synthesized by *in situ* polymerization with supported Cp_2ZrCl_2 catalyst. Polymer Composites, **31**, 507–515 (2010).
DOI: 10.1002/pc.20831

[4] Yang B-X., Pramoda K. P., Xu G. Q., Goh S. H.: Mechanical reinforcement of polyethylene using polyethylene-grafted multiwalled carbon nanotubes. Advanced Functional Materials, **17**, 2062–2069 (2007).
DOI: 10.1002/adfm.200600599

[5] Dorigato A., Morandi S., Pegoretti A.: Effect of nanoclay addition on the fiber/matrix adhesion in epoxy/glass composites. Journal of Composite Materials, **46**, 1439–1451 (2012).
DOI: 10.1177/0021998311420311

[6] Dorigato A., Pegoretti A.: Development and thermomechanical behavior of nanocomposite epoxy adhesives. Polymers for Advanced Technologies, **23**, 660–668 (2012).
DOI: 10.1002/pat.1942

[7] Dorigato A., Pegoretti A., Penati A.: Effect of the polymer–filler interaction on the thermo-mechanical response of polyurethane-clay nanocomposites from blocked prepolymer. Journal of Reinforced Plastics and Composites, **30**, 325–335 (2011).
DOI: 10.1177/0731684410396599

[8] Lee E. M., Oh Y. S., Ha H. S., Jeong H. M., Kim B. K.: Ultra high molecular weight polyethylene/organoclay hybrid nanocomposites. Journal of Applied Polymer Science, **114**, 1529–1534 (2009).
DOI: 10.1002/app.30736

[9] Mandalia T., Bergaya F.: Organo clay mineral–melted polyolefin nanocomposites effect of surfactant/CEC ratio. Journal of Physics and Chemistry of Solids, **67**, 836–845 (2006).
DOI: 10.1016/j.jpcs.2005.12.007

[10] Pegoretti A., Dorigato A., Brugnara M., Penati A.: Contact angle measurements as a tool to investigate the filler–matrix interactions in polyurethane–clay nanocomposites from blocked prepolymer. European Polymer Journal, **44**, 1662–71672 (2008).
DOI: 10.1016/j.eurpolymj.2008.04.011

[11] Bondioli F., Dorigato A., Fabbri P., Messori M., Pegoretti A.: High-density polyethylene reinforced with submicron titania particles. Polymer Engineering and Science, **48**, 448–457 (2008).
DOI: 10.1002/pen.20973

[12] Bondioli F., Dorigato A., Fabbri P., Messori M., Pegoretti A.: Improving the creep stability of high-density polyethylene with acicular titania nanoparticles. Journal of Applied Polymer Science, **112**, 1045–1055 (2009).
DOI: 10.1002/app.29472

[13] Kontou E., Niaounakis M.: Thermo-mechanical properties of LLDPE/SiO_2 nanocomposites. Polymer, **47**, 1267–1280 (2006).
DOI: 10.1016/j.polymer.2005.12.039

[14] Yang F., Nelson G. L.: PMMA/silica nanocomposite studies: Synthesis and properties. Journal of Applied Polymer Science, **91**, 3844–3850 (2004).
DOI: 10.1002/app.13573

[15] Zhang M. Q., Rong M. Z., Zhang H. B., Friedrich K.: Mechanical properties of low nano-silica filled high density polyethylene composites. Polymer Engineering and Science, **43**, 490–500 (2003).
DOI: 10.1002/pen.10040

[16] Chaichana E., Jongsomjit B., Praserthdam P.: Effect of nano-SiO_2 particle size on the formation of LLDPE/SiO_2 nanocomposite synthesized via the *in situ* polymerization with metallocene catalyst. Chemical Engineering Science, **62**, 899–905 (2007).
DOI: 10.1016/j.ces.2006.10.005

[17] Jongsomjit B., Panpranot J., Praserthdam P.: Effect of nanoscale SiO_2 and ZrO_2 as the fillers on the microstructure of LLDPE nanocomposites synthesized via *in situ* polymerization with zirconocene. Materials Letters, **61**, 1376–1379 (2007).
DOI: 10.1016/j.matlet.2006.07.034

[18] Wang Z., Li G., Xie G., Zhang Z.: Dispersion behavior of TiO_2 nanoparticles in LLDPE/LDPE/TiO_2 nanocomposites. Macromolecular Chemistry and Physics, **206**, 258–262 (2005).
DOI: 10.1002/macp.200400309

[19] Dorigato A., Pegoretti A.: Tensile creep behaviour of polymethylpentene–silica nanocomposites. Polymer International, **59**, 719–724 (2010).
DOI: 10.1002/pi.2769

[20] Dorigato A., Pegoretti A., Kolařík J.: Nonlinear tensile creep of linear low density polyethylene/fumed silica nanocomposites: Time-strain superposition and creep prediction. Polymer Composites, **31**, 1947–1955 (2010).
DOI: 10.1002/pc.20993

[21] Dorigato A., Pegoretti A., Penati A.: Linear low-density polyethylene/silica micro- and nanocomposites: Dynamic rheological measurements and modelling. Express Polymer Letters, **4**, 115–129 (2010).
DOI: 10.3144/expresspolymlett.2010.16

[22] Dorigato A., Pegoretti A., Fambri L., Slouf M., Kolarik J.: Cycloolefin copolymer/fumed silica nanocomposites. Journal of Applied Polymer Science, **119**, 3393–3402 (2011).
DOI: 10.1002/app.32988

[23] Dorigato A., D'Amato M., Pegoretti A.: Thermo-mechanical properties of high density polyethylene – fumed silica nanocomposites: Effect of filler surface area and treatment. Journal of Polymer Research, **19**, 9889–9899 (2012).
DOI: 10.1007/s10965-012-9889-2

[24] Pennings A. J., Smook J., De Boer J., Gogolewski S., van Hutten P. F.: Process of preparation and properties of ultra-high strength polyethylene fibers. Pure and Applied Chemistry, **55**, 777–798 (1983).

[25] Smith P., Lemstra P. J., Kalb B., Pennings A. J.: Ultra-high-strength polyethylene filaments by solution spinning and hot drawing. Polymer Bulletin, **1**, 733–736 (1979).
DOI: 10.1007/BF00256272

[26] Van Krevelen D. W.: Properties of polymers. Elsevier. Amsterdam (1990).

[27] Smith P., Lemstra P. J., Pijpers J. P. L.: Tensile strength of highly oriented polyethylene. II. Effect of molecular weight distribution. Journal of Polymer Science Part B: Polymer Physics, **20**, 2229–2241 (1982).
DOI: 10.1002/pol.1982.180201206

[28] Salem D. R.: Structure formation in polymeric fibers. Hanser, Munich (2005).

[29] Chantrasakul S., Amornsakchai T.: High strength polyethylene fibers from high density polyethylene/organoclay composites. Polymer Engineering and Science, **47**, 943–950 (2007).
DOI: 10.1002/pen.20778

[30] La Mantia F. P., Dintcheva N. T., Scaffaro R., Marino R.: Morphology and properties of polyethylene/clay nanocomposite drawn fibers. Macromolecular Materials and Engineering, **293**, 83–91 (2008).
DOI: 10.1002/mame.200700204

[31] Mezghani K., Farooqui M., Furquan S., Atieh M.: Influence of carbon nanotube (CNT) on the mechanical properties of LLDPE/CNT nanocomposite fibers. Materials Letters, **65**, 3633–3635 (2011).
DOI: 10.1016/j.matlet.2011.08.002

[32] Ruan S., Gao P., Yu T. X.: Ultra-strong gel-spun UHMWPE fibers reinforced using multiwalled carbon nanotubes. Polymer, **47**, 1604–1611 (2006).
DOI: 10.1016/j.polymer.2006.01.020

[33] Zhang Y., Yu J., Zhou C., Chen L., Hu Z.: Preparation, morphology, and adhesive and mechanical properties of ultrahigh-molecular-weight polyethylene/SiO_2 nanocomposite fibers. Polymer Composites, **31**, 684–690 (2010).
DOI: 10.1002/pc.20847

[34] Riande E., Calleja R. D., Prolongo M., Masegosa R.: Polymer viscoelasticity, stress and strain in practice. Marcel Dekker, New York (2000).

[35] Anandakumaran K., Roy S. K., St. John Manley R.: Drawing-induced changes in the properties of polyethylene fibers prepared by gelation/crystallization. Macromolecules, **21**, 1746–1751 (1988). DOI: 10.1021/ma00184a036

[36] Selikhova V. I., Ozerina L. A., Ozerin A. N., Bakeyev N. F.: Special melting behaviour of highly oriented polyethylene. Polymer Science U.S.S.R., **28**, 378–385 (1986). DOI: 10.1016/0032-3950(86)90094-8

[37] Capaccio G., Crompton T. A., Ward I. M.: Ultra-high modulus polyethylene by high temperature drawing. Polymer, **17**, 644–645 (1976). DOI: 10.1016/0032-3861(76)90288-3

[38] Humphreys J., Ward I. M., Nix E. L., McGrath J. C., Emi T.: A study of the drawing behavior of polyvinylidene fluoride. Journal of Applied Polymer Science, **30**, 4069–4079 (1985). DOI: 10.1002/app.1985.070301010

[39] Dorigato A., Pegoretti A.: Fracture behaviour of linear low density polyethylene – fumed silica nanocomposites. Engineering Fracture Mechanics, **79**, 213–224 (2012). DOI: 10.1016/j.engfracmech.2011.10.014

[40] Tokihisa M., Yakemoto K., Sakai T., Utracki L. A., Sepehr M., Li J., Simard Y.: Extensional flow mixer for polymer nanocomposites. Polymer Engineering and Science, **46**, 1040–1050 (2006). DOI: 10.1002/pen.20542

Facile synthesis of polypyrrole nanofiber and its enhanced electrochemical performances in different electrolytes

S. Sahoo, S. Dhibar, C. K. Das[*]

Materials Science Centre, Indian Institute of Technology, 721302 Kharagpur, India

Abstract. A porous nanocomposite based on polypyrrole (PPy) and sodium alginate (SA) has been synthesized by easy, inexpensive, eco-friendly method. As prepared nanocomposite showed fibrillar morphology in transmission electron microscopic (TEM) analysis. The average diameter of ~100 nm for the nanofibers was observed from scanning electron microscopic (SEM) analysis. As prepared nanofiber, was investigated as an electrode material for supercapacitor application in different aqueous electrolyte solutions. PPy nanofiber showed enhanced electrochemical performances in 1 M KCl solution as compared to 1 M Na_2SO_4 solution. Maximum specific capacitance of 284 F/g was found for this composite in 1 M KCl electrolyte. It showed 76% specific capacitance retention after 600 cycles in 1 M KCl solution. Electrochemical Impedance Spectra showed moderate capacitive behavior of the composite in both the electrolytes. Further PPy nanofiber demonstrated higher thermal stability as compared to pure PPy.

Keywords: *nanocomposites, polypyrrole, sodium alginate, nanofiber, supercapacitor*

1. Introduction

Among different nonstructural morphologies of conducting polymers (CP), one dimensional nanostructures have produced a great deal of research interest as these has offered various potential applications in different fields such as chemical sensor, gas-separation membranes, neuron devices etc. [1–3]. Among various CPs, PPys are well studied because of their good thermal stability, enhanced electrical as well as electrochemical properties, excellent environmental stability [4, 5]. Various approaches for the synthesis of PPy nanofiber have been reported. Several reports are available where PPy nanofibers were prepared by using templates like zeolites, alumina, various nanostructured templates [6, 7]. Some template free approaches for PPy nanofiber synthesis are also reported. Athawale *et al*. [8] has reported the synthesis of PPy nanofiber using ultrasonic wave at room temperature. It was also observed that

with increasing sonication time, the length of the fiber increases. PPy nano-network as well as nanofiber were also prepared by using interfacial and template polymerization technique and investigated as a promising material for device applications [9]. Zang *et al*. [10] has reported a template-free electrochemical one-step synthetic approach to prepare PPy nanofiber in aqueous solution using phosphate buffer solution, with unique chem-physical properties.

Among various energy storage devices of today's world, supercapacitors has been considered as the most widely investigated energy storage devices due to their low maintenance cost, fast charging ability as well as exceptionally high cyclic stability [11, 12]. Supercapacitors are mainly used in various high power equipments like hybrid electric vehicles, cellular phones, laptops etc., basically where fast charging is desirable. It has the ability to fulfill

---

the gap between batteries and capacitors. However, supercapacitors are now mainly available in two types:

(1) Electrochemical Double – Layer Capacitor (EDLC) – EDLCs store charges non-faradically. Mainly carbon based materials like activated carbon, carbon nanotube, graphene are used [13–15] as electrode for these type of supercapacitors. Due to high surface area, superior conductivity, high porosity graphene has been considered as an essential candidate for supercapacitor electrode materials. On the other hand, addition of carbon nanotubes can significantly enhance the performances of the EDLC due to its unique properties like nanoporosity, high surface area, and high conductivity [13–15]. In earlier research, activated carbon was also chosen as a part of electrode material because of its high surface area.

(2) Pseudocapacitor – Pseudocapacitors has the capability to store charge faradically through various charge transfer reactions between electrode and electrolyte. Mainly metal oxides and CPs are used [16–18].

CPs are used as pseudocapacitive electrode materials mainly due to their high specific capacitance, high conductivity in charged state, low Equivalent Series Resistance (ESR). The charge – discharge process in these types of pseudocapacitive materials are basically associated with the insertion – deinsertion of counter ions, arises from the electrolyte [19]. Nanostructured materials are mainly used for energy devices because of their low scale dimension which increases the electrolyte transport rate and therefore enhances the electrochemical performances. The specific surface area and high porosity, which are the two significant properties of the nanostructured materials help to achieve superior electrochemical properties. Materials in nanometer size have the ability to improve electrochemical performances because of their unique conducting pathway, nanoscale dimension, high porosity etc. Gupta and Miura [20] prepared electrode material based on electrochemically deposited polyaniline nanowires on stainless steel and achieved a highest specific capacitance of 775 F/g at 10 mV/s scan rate. Li *et al.* [21] reported porous, mat-like polyaniline nanocomposite, which exhibited excellent specific capacitance of 2093 F/g with long cycle life and fast

charging/discharging. Kuila *et al.* [22] reported a simple approach to synthesize ordered arrays of polyaniline nanorods, which exhibited extraordinary electrochemical properties with an electrochemical capacitance value of 3407 F/g. They have suggested that the small dimension of the electrode material increases the utilization of conducting polymer as electrode material. Overall, nanostructured version of conducting polymer has been considered as an essential component for the preparation of electrode materials for supercapacitor applications.

In this work, we have synthesized PPy nanofiber through a facile chemical route using sodium alginate (SA) as template. Further, it's potential to be used as an electrode material for supercapacitor application has been investigated in two different aqueous electrolytes (1 M KCl and 1 M Na_2SO_4 solution).

2. Materials and experiment
2.1. Materials

Pyrrole (E. Merck Ltd, India) was used as a monomer for nanofiber preparation. Potassium chloride (KCl, E. Merck Ltd., India) and sodium sulfate (Na_2SO_4, E. Merck Ltd., India) were used as electrolytes for the electrochemical characterizations. Sodium alginate (SA, Food Grade, Loba Chemie Pvt. Ltd., Mumbai, India), sodium hydroxide (NaOH, Loba Chemie Pvt. Ltd. Mumbai, India) and ammonium persulfate (APS) [$(NH_4)_2SO_4$, Loba Chemie Pvt. Ltd., Mumbai, India] were also used for the preparation of PPy nanofiber. All the chemicals were used as received, without any further purification.

2.2. Characterization techniques
2.2.1. Fourier Transform Infrared Spectroscopy (FTIR)

FTIR spectra of nanocomposites were recorded by IR spectrometer (NEXUS 870, Thermo Nicolet, USA). For the IR spectrum, little bit of sample was mixed with potassium bromide (KBr) in adequate level to make a disk and the disk was analyzed in order to get the spectrum.

2.2.2. Scanning Electron Microscopy (SEM)

The morphology of PPy nanofiber was analyzed through SEM instrument (Tescan VEGA LSU SEM, USA). Small amount of sample was adhered to the

sample holder by carbon tape and analyzed by SEM. However, before analysis the samples were sputtered with gold in order to make them conducting.

2.2.3. High Resolution Transmission Electron Microscopy (HR-TEM)

The bulk morphology of nanofiber was examined by high resolution transmission electron microscopy (HR-TEM, JEOL 2100, Japan). A small amount of the sample was dispersed in acetone through sonication and a drop of this dispersed solution was put on the copper grid for HRTEM analysis.

2.2.4. Electrochemical characterization

Electrochemical experiments such as Cyclic Voltammetry (CV), Electrochemical Impedance Spectroscopy (EIS) were carried out by three electrode system where platinum and saturated calomel electrode (SCE) were used as counter and reference electrodes respectively. Cyclic voltammetry (Gamry Instrument) measurements were performed in two different aqueous electrolytes – 1 M KCl and 1 M Na_2SO_4 solution at different scan rates from 10 to 200 mV/s within a potential window of –0.8 to 0.8 V. The electrodes were used for electrochemical characterization without any polymer binder. The impedance spectroscopy investigations of the nanofiber were performed in the frequency range of 100 mHz to 10 MHz.

2.2.5. Thermogravimmetric analysis

Thermogravimetric analysis was carried out by Dupont 2100 Thermogravimetric analyzer (USA). The TGA measurements were conducted at a heating rate of 10°C/min under N_2 atmosphere from room temperature to 800°C.

2.3. Synthesis of PPy nanofiber

A simple facile method was carried out for the synthesis of PPy nanofiber. In this process, 300 mg of SA was stirred with 0.1 M NaOH (300 ml) at 60°C for 12 h. After that 1 mL of pyrrole was added to the above solution and further stirred for 1 h. The resulting solution was cooled at 0°C. 1 M H_2SO_4 was added drop wise to adjust the pH value of the solution to 7. 1 g of APS was poured into the solution and kept at 0°C for 24 h for the synthesis of nanofiber. The black colored precipitation was collected by filtration and washed with deionized water for several times. Lastly the PPy nanofiber composite was dried at 60°C. For comparison, PPy without SA was prepared by an in-situ oxidative polymerization method [23].

3. Results and discussion

3.1. PPy nanofiber synthesis

SA is the sodium salt of alginic acid. It is a linear copolymer with homopolymeric blocks of (1-4)-linked β-D-mannuronate (M) and its C-5 epimer α-L-guluronate (G) residues (Figure 1) and can act as polyelectrolyte. This is a biomacromolecular polysaccharide, mainly used for different biomedical applications. The strong electrostatic repulsions among the carboxylate anions of SA (–COO⁻) allows it to form expanded network structure, which is the prime requirement for easy electrolyte accessibility and by this way it has become an important tool for the construction of electrode material for supercapacitor application [24]. However, in the typical synthetic procedure, addition of monomer allows the biomolecule to form biopolymer – monomer complexes through hydrogen bonding. The probable structure of the bio polymer-monomer complex has been proposed and shown in Figure 2. How-
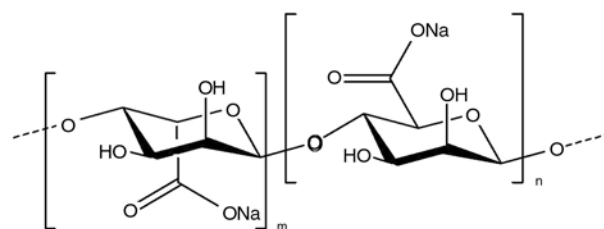

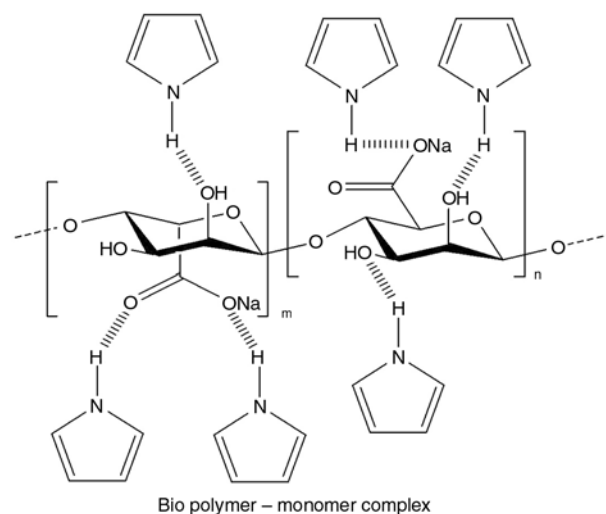**Figure 1.** Chemical structure of sodium alginate

Figure 2. Probable structure of bio polymer-monomer complex

ever, when the oxidant APS was added in the reaction mixture, polymerization occurred as well as PPy were initiated onto the biopolymer chains and also formed PPy Nanofiber composite [3]. The SEM image of PPy Nanofiber shows this fiber like network morphology. According to Zhang *et al.* [24] nanofibrillar morphology can be achieved only when the seed template also shows nanofibrillar morphology and has the capability to react with the monomer. Here, SA itself has the ability to exhibit nanofibrillar morphology and also can react with pyrrole. So, the choice of SA for nanofiber synthesis is reasonable and perfect.

3.2. FTIR analysis

FTIR analysis is generally carried out to identify the chemical environment of the composites. The FTIR spectrum of SA, pure PPy and PPy nanofiber are shown in Figure 3. The peaks at 1623, 1415, 1088 and 1034 cm^{-1} in the FTIR spectrum of SA correspond to the asymmetric COO$^-$, symmetric COO$^-$, C–O and C–O–C stretching respectively. The peaks at 1562, 1469 and 3410 cm^{-1} correspond to the C–C, C–N and N–H stretching vibrations of the pyrrole ring [23]. Whereas, the peaks at 2855 and 2962 cm^{-1} are associated with the symmetric and asymmetric vibrations of CH$_2$ of PPy [25]. However, it is noticed that the different peaks of SA are shifted to lower frequency region in the FTIR spectrum of PPy nanofiber. Such appearance of the bands at shifted positions in case of composite may be due to the result of the interaction between PPy and SA. Caykara *et al.* [26] successfully prepared the blend of poly (ethylene oxide) and SA by solution casting method and
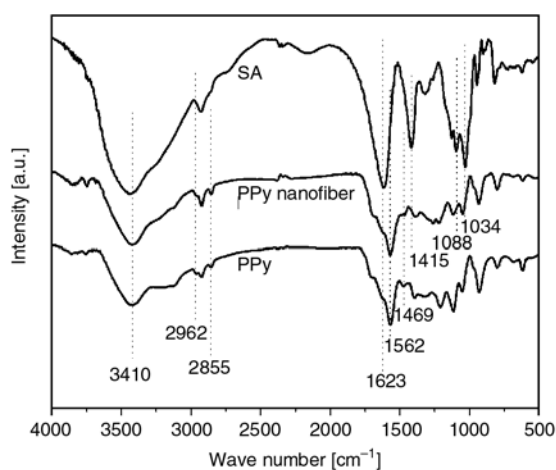
established that the hydrogen bonding interaction between two polymers is responsible for the band shifting. Thus, FTIR spectrum of the composite confirms the formation of hydrogen bonding between PPy and SA. Similar type of spectrum was also observed by Ma *et al.* [27].

3.3. Morphological study

The morphology of as prepared PPy nanofiber was analyzed through SEM and TEM. The SEM image of PPy nanofiber (Figure 4a) shows the fiber like morphology. It shows a random network of nanostructured PPy with the diameter ~100 nm. This porous network is superior for easy and fast electrolyte transport, which is the essential requirement for enhanced electrochemical properties of the electrode materials. However, for better understanding of the morphological change, we have shown SEM image of PPy prepared by in-situ polymerization, without SA, which shows granular structure (Figure 4b) [23]. Thus SEM analysis of PPy nanofiber confirms that SA plays an important role for the synthesis of PPy nanofiber. For further analysis we have done the TEM analysis of PPy nanofiber. Figure 5 shows the TEM image of PPy nanofiber, which clearly indicates that the composite consists of nanofibers with diameter of ~100 nm. The uniform network of PPy nanofiber is further confirmed by TEM.

3.4. Electrochemical properties

The electrochemical performances of various electrode materials depend not only on the nature, porosity, conductivity of the electrode materials but also on the nature of the electrolytes. The choice of electrolyte depends on several factors like resistance, capacitance, electrochemically stable potential window, manufacturing cost etc. [28]. However, among organic and aqueous electrolytes, aqueous electrolytes are more superior for supercapacitors in terms of safety and cost. Further, aqueous electrolytes are environmentally benign. Here, we have chosen 1 M KCl and 1 M Na$_2$SO$_4$ solution as both are ecofriendly as well as cheaper and has the ability to serve as electrolytic solution for supercapacitors. Further, it is well established fact that the cycling behavior of the supercapacitors is superior in aqueous electrolyte as compared to organic electrolyte as it degrades in the electrode electrolyte interface in organic electrolyte [29]. Figure 6a, 6b

Figure 3. FTIR spectrum of PPy, SA, PPy nanofiber
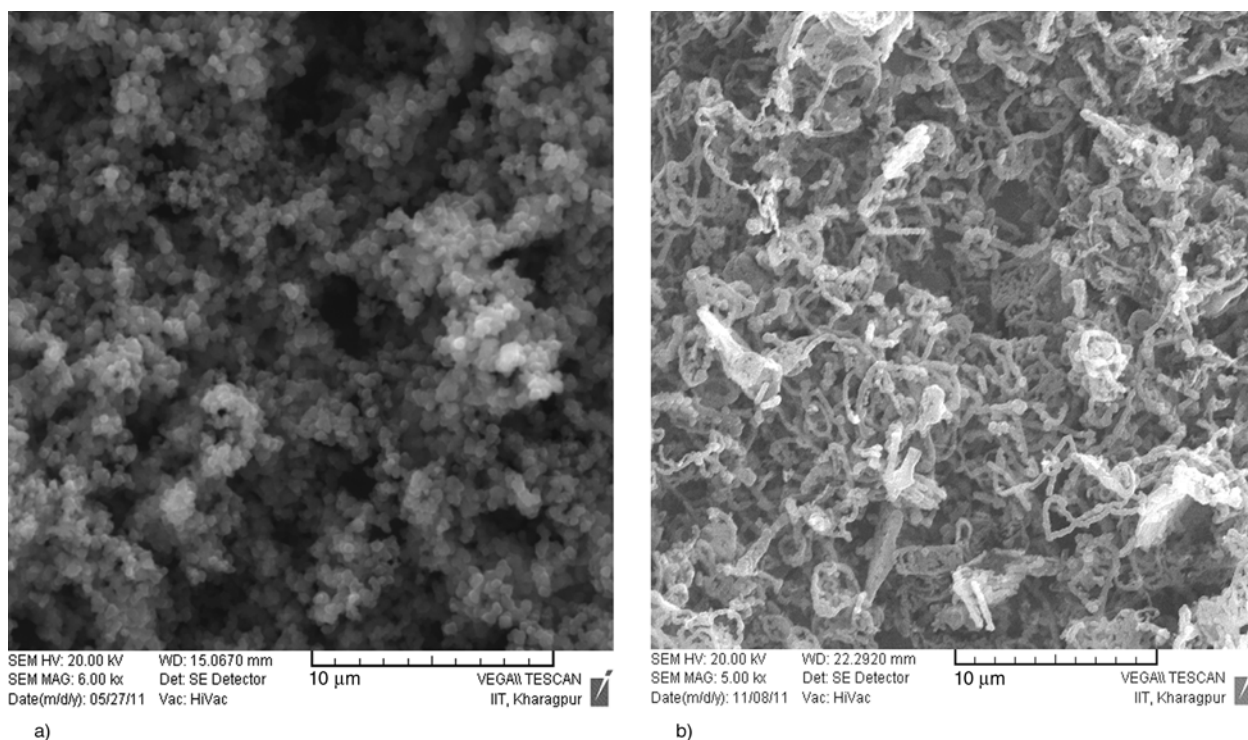
Figure 4. SEM images of (a) PPy without SA (granullar morphology) and (b) PPy nanofiber (fibrillar morphology)
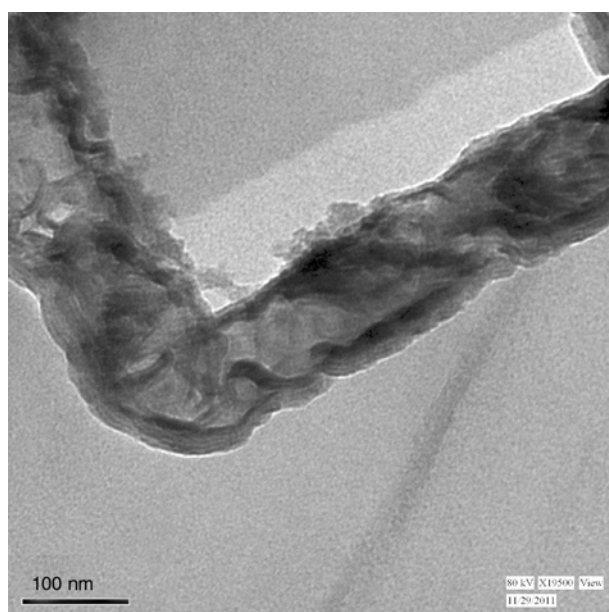
Figure 5. TEM image of PPy nanofiber

shows the CV curves of PPy nanofiber in 1 M KCl and 1 M Na_2SO_4 solution respectively. The non-rectangular shape of CV curves designates the redox behavior due to broad pore size distribution. The wide area of the CV curves implies the pseudocapacitive performance of the PPy nanofiber. On the other hand, in case of Na_2SO_4, the CV curve deviates from the ideal rectangular shape with some redox peaks (in between –0.6 to –0.4), which is also

an indication of pseudocapacitance properties of the PPy nanofiber.

In order to find the prospect of the composites to be used as electrode materials for supercapacitors, constant current charging/discharging (CCD) analysis was performed at 1 A/g. CCD test is the common tool to compare the relative cycling efficiency among different capacitors. This test is an indicator of the quality of supercapacitors. The CCD curves of PPy nanofiber in different electrolytes are shown in Figure 7a, 7b. The curves are linear as well as symmetrical, which is a typical characteristic of ideal capacitor [30]. The specific capacitance of the composite was calculated from the discharge cycle of the typical voltage-time response curve in CC measurements using Equation (1) [31, 32]:

$$C_{cc} = \frac{I \cdot \Delta t}{\Delta V \cdot m} \tag{1}$$

where C_{cc} is the specific capacitance obtained from discharge cycle of constant current charge/discharge measurements, I is the constant current, Δt is the discharge time, ΔV denotes the potential range and m is the mass of the sample. PPy nanofiber shows maximum capacitance of 284 F/g in KCl electrolyte. This value is higher than that of pure PPy, synthesized by in-situ oxidative polymeriza-
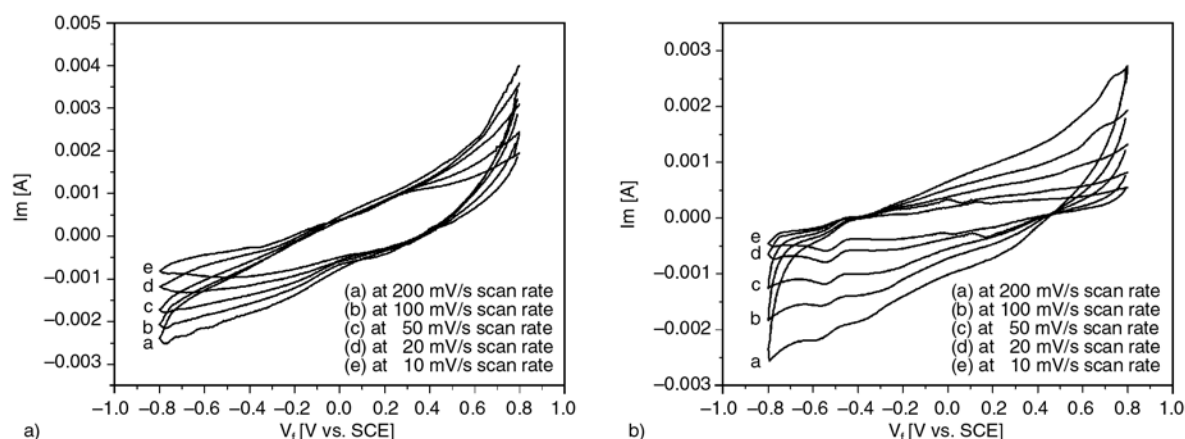
Figure 6. Cyclic voltammograms of PPy nanofiber in (a) 1 M KCl and (b) 1 M Na$_2$SO$_4$ solution
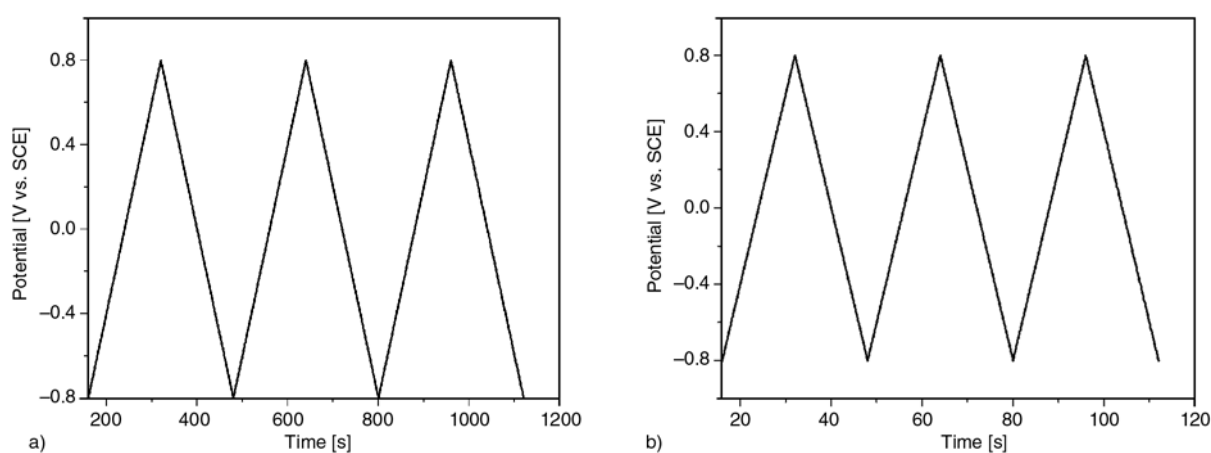

Figure 7. CCD curves of PPy nanofiber in (a) 1 M KCl and (b) 1 M Na$_2$SO$_4$ electrolyte

tion method and reported earlier [23]. Further, as prepared composite shows enhanced capacitance value than several PPy based electrode materials for supercapacitors, reported in the literatures [33–35]. On the other hand, it shows lower specific capacitance of 148 F/g in Na$_2$SO$_4$ electrolyte. The enhanced specific capacitance of PPy nanofiber may be due to the network structure, which enhances the surface area of the redox reaction and shortens the distance of electrolyte ions transport [21]. Further, the improved capacitance properties of the electrode material in KCl electrolyte as compared to Na$_2$SO$_4$ electrolyte may be explained by the following way – the hydrated ionic radius of K$^+$ (3.31 Å) is smaller than the hydrated ionic radius of Na$^+$ (3.58 Å), which allows it's easier and faster accessibility into the inner surface of the electrode materials as compared to Na$^+$ [36].

The cyclic stability test of PPy nanofiber in different electrolytes was conducted up to 600 cycles. The variation in specific capacitance with cycle
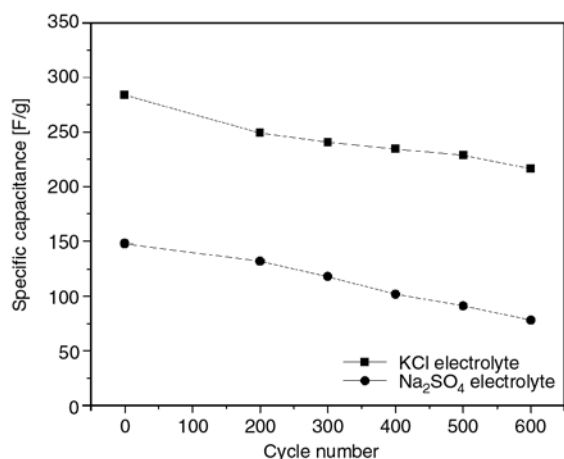
Figure 8. Specific capacitance *vs*. cycle number curve of PPy nanofiber in different electrolytes

number is shown in Figure 8. It shows 76% capacitance retention after 600 cycles in KCl electrolyte. Whereas this retention of capacitance decreases to 53%, when 1 M Na$_2$SO$_4$ was used as electrolyte. The variation in cyclic stability of composite material in different electrolytes may be caused by the doping

and de-doping of the electrode material, which allows the material to experience swelling and shrinkage and cause mechanical stress to the polymeric backbone. However, the enhanced cyclic stability may be due to the intermolecular interaction (Hydrogen Bonding) between SA and PPy chains, which restrict the change of regular network structure during the cyclic test and prevents the shrinkage and swelling of nanostructured polymer [21].

3.5. Electrochemical Impedance Spectroscopy (EIS)

EIS is one of the spectroscopic techniques, which measures the dielectric properties of any substance as a function of frequency. Basically, data obtained from EIS can be expressed through Bode plot or Nyquist plot. Nyquist plot is the plot of imaginary part of the impedance (Z') versus real part of impedance (Z''). High frequency intercept of the real part of impedance gives the solution resistance (R_s) of the composite. Depressed semicircle in the higher frequency region indicates the charge transfer resistance (R_{ct}), which arises mainly due to the charge transfer processes of the electrode materials. On the other hand imperfectness of the supercapacitive materials can be expressed by Constant Phase Element (CPE). The CPE can be expressed by the Equation (2) [31, 32]:

$$Z_{CPE} = \left[Q^0 (j\omega)^n \right]^{-1} \qquad (2)$$

where Q^0 is the frequency independent constant related to the surface and electroactive substance, ω represents the angular frequency ($\omega = 2\pi f$). On the other hand, n value arises from the slope of $\log Z$ versus $\log f$. Depending on this n value, CPE shows different responses. If n value = 0 represents the resistance, whereas n value = 1 represents ideal capacitor response, which is impossible to obtain in real world. Further n value = 0.5 indicates the Warburg behavior. However, n value > 0.5 represents moderate capacitor behavior [31, 32, 37–39].

Figure 9a, 9b demonstrates the Nyquist plots (fitted) of PPy nanofiber in both the electrolytes. Generally ESR is determined from the x-intercept of the Nyquist plot. This data indicates the rate by which supercapacitor can be changed/discharged [40]. PPy nanofiber shows low ESR (~1 Ω) in both the electrolytes. Lower R_s value indicates the enhanced conductivity as well as improved capacitive properties. The interpretation of the impedance spectra mainly carried out by fitting the experimental impedance spectra with an equivalent electrical circuit. The appropriate equivalent circuit for fitting the impedance spectra of PPy nanofiber in different electrolytes is shown in Figure 10. The fitting data of the composite in two electrolytes are shown in Table 1. In both the electrolytes we found n value > 0.5, which indicates moderate capacitor behavior. However, it is observed that, PPy nanofiber shows higher n value (0.714) in KCl electrolyte as compared to that in Na_2SO_4 electrolyte (0.556). The difference

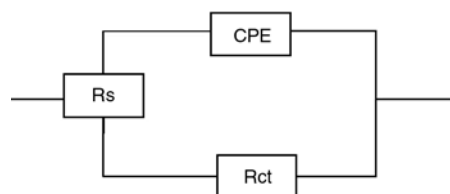**Figure 10.** Equivalent electrical circuit used in EIS fitting data

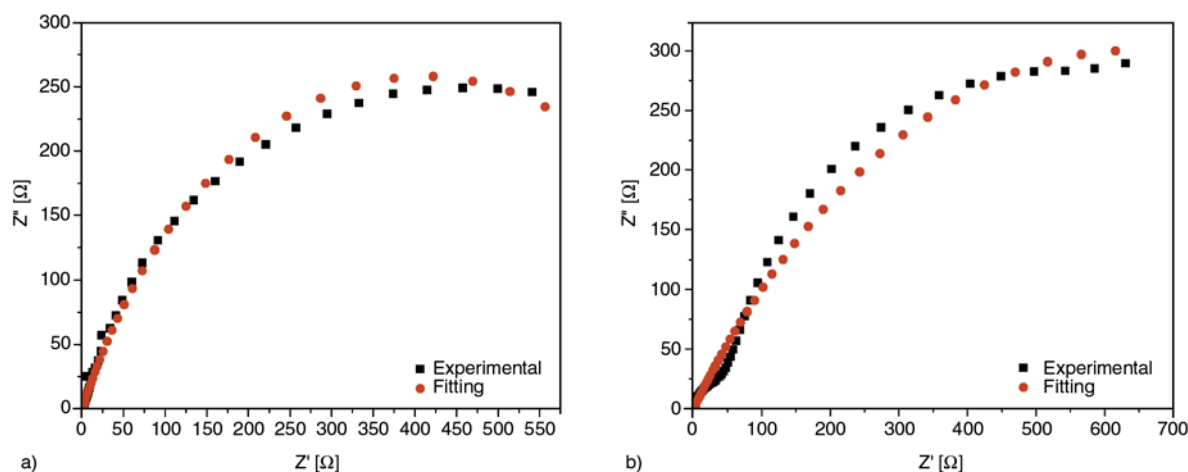**Figure 9.** Nyquist plots of PPy nanofiber in (a) 1 M KCl and (b) 1 M Na_2SO_4 electrolyte

Table 1. Fitting data for equivalent circuit elements of PPy/SA composite

Electrolyte	R_s [Ω]	R_{ct} [Ω]	CPE (S-s^n) $\cdot 10^{-3}$	n
1 M Na$_2$SO$_4$	1.24	1.29	1.08	0.556
1 M KCl	1.002	0.82	0.66	0.714

in *n* value in different electrolytes may arise due to several factors like variation of porosity in different electrolytes, dynamic disorder and diffusion etc.

4. TGA analysis

The thermal behavior of the PPy nanofiber was analyzed by TGA analysis. Figure 11 shows the TGA curves of SA, PPy nanofiber and pure PPy (without SA). The initial mass loss of all the samples at around 100°C arises due to the deintercalation of water. For SA, a sharp weight loss is observed at 253°C, which is due to the decomposition of alginate. However, in case of PPy nanofiber, the decomposition of alginate arises at ~270°C. Hence, the decomposition temperature of alginate in PPy nanofiber is higher than that of SA, which clearly indicates the interaction between SA and PPy. On the other hand, 20% weight loss was observed at 322°C for PPy nanofiber, where as pure PPy showed at 260°C. However the TGA curve clearly indicates higher thermal stability of PPy nanofiber as compared to PPy, without SA [23]. This enhanced thermal stability may be due to the formation of hydrogen bonds between SA and PPy chains. The enhanced thermal stability makes the nanofiber suitable for high temperature device applications.
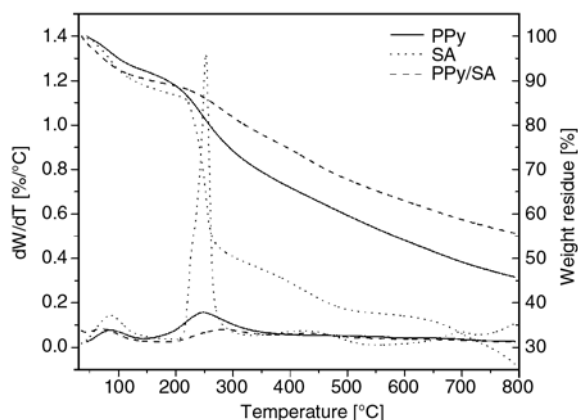
Figure 11. TGA curves of PPy, SA, PPy nanofiber

5. Conclusions

We have proposed a simple ecofriendly synthetic procedure to prepare PPy nanofiber by using SA as template. The morphological study of the composite shows fiber like network. It demonstrates superior electrochemical performances in KCl electrolyte as compared to Na$_2$SO$_4$ electrolyte due to the formation of regular network structure between PPy and SA. Further enhanced thermal stability of the nanofiber allows it to be used in high temperature device application. Moreover, the nanofiber shows enhanced capacitance as well as improved cyclic stability due to the intermolecular interaction bet SA and PPy. Overall this approach provides an inexpensive and facile way to prepare a supercapacitive electrode material using conducting polymer. Further Optimization of the experimental can improve the electrochemical performances of the electrode.

Acknowledgements

References

[1] Gao J., Sansiñena J-M., Wang H-L.: Tunable polyaniline chemical actuators. Chemistry of Materials, **15**, 2411–2418 (2003).
DOI: 10.1021/cm020329e

[2] Wu C-G., Bein T.: Conducting polyaniline filaments in a mesoporous channel host. Science, **264**, 1757–1759 (1994).
DOI: 10.1126/science.264.5166.1757

[3] Yu Y., Zhihuai S., Chen S., Bian C., Chen W., Xue G.: Facile synthesis of polyaniline–sodium alginate nanofibers. Langmuir, **22**, 3899–3905 (2006).
DOI: 10.1021/la051911v

[4] Wu T-M., Chang H-L., Lin Y-W.: Synthesis and characterization of conductive polypyrrole/multi-walled carbon nanotubes composites with improved solubility and conductivity. Composites Science and Technology, **69**, 639–644 (2009).
DOI: 10.1016/j.compscitech.2008.12.010

[5] Wu T-M., Lin S-H.: Synthesis, characterization, and electrical properties of polypyrrole/multiwalled carbon nanotube composites. Journal of Polymer Science Part A: Polymer Chemistry, **44**, 6449–6457 (2006).
DOI: 10.1002/pola.21724

[6] Ikegame M., Tajima K., Aida T.: Template synthesis of polypyrrole nanofibers insulated within one-dimensional silicate channels: Hexagonal versus lamellar for recombination of polarons into bipolarons. Angewandte Chemie International Edition, **42**, 2154–2157 (2003).
DOI: 10.1002/anie.200250800

[7] He J., Chen W., Xu N., Li L., Li X., Xue G.: SERS studies on the ordered structure of the surface of polypyrrole nanotubules. Applied Surface Science, **221**, 87–92 (2004).
DOI: 10.1016/S0169-4332(03)00810-9

[8] Athawale A. A., Katre P. P., Bhagwat S. V., Dhamane A. H.: Synthesis of polypyrrole nanofibers by ultrasonic waves. Journal Applied Polymer Science, **108**, 2872–2875 (2008).
DOI: 10.1002/app.27301

[9] Burke A.: Ultracapacitors: Why, how, and where is the technology. Journal of Power Sources, **91**, 37–50 (2000).
DOI: 10.1016/S0378-7753(00)00485-7

[10] Zang J., Li C. M., Bao S-J., Cui X., Bao Q., Sun C. Q.: Template-free electrochemical synthesis of superhydrophilic polypyrrole nanofiber network. Macromolecules, **41**, 7053–7057 (2008).
DOI: 10.1021/ma801345k

[11] Winter M., Brodd R. J.: What are batteries, fuel cells, and supercapacitors? Chemical Reviews, **104**, 4245–4269 (2004).

[12] Kötz R., Carlen M.: Principles and applications of electrochemical capacitors. Electrochimica Acta, **45**, 2483–2498 (2000).
DOI: 10.1016/S0013-4686(00)00354-6

[13] Qu D., Shi H.: Studies of activated carbons used in double-layer capacitors. Journal of Power Sources, **74**, 99–107 (1998).
DOI: 10.1016/S0378-7753(98)00038-X

[14] An K. H., Kim W. S., Park Y. S., Moon J-M., Bae D. J., Lim S. C., Lee Y. S., Lee Y. H.: Electrochemical properties of high-power supercapacitors using single-walled carbon nanotube electrodes. Advanced Functional Materials, **11**, 387–392 (2001).
DOI: 10.1002/1616-3028(200110)11:5<387::AID-ADFM387>3.0.CO;2-G

[15] Li Y., van Zijll M., Chiang S., Pan N.: KOH modified graphene nanosheets for supercapacitor electrodes. Journal of Power Sources, **196**, 6003–6006 (2011).
DOI: 10.1016/j.jpowsour.2011.02.092

[16] Acik M., Baristiran C., Sonmez G.: Highly surfaced polypyrrole nano-networks and nano-fibers. Journal of Materials Science, **41**, 4678–4683 (2006).
DOI: 10.1007/s10853-006-0034-7

[17] Lang X., Hirata A., Fujita T., Chen M.: Nanoporous metal/oxide hybrid electrodes for electrochemical supercapacitors. Nature Nanotechnology, **6**, 232–236 (2011).
DOI: 10.1038/nnano.2011.13

[18] Aricò A. S., Bruce P., Scrosati B., Tarascon J-M., van Schalkwijk W.: Nanostructured materials for advanced energy conversion and storage devices. Nature Materials, **4**, 366–377 (2005).
DOI: 10.1038/nmat1368

[19] Mastragostino M., Arbizzani C., Soavi F.: Polymer-based supercapacitors. Journal of Power Sources, **97**, 812–815 (2001).
DOI: 10.1016/S0378-7753(01)00613-9

[20] Gupta V., Miura N.: High performance electrochemical supercapacitor from electrochemically synthesized nanostructured polyaniline. Materials Letters, **60**, 1466–1469 (2006).
DOI: 10.1016/j.matlet.2005.11.047

[21] Li Y., Zhao X., Xu Q., Zhang Q., Chen D.: Facile preparation and enhanced capacitance of the polyaniline/sodium alginate nanofiber network for supercapacitors. Langmuir, **27**, 6458–6463 (2011).
DOI: 10.1021/la2003063

[22] Kuila B. K., Nandan B., Böhme M., Janke A., Stamm M.: Vertically oriented arrays of polyaniline nanorods and their super electrochemical properties. Chemical Communication, **2009**, 5749–5751 (2009).
DOI: 10.1039/B912513B

[23] Sahoo S., Karthikeyan G., Nayak G. C., Das C. K.: Electrochemical characterization of in situ polypyrrole coated graphene nanocomposites. Synthetic Metals, **161**, 1713–1719 (2011).
DOI: 10.1016/j.synthmet.2011.06.011

[24] Zhang G. Q., Zha L. S., Zhou M. H., Ma J. H., Liang B. R.: Preparation and characterization of pH- and temperature-responsive semi–interpenetrating polymer network hydrogels based on linear sodium alginate and crosslinked poly(*N*-isopropylacrylamide). Journal of Applied Polymer Science, **97**, 1931–1940 (2005).
DOI: 10.1002/app.21957

[25] Bose S., Kuila T., Uddin M. E., Kim N. H., Lau A. K. T., Lee J. H.: In-situ synthesis and characterization of electrically conductive polypyrrole/graphene nanocomposites. Polymer, **51**, 5921–5928 (2010).
DOI: 10.1016/j.polymer.2010.10.014

[26] Çaykara T., Demirci S., Eroğlu M. S., Güven O.: Poly (ethylene oxide) and its blends with sodium alginate. Polymer, **46**, 10750–10757 (2005).
DOI: 10.1016/j.polymer.2005.09.041

[27] Ma G., Fang D., Liu Y., Zhu X., Nie J.: Electrospun sodium alginate/poly(ethylene oxide) core–shell nanofibers scaffolds potential for tissue engineering applications. Carbohydrate Polymers, **87**, 737–743 (2012).
DOI: 10.1016/j.carbpol.2011.08.055

[28] Tanahashi I., Yoshida A., Nishino A.: Comparison of the electrochemical properties of electric double-layer capacitors with an aqueous electrolyte and with a non-aqueous electrolyte. Bulletin of the Chemical Society of Japan, **63**, 3611–3614 (1990).
DOI: 10.1246/bcsj.63.3611

[29] Chen W., Rakhi R. B., Alshareef H. N.: High energy density supercapacitors using macroporous kitchen sponges. Journal of Materials Chemistry, **22**, 14394–14402 (2012).
DOI: 10.1039/C2JM32030D

[30] Yan J., Wei T., Shao B., Ma F., Fan Z., Zhang M., Zheng C., Shang Y., Qian W., Wei F.: Electrochemical properties of graphene nanosheet/carbon black composites as electrodes for supercapacitors. Carbon, **48**, 1731–1737 (2010).
DOI: 10.1016/j.carbon.2010.01.014

[31] Chen W-C., Wen T-C.: Electrochemical and capacitive properties of polyaniline-implanted porous carbon electrode for supercapacitors. Journal of Power Sources, **117**, 273–282 (2003).
DOI: 10.1016/S0378-7753(03)00158-7

[32] Sahoo S., Karthikeyan G., Nayak G. C., Das C. K.: Modified graphene/polyaniline nanocomposites for supercapacitor application. Macromolecular Research, **20**, 415–421 (2012).
DOI: 10.1007/s13233-012-0042-1

[33] Qu Q., Zhang P., Wang B., Chen Y., Tian S., Wu Y., Holze R.: Electrochemical performance of MnO_2 nanorods in neutral aqueous electrolytes as a cathode for asymmetric supercapacitors. Journal of Physical Chemistry C, **113**, 14020–14027 (2009).
DOI: 10.1021/jp8113094

[34] Hu C-C., Chu C-H.: Electrochemical impedance characterization of polyaniline-coated graphite electrodes for electrochemical capacitors – Effects of film coverage/thickness and anions. Journal of Electroanalytical Chemistry, **503**, 105–116 (2001).
DOI: 10.1016/S0022-0728(01)00385-0

[35] Piao T., Park S-M., Doh C-H., Moon S-I.: Intercalation of lithium ions into graphite electrodes studied by AC impedance measurements. Journal of the Electrochemical Society, **146**, 2794–2798 (1999).
DOI: 10.1149/1.1392010

[36] Levi M. D., Aurbach D.: Simultaneous measurements and modeling of the electrochemical impedance and the cyclic voltammetric characteristics of graphite electrodes doped with lithium. Journal of Physical Chemistry B, **101**, 4630–4640 (1997).
DOI: 10.1021/jp9701909

[37] Ingram M. D., Staesche H., Ryder K. S.: 'Activated' polypyrrole electrodes for high-power supercapacitor applications. Solid State Ionics, **169**, 51–57 (2004).
DOI: 10.1016/j.ssi.2002.12.003

[38] Jurewicz K., Delpeux S., Bertagna V., Béguin F., Frackowiak E.: Supercapacitors from nanotubes/polypyrrole composites. Chemical Physics Letters, **347**, 36–40 (2001).
DOI: 10.1016/S0009-2614(01)01037-5

[39] Sun W., San S., Duo Y., Chen Y.: Preparation and characterization of micro polypyrrole electrodes for supercapacitor. Advanced Materials Research, **60–61**, 375–379 (2009).
DOI: 10.4028/www.scientific.net/AMR.60-61.375

[40] Wang Y., Shi Z., Huang Y., Ma Y., Wang C., Chen M., Chen Y.: Supercapacitor devices based on graphene materials. Journal of Physical Chemistry C, **113**, 13103–13107 (2009).
DOI: 10.1021/jp902214f

Epoxy/PCL nanocomposites:
Effect of layered silicate on structure and behavior

J. Rotrekl, L. Matějka, L. Kaprálková, A. Zhigunov, J. Hromádková, I. Kelnar[*]

Institute of Macromolecular Chemistry, Academy of Sciences of the Czech Republic, Heyrovsky Sq. 2, 162 06 Prague, Czech Republic

Abstract. The effect of clay-induced morphological transitions on the structure formed in the course of reactively induced phase separation (RIPS) and its impact on the properties of epoxy/polycaprolactone (PCL) nanocomposites were studied. The effect of organophilized montmorillonite on the behavior of epoxy containing 5–30% PCL was strongly dependent on the epoxy/PCL system composition. With a supercritical 20% PCL content, the increasing amounts of clay led to changes in the morphology that produced phase inversion, causing radical changes in the mechanical behavior. The main effect of the clay, which was located preferentially in the epoxy, was to influence the significant dynamic asymmetry (and thus the phase behavior). The simultaneous pinning effect of the clay on the phase separation changed the composition and parameters of the coexisting phases. The evaluation of the structure-properties relationship indicated the significant potential for nanoclays to control the behavior of thermoplastic- modified epoxy systems.

Keywords: nanocomposites, epoxy, mechanical properties, microstructure, phase separation

1. Introduction

The use of engineering thermoplastic polymers [1–5] to enhance and balance the mechanical properties of epoxy resins has been investigated as an alternative to liquid rubber toughening [6] since the 1980s. The application of engineering thermoplastics like polyether ether ketone (PEEK) [1], polyether sulphone (PES) [2], polyether imide (PEI) [3, 4], and polybutylene terephatlate (PBT) [5] can enhance toughness of epoxies with less marked reduction of their other properties. The primary shortcoming is the increase in viscosity that limits the content of the modifier. An increasing number of studies have indicated not only that nanofillers (NF) can compensate for the stiffness reduction of impact-modified polymeric systems but also that a suitable combination of NF and a polymeric modifier can also provide a synergistic effect (e.g., further increasing the material toughness) [7–16]. The enhanced efficiency of impact modifiers allows their content to be reduced. This effect was observed in both immiscible thermoplastic systems [7–9] and epoxies with two phase structures formed by the reaction-induced phase separation (RIPS) [10] of a modifier dissolved in an uncured resin. The enhanced mechanical performance of epoxy systems was mostly observed in liquid rubbers and clays [11–13] and in combinations of thermoplastics (PEEK, PEI, PES, ABS) and clays [14–20]. The synergistic effect of the nanofiller consists in its complex effect on the multiphase system by reinforcement, leading also to a change in the component parameter profile combined with a significant influence on the structure and parameters of the interface. The NF influences the structure by affecting the dynamic phase behavior in the case of immiscible thermoplastics [7–9]

---

and the phase separation (including RIPS) that occurs in thermosets. In both cases, the change of morphology type and dimension, including the formation of complex structures, is accompanied by an influence on the interface and crystallinity parameters [19].

The effect of inorganic particles on the structure of multiphase polymers has been demonstrated in both experimental and theoretical studies [21–24]. Generally, fillers can support the initiation of phase separation [24–26] (e.g., by composition [25] fluctuations due to preferential wetting of one polymer phase on the filler surface [26]), and they also have a pinning effect during the subsequent separation because they increase the viscosity, blocking mass transfer [23, 27–29] in the system. Especially in the case of RIPS, separation can also be influenced by NF-induced effects on the crosslinking reaction kinetics [30].

The combination of a low T_g and low viscosity epoxy with a dissolved high T_g and high molecular weight thermoplastic polymer represents a system with significant dynamic asymmetry (i.e., a system in which the phase separation is strongly influenced by viscoelastic effects) [31–34]. As a result, relatively unexpected complex phase separations occur, which are strongly time and temperature dependent. The variation in the component molecular weight can be an effective tool to generate favorable structures (e.g., fine particles for elastomers and co-continuous structures for thermoplastic tougheners in epoxy). The advantage of reactive systems is that these structures may be fixed by vitrification and gelation. The comprehensive influence of nanofillers on polymers offers significant potential for nanofiller (NF) to affect the viscoelastic phase separation. This possibility has been demonstrated in several studies [14–16]. Strong NF effects on the epoxy/PEI system were shown by Peng and cooworkers [14, 16], and the effect of attapulgite on the structure of the epoxy/ PES system was demonstrated by Zhao *et al.* [35].

The existing studies of epoxy and thermoplastics have focused only on one modifier concentration or a limited composition range, and some lack descriptions of the effects of NF on the structure or fail to evaluate the mechanical behavior.

Based on our results indicating the importance of montmorillonite (MMT) content in epoxy and liquid rubber [11, 12], this study focuses on a more detailed description of the relationship between the structure and properties of epoxy containing 5–30% PCL. The reason for the choice of semicrystalline PCL with relatively low mechanical behavior is the well-described phase behavior [40–42] of epoxy/PCL systems and the reported potential to upgrade epoxy [36, 37]. Moreover, in the selected Diglycidyl ether of bisphenol A/diaminodiphenyl sulfone (DGEBA/ DDS) system, the phase separation proceeds above the melting point of PCL. A further advantage of this semi-model system is the relatively easy dissolution of PCL in epoxy (Lower critical solution temperature – LCST) and the fair phase contrast in optical microscopy, which is necessary for a more comprehensive study of the effect of MMT on RIPS, which would constitute a continuation of this work.

2. Experimental
2.1. Materials
Cloisite C30 B (MMT modified with methyl tallow bis(2-hydroxyethyl) quaternary ammonium chloride) was obtained from Southern Clay Products, Inc. (Gonzales, Texas, USA). Polycaprolactone (PCL) m.w. 40000 was obtained from Perstorp (Perstorp, Sweden). Diglycidyl ether of bisphenol A (DGEBA)-based epoxy resin Epilox A19-02 (epoxy equivalent weight 185–200 g, m.w. 396 g/mol) Leuna-Harze GmbH (Leuna, Germany), amine hardener diaminodiphenyl sulfone (DDS) Aldrich (St. Louis, Missouri, USA).

2.2. Preparation of epoxy hybrid composites
The epoxy nanocomposites were prepared using a rotary mixer with an evacuated chamber. Clay and PCL were mixed with epoxy resin at 130°C for 60 min. Then the curing agent was added, and the mixing continued for 10 min at the same temperature. Test specimens (1.5 mm thick dog-bone with the working part length of 40 mm and width of 4 mm and unnotched Charpy bars $80 \times 10 \times 4$ mm^3) were prepared by casting the sample into a steel mold and curing at 170°C for 4 hours.

2.3. Testing
The tensile strength tests were carried out at 22°C using an Instron 5800 apparatus at a crosshead speed of 1 mm/min. At least eight specimens were tested for each sample. The stress at break (σ_B, vari-

ation coefficient <2%) and Young's modulus (*E*, variation coefficient <6%) were evaluated. The impact strength was measured using a Zwick hammer (Charpy) with an energy of 4 J (variation coefficient <11%). The reported values are the averages of ten measurements.

Dynamic mechanical analysis (DMA) was performed with an ARES apparatus (Rheometric Scientific, Piscataway, NJ). T_g was determined from the maximum of the loss modulus E'', which was measured as a function of temperature at a frequency of 1 Hz. Chemorheological experiments to characterize the time to gel point during curing at 170°C were conducted in the parallel-plate geometry using oscillatory shear deformation at a frequency of 6.28 rad/s (1 Hz) using the same equipment.

2.4. Morphological observations

The phase structure of the cryofractured samples was observed using scanning electron microscopy (SEM). The PCL phase was etched with tetrahydrofuran for 1 h. The size of the dispersed particles was evaluated from the micrographs (from 5 representative pictures containing approximately 100 particles) using a Mini Mop image analyzer (Kontron Co., Germany).

For transmission electron microscopy (TEM), ultrathin (60 nm) sections were cut using an Ultracut UCT (Leica) ultramicrotome. Wide-angle X-ray diffraction (WAXS) patterns were obtained with an HZG/4A powder diffractometer (Freiberger Präzisionsmechanik GmbH, Germany) and monochromatic CuKα radiation. The cloud point was determined from light transmission measurements.

3. Results and discussion

In this work, we have observed the effect of clay on phase separation during the formation of the DGEBA/DDS/PCL nanocomposite, as well as its final structure and mechanical properties.

3.1. Effect of clay on T_g

The phase separation of the system was characterized by changes in the T_g of the epoxy because the DMA test used to determine this value does not allow the T_g of PCL to be evaluated (not shown) at ~–50°C because of the dominance of the interfering secondary sub-T_g transition in the epoxy matrix.

Table 1. Effect of clay on glass transition temperature of epoxy phase and its dependence on PCL content

PCL content [wt%]	C30 content [wt%]			
	0	**0.5**	**1.5**	**3**
	T_g [°C]			
0	202.0	200.0	199.5	198.5
5	198.0	195.0	194.0	192.0
10	197.0	194.0	193.0	183.0
15	193.6	191.0	183.0	173.0
20	191.6	181.0	172.0	161.0
30	179.0	–	170.0	160.0

The results in Table 1 suggest that a decrease in the glass transition temperature (T_g) of the epoxy phase occurs at all compositions of epoxy/PCL and that the reduction is more significant as the clay content increases. At the same time, Table 1 clearly shows that the clay also decreases the T_g of neat epoxy.

Generally, nanofillers influence the T_g of polymer matrices by two contradictory effects [38, 39]: reduction of the chain mobility by interaction with the rigid nanofiller and (b) increase of the free volume because of the presence of the nanofiller and the loosened molecular packing of the chains. In the case of the rigid DGEBA-DDS network, the effect of the increased free volume dominates, leading to a decrease in the T_g.

Table 1 also shows that the decrease in T_g is more significant for all PCL-containing nanocomposites than the MMT-induced decrease in the T_g of the single epoxy matrix. This result indicates that the extent of the phase separation (and the content of PCL dissolved in the epoxy phase due) is reduced because of the pinning effect [23] of the clay. Clearly, the pinning effect of clay (which occurs for all PCL content levels) is more apparent at higher PCL contents because of the greater mass transfer and viscosity of the system.

3.2. Effect of clay on structure

The results shown in Figures 1–5 indicate that the clay-induced structural transformations are strongly dependent on the PCL content.

In the case of subcritical [40, 41] (5 and 10 wt%) PCL content, SEM observation (Figures 1 and 2) shows a structure that consists of spherical PCL inclusions in an epoxy rich matrix. The increased clay content, which is preferentially localized in the epoxy (as indicated by TEM, not shown), has an unexpected
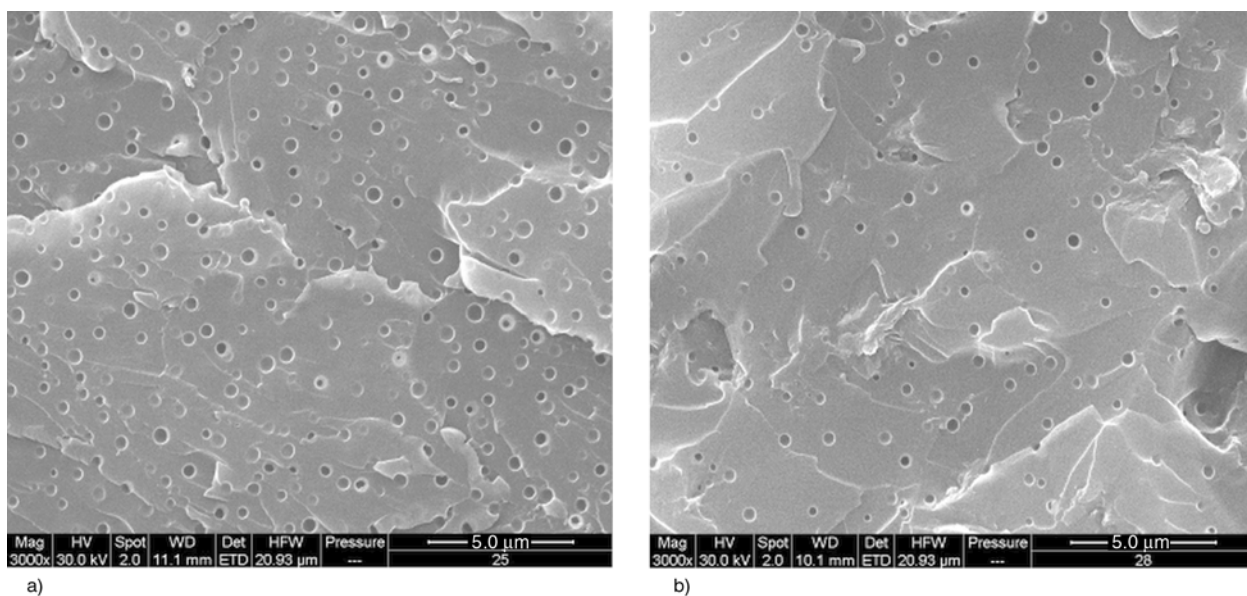
Figure 1. SEM image of epoxy/PCL 95/5 (w/w) containing (a) 0% clay (b) 3% clay
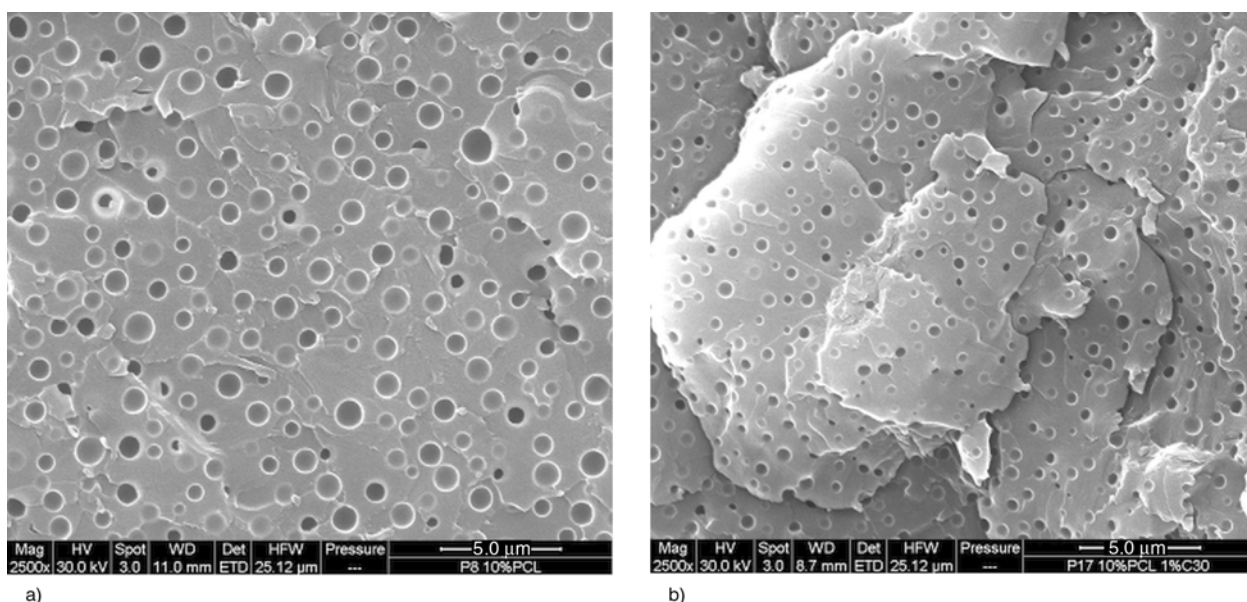
Figure 2. SEM image of 90/10 (a) 0% clay (b) 3% clay

effect on the structure. Figure 1 clearly shows that the increased clay content does not affect the particle size in the 95/5 epoxy/PCL system, which is approximately 500 nm in all cases. Instead, it leads to a reduction in the number of particles and a corresponding enlargement of the interparticle distance. This result seems to be a consequence of the pinning effect of the clay, causing a less-complete phase separation, as indicated by the lower T_g of the epoxy phase (Table 1). Surprisingly, the number of particles decreases, in spite of the expected higher nucleation of the phase separation [25] caused by the presence of clay.

At a 90/10 epoxy/PCL composition, a marked decrease in the size of the PCL inclusions (Figure 2a) with 0.5% clay content was observed, but there was no further effect of the increasing clay content on the size. This result indicates that the dominant pinning effect of the clay with its initial low content is balanced by other clay-induced effects, supporting particle growth with increasing clay content. These effects include clay nucleation [25], which leads to an earlier onset of phase separation [36] at lower conversion and viscosity, as well as a longer interval between the onset of phase separation and gelation [11].
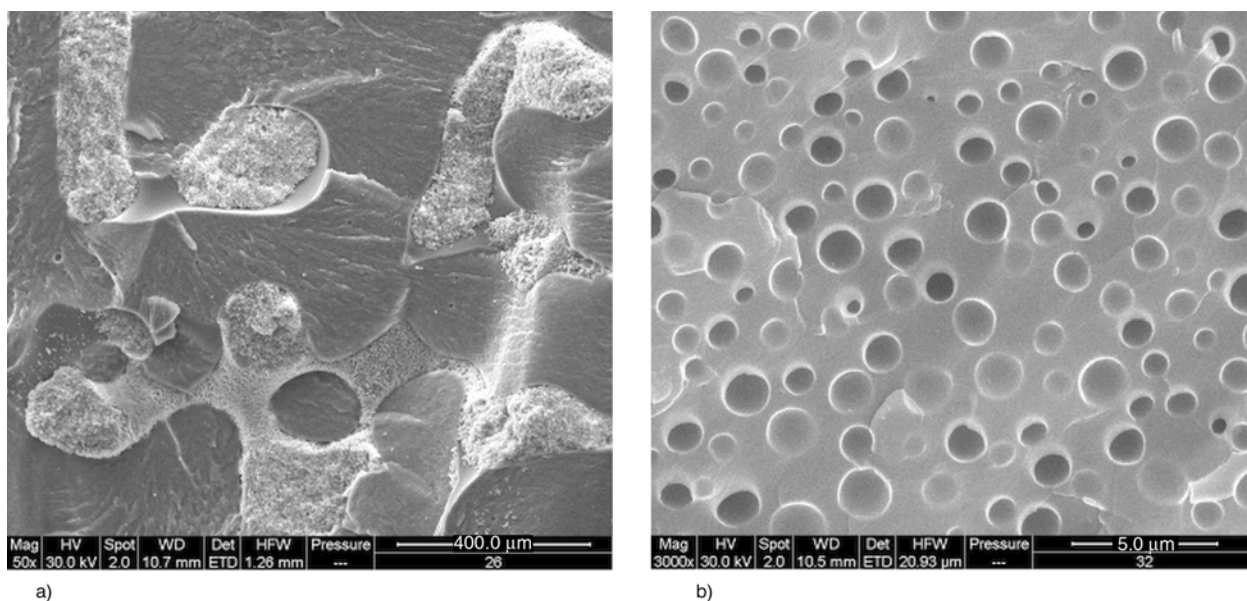
Figure 3. SEM image of 85/15 epoxy/PCL (w/w) with (a) 0% clay (b) 0.5% clay

These results represent a difference from epoxy/liquid rubber/clay systems [11, 12], in which an increase in particle size was found. This difference can be explained by the expected lower significance of the pinning effect of clay on the phase separation of the modifier as a result of the significantly lower molecular weight (i.e., in the system with the less significant asymmetry).

At supercritical (>12%) PCL content, the effect of the clay on the morphology is highly significant.

In the case of 85/15 epoxy/PCL without clay, SEM observation (Figure 3) shows a relatively rough bicontinuous structure that contains subinclusions of the second phase formed by the secondary phase separation. The PCL-rich phase contains relatively large epoxy globules (<10 µm), whereas the PCL inclusions in the epoxy are finer (<2 µm).

This structure quickly changes to that of continuous epoxy containing relatively fine PCL inclusions (~1 µm average size) at 0.5% clay addition. The PCL particles are further refined by the addition of greater clay contents because the larger amount of clay dispersed in the epoxy phase produces a more pronounced change in the dynamic asymmetry. This trend causes an earlier disruption of the initial (finer) bicontinuous structure [34], forming smaller particles whose growth is limited by the increased pinning effect of the clay.

The most significant structural transformation was found for the 80/20 system. The original structure, which had a continuous PCL-rich phase containing

approximately ~20 µm epoxy-rich particles (Figure 4a), is transformed to an epoxy-rich matrix with fine PCL-rich inclusions when the clay content is greater than 1.5% MMT (Figure 4c) (i.e., the clay causes a phase inversion). The size of the PCL inclusions further diminishes at 3% clay (not shown). In the cases of 0.5 and 1% C30 clay content, rough bicontinuous structures (Figure 4b) with subinclusions of the second phase were observed (approximately corresponding to the 85/15 system without clay in Figure 3a). The reason for this transformation is the lower mobility (higher viscosity) of the epoxy phase due to clay, supporting its continuity. The course of the structure changes with increasing clay content (Figure 4) resembles the time-evolution of the phase separation in an analogous system with a significant dynamic asymmetry caused only by the crosslinking of epoxy [40], but the sequence proceeds in the opposite order. In the case of the most complete separation without clay (Figure 4a), the structure corresponds to the initial stage of the phase separation evolution, [40] whereas in presence of clay and thus hindered separation, 'final' phase inverted structure occurs. As a result, this transformation of the structure by clay cannot be explained by mere 'freezing' [14] of the course of RIPS in the earlier stage.
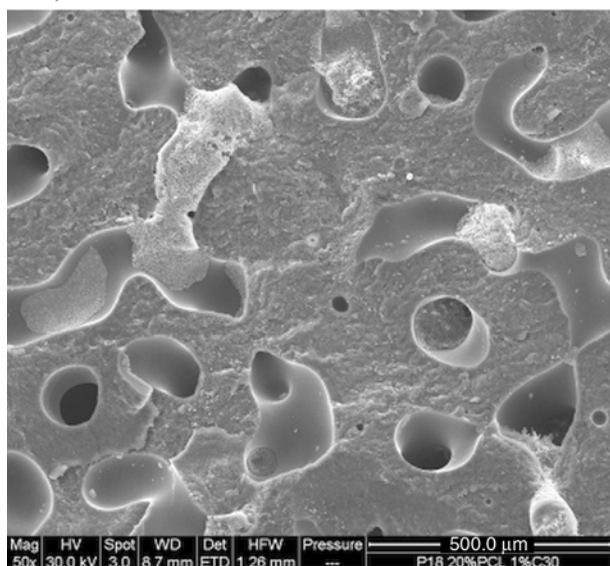
Consequently, it is clear that the clay changes the phase diagram (position of critical point) of this low critical solution temperature (LCST) system with significant dynamical asymmetry because it remark-
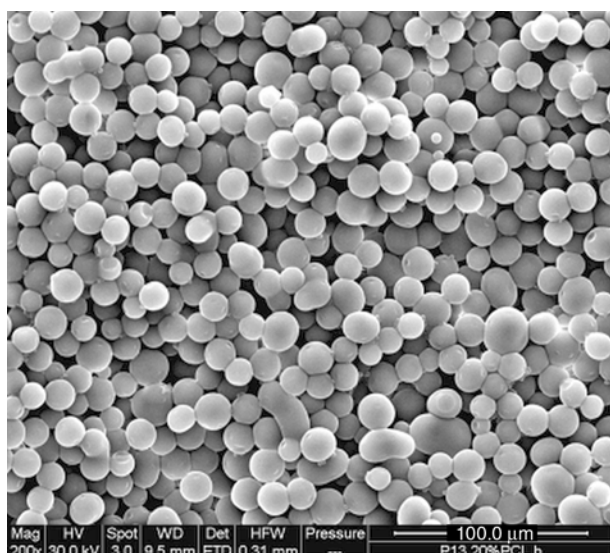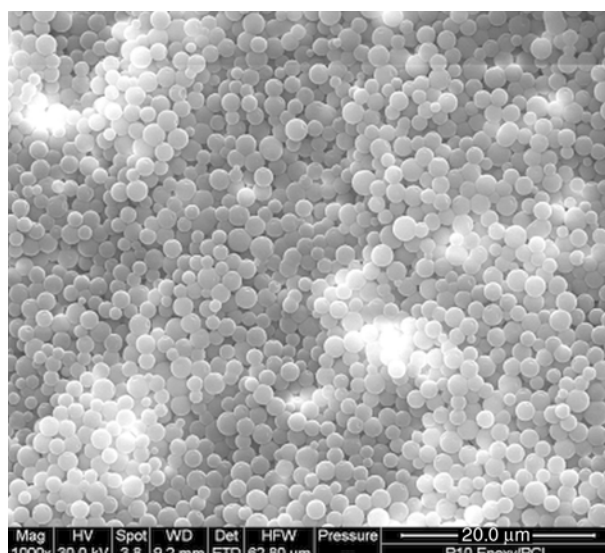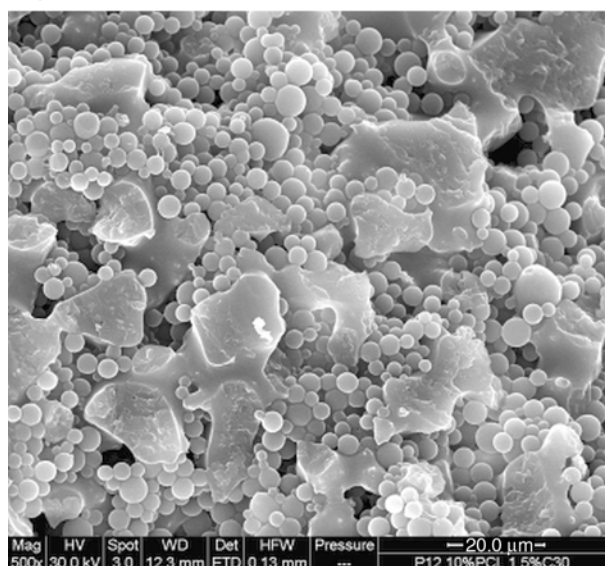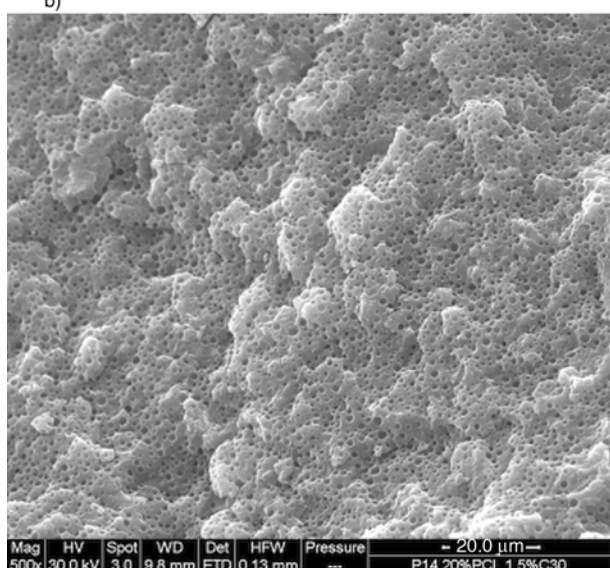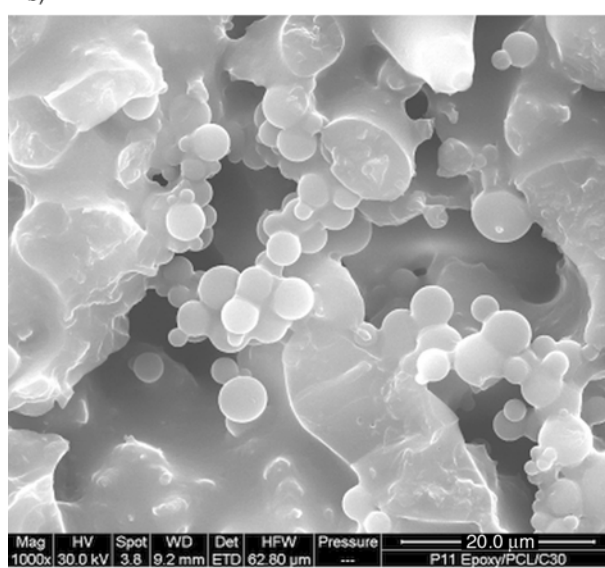
Figure 4. SEM image of 80/20 epoxy/PCL (w/w) with (a) 0% clay (b) 1% clay (c) 1.5% clay

Figure 5. SEM image of 70/30% epoxy/PCL (w/w) (a) 0% clay (b, c) 1.5% clay

ably alters the dynamic asymmetry caused by preferential clay localization inside the epoxy phase. The study of the effect of clay on the phase diagram is in progress. Observation of selected 80/20 samples at lower conversions indicates a self-similar development of the structures identified here (droplet like structures were formed immediately, without the appearance of a bicontinuous structure), at least at the conversion for which SEM observation was possible.

The marked effect of clay on the structure is also obvious in the 70/30 system (Figure 5). In this case, the original structure, consisting of a PCL matrix and closely stacked and partially interconnected epoxy globules, is transformed to a rough bicontinuous structure by the presence of clay. Figure 5a shows the relatively fine size of the epoxy globules (<4 μm) in comparison with those of the analogous 80/20 system (Figure 4a) as a consequence of the higher PCL content. Figure 5b, 5c show that the co-continuous PCL-rich phase contains interconnected epoxy particles, suggesting that the clay-enhanced viscosity of the epoxy (slowing the epoxy dynamics) leads to the dual continuity of the epoxy in both the relatively rough continuous epoxy-rich threads and the interconnected epoxy globules inside the continuous PCL-rich phase. It can be seen that the epoxy globules attached to the continuous epoxy phase are merged incompletely (Figure 5c), which seems to be a consequence of the different degree of curing in the epoxy-rich phase and in the globules formed in the PCL-rich phase [41]. Finally, the fact that the increased clay content does not lead to a continuous epoxy phase as it does in the 80/20 system is apparently a consequence of the high PCL content.

An important feature of all structures containing closely packed epoxy globules (Figures 4a, 4b and 5) is their at least partial interconnection, which is also documented by the fact that the structure was preserved, in spite of the PCL matrix extraction using tetrahydrofuran.

The above results clearly show that the effect of the clay on the dimensions of the PCL inclusions was small at low (subcritical) PCL content, for which phase separation was the expected nucleation and growth (NG) mechanism (i.e., dynamic asymmetry is less important because of the reduced extent of mass transfer). On the other hand, when the PCL content exceeded the critical concentration with expected spinodal decomposition (SD) [40] mechanism, the structure was significantly affected by the dynamic asymmetry [43], and the clay-induced change in this asymmetry led to a phase inversion. Consequently, the effect of the clay was similar to that of an increase in the molecular weight or the content of the epoxy rich phase (i.e., the component influenced by NF).

3.3. Mechanical properties

Because of the relatively low level of the mechanical properties of PCL, the goal of this work was to study the potential of NF to tailor the structure and properties at respective PCL concentrations rather than the achievement of highly enhanced mechanical properties of epoxy systems.

In the case the 95/5 epoxy/PCL matrix, Figure 6 clearly shows that best values of the strength and toughness occurred in the sample without added clay, in contrast to the systems with higher PCL contents and the analogous systems with different
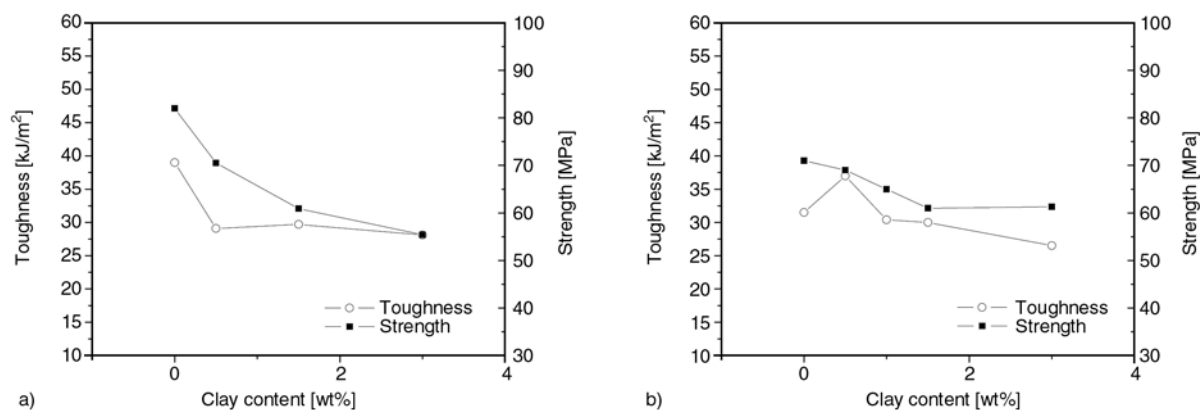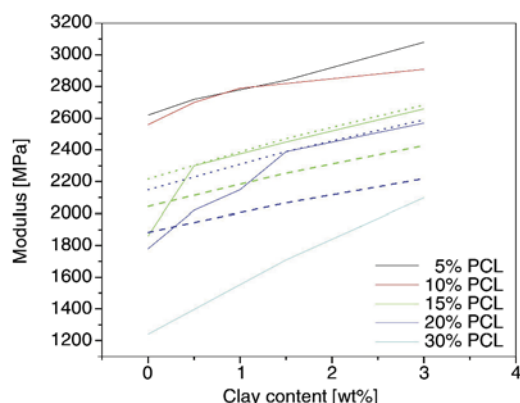

Figure 6. Effect of clay content on strength and toughness of epoxy containing (a) 5 wt% and (b) 10 wt% polycaprolactone
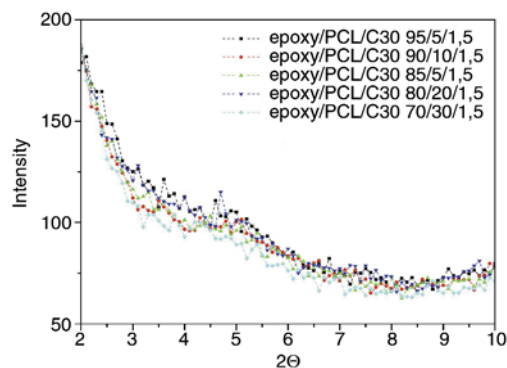
thermoplastic modifiers, which show the synergy of the clay/thermoplastic combination [14–17, 19]. The reduced properties in the presence of clay appear to be a consequence of the lower PCL content (and the resulting lower number of particles), as well as the related increase of the interparticle distance (Figure 1), especially when the low crystallinity of PCL the inclusions (<5 %) and the resulting significant rubbery character are considered. The lower content of the low-modulus inclusions should increase the strength, which seems to contradict the observed decrease. These results indicate a significant variation effect in the component parameter ratio [44], which is caused by the lower extent of phase separation indicated by both the reduced T_g of the epoxy and the lower PCL inclusion content.

As expected, the refinement of the PCL inclusion size with the addition of clay in the 90/10 epoxy/PCL blend has a minimal effect on the properties [45]. The simultaneous increase in the toughness with the addition of 0.5% clay indicates a synergistic effect caused by the clay, which is probably produced by the more favorable ratio of the component parameters (because of both the reinforcement of the epoxy by the clay and the changed composition of both components), as determined by the varying degree of phase separation.

From the dependence of the modulus on the clay content for both 5 and 10% PCL (Figure 7), it can be seen that the increased clay concentration leads to an expected increase in the modulus as a consequence of the hydrodynamic filler reinforcing effect


Figure 8. XRD patterns for epoxy/PCL containing 1.5% clay and their dependence on PCL content

Figure 7. Effect of clay content on modulus of epoxy with various PCL contents. Solid lines represent experimental values. The doted line of the same color represent corresponding Kerner model values and the dashed lines represent values calculated using co-continous model [46].

throughout the entire concentration range. This effect apparently exceeds the negative effect of the higher content of residual PCL indicated by the decrease of T_g with the addition of clay (Table 1). The XRD patterns of the samples (Figure 8) indicate a comparable degree of partial exfoliation for all epoxy/PCL matrix compositions (i.e., the reinforcing effect of clay is similar for all systems studied).

With 15 and 20% PCL, the initial PCL matrix and co-continuous structure transformed to an epoxy-rich matrix containing fine PCL domains with the addition of 0.5 and 1.5% clay for 15 and 20% PCL, respectively (Figures 3 and 4). This transition produced a radical increase of the strength and toughness of the blend (Figure 9). Interestingly, the best performance was found for an epoxy matrix with PCL inclusions, whereas the structures with a continuous PCL phase exhibited much lower levels of toughness and strength. The reason for this trend is the relatively poor mechanical behavior of PCL (in comparison with other thermoplastics) and the low volume of the PCL matrix between the high content of interconnected epoxy globules (Figure 4a) in the 80/20 system without clay. In the case of the 'intermediate' bicontinuous structure with low clay content (Figures 3b, 4b), the presence of both phases in the form of rough bulky threads exerted a negative effect on the mechanical properties of the blend. The toughness did not increase with further refinement of the PCL inclusions (in spite of their expected low modulus) because of the independence of the toughness on the particle size within this range [45]. The expected negative effect of clay on the toughness of the epoxy matrix and the changed ratio of the component parameters by the less complete phase separation must also be considered.
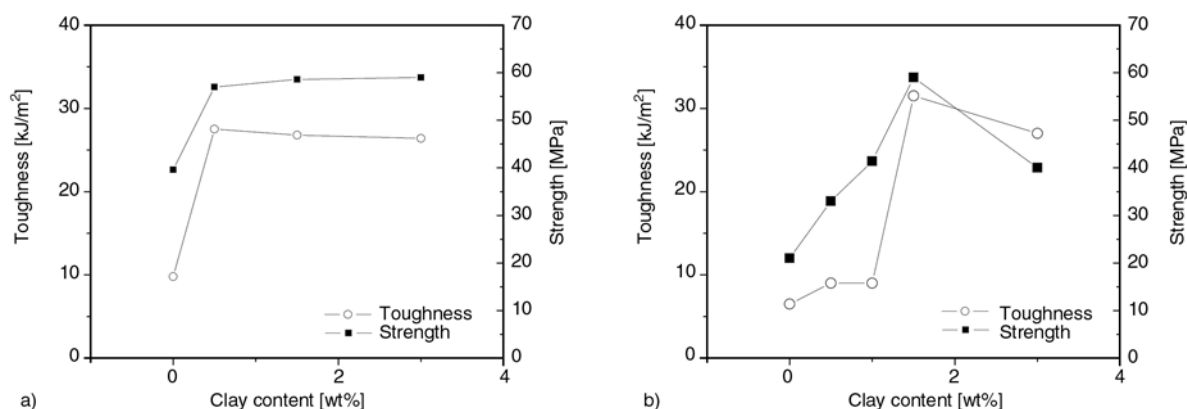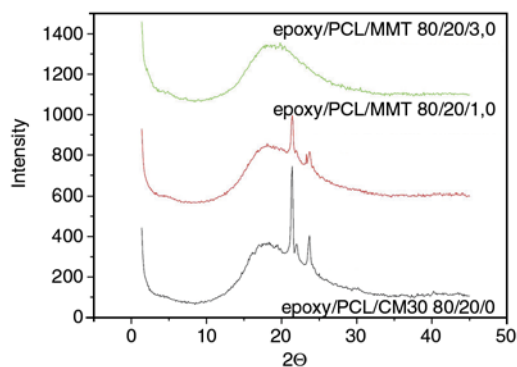
Figure 9. Effect of clay content on strength and toughness of epoxy containing (a) 15 wt% and (b) 20 wt% polycaprolactone

Evaluation of the mechanical parameters corresponding to the clay-induced morphological transitions in systems with supercritical PCL contents indicates the possibility that extremely variable properties could be achieved. In the case of low PCL contents, the relatively significant ability to affect the mechanical properties, including the achievement of a synergistic effect with minimal structural changes through a matrix-inclusion structure, indicate the dominant effect of varying the component parameter ratio.

Figure 7 shows that the matrix-inclusion structure (occurring at clay contents greater than 0.5 and 1.5% for 15 and 20% PCL, respectively (see Figures 3, 4), exhibits a higher modulus than the system with a co-continuous structure and the same composition. This effect occurs in parallel to the reinforcement of matrix by clay; moreover, this difference in the modulus occurs in spite of the significant change in the PCL crystallinity between the two structures. We have found (Figure 10 XRD) that an estimated modulus of 50 MPa corresponded to a crystallinity value less than 5% in the PCL inclusions, whereas the crystallinity of the continuous PCL phase was ~50%, corresponding to a modulus of 400 MPa. The drastic change in modulus exceeds the effect of the lower crystallinity. This increase corresponds to the well-known more significant impact [46] of continuous phases on the stiffness of a system, in comparison with that of the matrix-inclusions morphology, as documented by the obvious good correspondence of these experimental results with the approximate values predicted using models for the respective structures [46] (Figure 7) and the above-mentioned corresponding values of the PCL moduli combined with the experimental values of the modulus of the corresponding single epoxy nanocomposite.

In the case of the 70/30 composition, the structure appeared to be unfavorable in all cases (Figures 5a, 5b), and the high content of low-profile PCL corresponded to poor mechanical behavior, which was represented by strength values of ~20 MPa and toughness values of ~10 kJ·m^{-2}. These poor properties were further confirmed by low E (Figure 7). This significant detrimental effect was produced by the high content of PCL dissolved in the epoxy, which increased with the clay content, as indicated by the significantly reduced T_g (Table 1). The presence of interconnected epoxy globules (Figure 5c) inside the co-continuous PCL phase (i.e., the dual continuity of the epoxy phase) had practically no effect on the material properties.

4. Conclusions

The effect of organophilized montmorillonite (MMT) on the structure and properties of epoxy containing 5–30% PCL was significant, especially in the case of supercritical PCL concentration. The radical

Figure 10. XRD patterns of epoxy/PCL 80/20 w/w system with various clay contents

change in morphology observed for 15 and 20% PCL led to a substantial improvement of the mechanical behavior of the materials. The main reason for this improvement was a shift in the dynamic asymmetry caused by the localization of clay inside the epoxy phase, supporting its continuity. The mechanical behavior was further influenced by changes in the compositions of the coexisting phases because of the reduced degree of phase separation caused by the pinning effect of the clay, as indicated by the lowered T_g of the composites. This effect was more pronounced in the matrix-inclusion structure, for which a synergistic increase in the toughness occurred. The results indicate the potential of clay to tailor the structure and properties of RIPS systems with significant dynamic asymmetry. This fact is further supported by the improvement of mechanical properties, even for the use of PCL, which exhibits a relatively low level of mechanical performance.

Acknowledgements

References

[1] Francis B., Ramaswamy R., Rao V. L., Thomas S.: Toughening of diglycidyl ether of bisphenol-a epoxy resin using poly (ether ether ketone) with pendent ditert-butyl groups. International Journal of Polymeric Materials, **55**, 681–702 (2006).
DOI: 10.1080/00914030500323326

[2] Mimura K., Ito H., Fujioka H.: Improvement of thermal and mechanical properties by control of morphologies in PES-modified epoxy resins. Polymer, **41**, 4451–4459 (2000).
DOI: 10.1016/S0032-3861(99)00700-4

[3] Bucknall C. B., Gilbert A. H.: Toughening tetrafunctional epoxy resins using polyetherimide. Polymer, **30**, 213–217 (1989).
DOI: 10.1016/0032-3861(89)90107-9

[4] Hourston D. J., Lane J. M.: The toughening of epoxy resins with thermoplastics: 1. Trifunctional epoxy resin-polyetherimide blends. Polymer, **33**, 1379–1383 (1992).
DOI: 10.1016/0032-3861(92)90110-I

[5] Oyanguren P. A., Frontini P. M., Williams R. J. J., Vigier G., Pascault J. P.: Reaction-induced phase separation in poly(butylene terephthalate)-epoxy systems: 2. Morphologies generated and resulting properties. Polymer, **37**, 3087–3092 (1996).
DOI: 10.1016/0032-3861(96)89408-0

[6] Riew C. K., Kinloch A. J.: Toughened plastics II: Novel approaches in science and engineering. Advances in Chemistry Series 252, American Chemical Society, Washington (1996).

[7] Kelnar I., Khunová V., Kotek J., Kaprálková L.: Effect of clay treatment on structure and mechanical behavior of elastomer-containing polyamide 6 nanocomposite. Polymer, **48**, 5336–5339 (2007).
DOI: 10.1016/j.polymer.2007.06.062

[8] Kelnar I., Rotrekl J., Kotek, J., Kaprálková L.: Effect of montmorillonite modification on the behaviour of polyamide/polystyrene blends. Polymer International, **57**, 1281–1286 (2008).
DOI: 10.1002/pi.2475

[9] Alyamac E., Yilmazer U.: Reactive extrusion of poly (ethylene terephthalate)–(ethylene/methyl acrylate/glycidyl methacrylate)–organoclay nanocomposites. Polymer Composites, **28**, 251–258 (2007).
DOI: 10.1002/pc.20285

[10] Pascault J-P., Sautereau H., Williams R. J. J., Verdu J.: Thermosetting polymers. Marcel Dekker, New York (2002).
DOI: 10.1201/9780203908402

[11] Kelnar I., Rotrekl J., Kaprálková L., Hromádková J., Strachota A.: Effect of poly(oxyalkylene)amines on structure and properties of epoxide nanocomposites. Journal of Applied Polymer Science, **125**, 2755–2763 (2012).
DOI: 10.1002/app.36604

[12] Kelnar I., Rotrekl J., Kaprálková L., Hromádková J., Strachota A.: Effect of amine-terminated butadiene-acrylonitrile/clay combinations on the structure and properties of epoxy nanocomposites. Journal of Applied Polymer Science, **125**, 3477–3483 (2012).
DOI: 10.1002/app.36696

[13] Bakar M., Kostrzewa M., Hausnerova B., Sar K.: Preparation and property evaluation of nanocomposites based on polyurethane-modified epoxy/montmorillonite systems. Advances in Polymer Technology, **29**, 237–248 (2010).
DOI: 10.1002/adv.20192

[14] Peng M., Li H., Wu L., Chen Y., Zheng Q., Gu W.: Organically modified layered-silicates facilitate the formation of interconnected structure in the reaction-induced phase separation of epoxy/thermoplastic hybrid nanocomposite. Polymer, **46**, 7612–7623 (2005).
DOI: 10.1016/j.polymer.2005.06.013

[15] Zhang J., Xie X.: Influence of addition of silica particles on reaction-induced phase separation and properties of epoxy/PEI blends. Composites Part B: Engineering, **42**, 2163–2169 (2011).
DOI: 10.1016/j.compositesb.2011.05.013

[16] Peng M., Li D., Chen Y., Zheng Q.: Effect of an organoclay on the reaction-induced phase-separation kinetics and morphology of a poly(ether imide)/epoxy mixture. Journal of Applied Polymer Science, **104**, 1205–1214 (2007).
DOI: 10.1002/app.25759

[17] Mirmohseni A., Zavareh S.: Epoxy/acrylonitrile-butadiene-styrene copolymer/clay ternary nanocomposite as impact toughened epoxy. Journal of Polymer Research, **17**, 191–201 (2010).
DOI: 10.1007/s10965-009-9305-8

[18] Asif A., Leena K., Rao V. L., Ninan K. N.: Hydroxyl terminated poly(ether ether ketone) with pendant methyl group-toughened epoxy clay ternary nanocomposites: Preparation, morphology, and thermomechanical properties. Journal of Applied Polymer Science, **106**, 2936–2946 (2007).
DOI: 10.1002/app.26774

[19] Wu D., Lin D., Zhang J., Zhou W., Zhang M., Zhang Y., Wang D., Lin B.: Selective localization of nanofillers: Effect on morphology and crystallization of PLA/PCL blends. Macromolecular Chemistry and Physics, **212**, 613–626 (2011).
DOI: 10.1002/macp.201000579

[20] Asif A., John B., Rao V. L., Ninan K. N.: Surface morphology, thermomechanical and barrier properties of poly(ether sulfone)-toughened epoxy clay ternary nanocomposites. Polymer International, **59**, 986–997 (2010).
DOI: 10.1002/pi.2817

[21] Tanaka H., Lovinger A. J., Davis D. D.: Pattern evolution caused by dynamic coupling between wetting and phase separation in binary liquid mixture containing glass particles. Physical Review Letters, **72**, 2581–2584 (1994).
DOI: 10.1103/PhysRevLett.72.2581

[22] Ginzburg V. V., Qiu F., Paniconi M., Peng G., Jasnow D., Balazs A. C.: Simulation of hard particles in a phase-separating binary mixture. Physical Review Letters, **82**, 4026–4029 (1999).
DOI: 10.1103/PhysRevLett.82.4026

[23] Suppa D., Kuksenok O., Balazs A. C., Yeomans J. M.: Phase separation of a binary fluid in the presence of immobile particles: A lattice Boltzmann approach. Journal of Chemical Physics, **116**, 6305–6310 (2002).
DOI: 10.1063/1.1460863

[24] Nesterov A. E., Lipatov Y. S., Horichko V. S., Ignatova T. D.: Effect of filler on kinetics and energy of activation of phase separation in poly(methyl methacrylate)/poly(vinyl acetate) blend. Macromolecular Chemistry and Physics, **199**, 2609–2612 (1998).
DOI: 10.1002/(SICI)1521-3935(19981101)199:11<2609::AID-MACP2609>3.0.CO;2-Z

[25] Karim A., Douglas J. F., Nisato G., Liu D-W., Amis E. J.: Transient target patterns in phase separating filled polymer blends. Macromolecules, **32**, 5917–5924 (1999).
DOI: 10.1021/ma990439f

[26] Araki T., Tanaka H.: Dynamic depletion attraction between colloids suspended in a phase-separating binary liquid mixture. Journal of Physics: Condensed Matter, **20**, 072101/1–072101/6 (2008).
DOI: 10.1088/0953-8984/20/7/072101

[27] Yurekli K., Karim A., Amis E. J., Krishnamoorti R.: Influence of layered silicates on the phase-separated morphology of PS–PVME blends. Macromolecules, **36**, 7256–7267 (2003).
DOI: 10.1021/ma020755l

[28] Zhong X., Liu Y., Su H., Zhan G., Yu Y., Gan W.: Enhanced viscoelastic effect of mesoscopic fillers in phase separation. Soft Matter, **7**, 3642–3650 (2011).
DOI: 10.1039/c0sm01445a

[29] Gharachorlou A., Goharpey F.: Rheologically determined phase behavior of LCST blends in the presence of spherical nanoparticles. Macromolecules, **41**, 3276–3283 (2008).
DOI: 10.1021/ma7020985

[30] Bao S., Shen S., Liang G., Zhai H., Xu W., He P.: Curing behavior of epoxy resin/tung oil anhydride exfoliated nanocomposite by differential scanning calorimetry. Journal of Applied Polymer Science, **92**, 3822–3829 (2004).
DOI: 10.1002/app.20398

[31] Tanaka H.: Viscoelastic phase separation. Journal of Physics: Condensed Matter, 12, R207–R264 (2000).
DOI: 10.1088/0953-8984/12/15/201

[32] Cicala G., Mamo A., Recca G., Restuccia C. L.: Study on epoxy/thermoplastic blends based on the addition of a novel aromatic block copolymer. Polymer Engineering and Science, **47**, 2027–2033 (2007).
DOI: 10.1002/pen.20915

[33] Yeganeh J. K., Goharpey F., Foudazi R.: Rheology and morphology of dynamically asymmetric lcst blends: Polystyrene/poly(vinyl methyl ether). Macromolecules, **43**, 8670–8685 (2010).
DOI: 10.1021/ma101421s

[34] Xia T., Huang Y., Peng X., Li G.: Morphological transition induced by nanoparticles in dynamically asymmetric PS/PVME blends. Macromolecular Chemistry and Physics, **211**, 2240–2247 (2010).
DOI: 10.1002/macp.201000237

[35] Zhao L., Zhan G., Yu Y., Tang X., Li S.: Influence of attapulgites on cure-reaction-induced phase separation in epoxy/poly(ether sulfone) blends. Journal of Applied Polymer Science, **108**, 953–959 (2008).
DOI: 10.1002/app.27416

[36] Siddhamali S. K.: Toughening of epoxy/polycaprolactone composites via reaction induced phase separation. Polymer Composites, **21**, 846–855 (2000).
DOI: 10.1002/pc.10239

[37] Barone L., Carciotto S., Cicala G., Recca A.: Thermomechanical properties of epoxy/poly(ε-caprolactone) blends. Polymer Engineering and Science, **46**, 1576–1582 (2006).
DOI: 10.1002/pen.20447

[38] Bershtein V. A., Egorova L. M., Yakushev P. N., Pissis P., Sysel P., Brozova L.: Molecular dynamics in nanostructured polyimide–silica hybrid materials and their thermal stability. Journal of Polymer Science Part B: Polymer Physics, **40**, 1056–1069 (2002).
DOI: 10.1002/polb.10162

[39] Kourkoutsaki T., Logakis E., Kroutilova I., Matejka L., Nedbal J., Pissis P.: Polymer dynamics in rubbery epoxy networks/polyhedral oligomeric silsesquioxanes nanocomposites. Journal of Applied Polymer Science, **113**, 2569–2582 (2009).
DOI: 10.1002/app.30225

[40] Chen J-L., Chang F-C.: Temperature-dependent phase behavior in poly(ε-caprolactone)–epoxy blends. Polymer, **42**, 2193–2199 (2001).
DOI: 10.1016/S0032-3861(00)00511-5

[41] Vanden Poel G., Goossens S., Goderis B., Groeninckx G.: Reaction induced phase separation in semicrystalline thermoplastic/epoxy resin blends. Polymer, **46**, 10758–10771 (2005).
DOI: 10.1016/j.polymer.2005.09.013

[42] Chen J-L., Chang F-C.: Phase separation process in poly(ε-caprolactone)–epoxy blends. Macromolecules, **32**, 5348–5356 (1999).
DOI: 10.1021/ma981819o

[43] Zhang Y., Chen F., Shi W., Liang Y., Han C. C.: Layered structure formation in the reaction-induced phase separation of epoxy/polysulfone blends. Polymer, **51**, 6030–6036 (2010).
DOI: 10.1016/j.polymer.2010.10.027

[44] Kelnar I., Stephan M., Jakisch L., Fortelný I.: Reactive blending of Nylon 6 and modified poly(styrene-*co*-maleic anhydride); Influence of poly(styrene-*co*-maleic anhydride) modification by fatty amine onto blend properties. Journal of Applied Polymer Science, **66**, 555–562 (1997).
DOI: 10.1002/(SICI)1097-4628(19971017)66:3<555::AID-APP17>3.0.CO;2-U

[45] Yee A. F., Du J., Thouless M. D.: Toughening of epoxies. in 'Polymer blends: Performance' (eds.: Paul D. R., Bucknall C. B.) Wiley, New York, 225–267 (2000).

[46] Willemse R. C., Speijer A., Langeraar A. E., Posthuma de Boer A.: Tensile moduli of co-continuous polymer blends. Polymer, **40**, 6645–6650 (1999).
DOI: 10.1016/S0032-3861(98)00874-X

Estimating the creep strain to failure of PP at different load levels based on short term tests and Weibull characterization

L. M. Vas[*], P. Bakonyi*

Department of Polymer Engineering, Faculty of Mechanical Engineering, Budapest University of Technology and Economics, H-1111 Budapest, Műegyetem rkp. 3., Hungary

Abstract. The short and long term creep behavior is one of the most important properties of polymers used for engineering applications. In order to study this kind of behavior of PP tensile and short term creep measurements were performed and analyzed using long term creep behavior estimating method based on short term tensile and creep tests performed at room temperature, viscoelastic behavior, and variable transformations. Applying Weibull distribution based approximations for the measured curves predictions for the creep strain to failure depending on the creep load were determined and the parameters were found by fitting the measurements. The upper, mean, and lower estimations as well as the confidence interval for the means give a possibility for designers' calculations at arbitrary creep load levels.

Keywords: *material testing, short term creep, long term behavior, creep strain to failure, Weibull distribution*

1. Introduction

The long term creep behavior of polymers or polymer composites subjected to mechanical load is one of the most important properties considering the fact that all machine parts or other constructions should have a sufficient life span of some years therefore it has been studied for a long time in order to find suitable methods for estimating the expected lifetime at different load levels.

Supposing the polymeric material is of linear viscoelastic nature and/or exhibits simple thermo-rheological behavior the time-temperature superposition principle can be used to construct the long term creep curve called master-curve from short term creep measurements performed at different temperatures and a given load level [1–5]. In general the Williams-Landel-Ferry (WLF) or the Arrhenius equation or some combination of them is applied to determining the shift factor necessary for constructing the long term master curve [6–10]. Power law type approximations like Nutting's or Findley's ones [6, 8, 11] or simple rheological models such as Standard Solid or Burgers or their generalized forms [1–5, 12] can give a simple solution to extrapolate the measured data or to describe the master curve mathematically. In some cases constitutive mechanical models are developed using measured material constants and numerical analysis [13] or finite element models are created to describe thermoelastic creep [14]. In opposite to them models based on the kinetic, thermal activation, or micro-deformation behavior of molecule chains are developed to predict the creep of polymers [15–18].

In general these methods can be used just at or below a given load level and in most cases they can-not estimate the expected lifetime and/or the creep strain-to-failure.

---

[*]Corresponding author, e-mail: vas@pt.bme.hu

Nagy and Vas [19, 20] have developed a combined method for estimating the long term behavior from short term measurements based on the linear viscoelastic theory and non-linear variable transformations and they employed that to stress relaxation. In the present paper this method is applied to estimate the creep strain to failure of PP at arbitrary load levels by making use of the information provided by tensile tests and short term creep measurements performed at room temperature as well as a Weibull distribution based stochastic model.

2. Theoretical considerations

Considering mechanical tests a polymer specimen behaves as a system characterized by operator S that gives a relationship between the time-dependent stimulus as input, $X(t)$, and the response, $Y(t)$, as output (Equation (1)) [19, 20]:

$$Y(t) = S(X)(t) \qquad (1)$$

If X_1 and X_2 are two stimuli and X_2 is the integral of X_1, then the following relations are true (Equation (2)):

$$X_2(t) = I(X_1)(t) = \int_0^t X_1(u)\mathrm{d}u \leftrightarrow$$

$$\leftrightarrow X_1(t) = D(X_2)(t) = \frac{\mathrm{d}X_2(t)}{\mathrm{d}t} \qquad (2)$$

where I and D are integral and differential operators, respectively. Supposing the polymer material is of linear viscoelastic (LVE) behavior then operator S is linear therefore in most cases the relations according to Equation (2) are valid for the responses as well (Equation (3)):

$$Y_2(t) = S(X_2)(t) = S(I(X_1))(t) =$$

$$= I(S(X_1))(t) = I(Y_1)(t) \leftrightarrow$$

$$\leftrightarrow (Y_1)(t) = D(Y_2)(t) \qquad (3)$$

For example, if $X_1(t) = F_1(t) = F_0 I(t)$ is a step-function and $X_2(t) = F_2(t) = \dot{F}_0 t I(t)$ is a ramp-function where $I(t)$ is the unit jump function, F_0 is the creep load, and $\dot{F}_0$ is the load rate, hence the responses of the real material are the creep curve, $Y_1(t) = \varepsilon_1(t)$, and the tensile test curve, that is the tensile load strain-time relationship recorded, $Y_2(t) = \varepsilon_2(t)$. In case of LVE behavior the LVE estimation of the creep curve is the derivative of the tensile test one (Equation (4)) [19, 20]:

$$\varepsilon_{L1}(t) = D(\varepsilon_2)(t) = \frac{\mathrm{d}\varepsilon_2(t)}{\mathrm{d}t} \qquad (4)$$

The creep stimulus above, $F_1(t)$, is of ideal form because it has got a jump of infinite steepness. In the reality the slope should be finite therefore the real creep stimulus is given by Equation (5):

$$F_1(t) = \begin{cases} \dot{F}_0 t I(t), & t < t_0 \\ \dot{F}_0 t_0, & t \geq t_0 \end{cases} \qquad (5)$$

where t_o is the uploading time needed for setting the creep load level ($F_0 = \dot{F}_0 t_0$) (Figure 1a).
Nagy and Vas showed that in the case of real creep stimulus where the uploading, that is the setting the creep load, is performed with constant load rate and assuming LVE behavior the proper form of Equation (4) is as follows (Equation (6)) [19, 20]:

$$\varepsilon_{L1}(t) = \varepsilon_2(t) - \varepsilon_2(t - t_0), \, t_0 \leq t \leq t_{2B} \qquad (6)$$

where $\varepsilon_{L1}(t)$ is the LVE response to the stimulus (5) while $\varepsilon_2(t)$ is the tensile test curve, t_{2B} is the break-
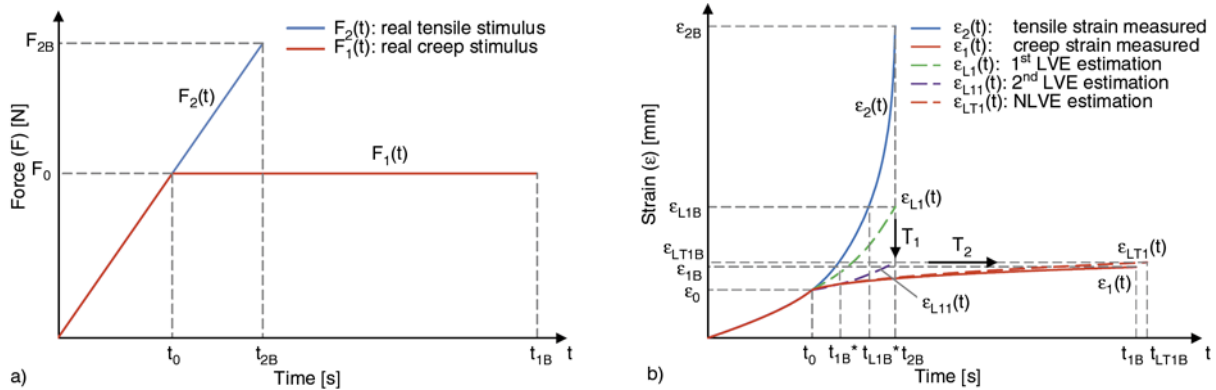
Figure 1. Stimuli of real creep and tensile tests (a) and the LVE estimation of the real creep curve (b)

ing time at tensile testing, consequently $\varepsilon_{2B} = \varepsilon_2(t_{2B})$ is the breaking strain, and $\varepsilon_2(t) = 0$ if $t \leq 0$. Equation (6) can be used if $\varepsilon_2(t)$ is the constant load rate tensile test response of the real polymer material and $\varepsilon_{L1}(t)$ can be considered as a linear viscoelastic (LVE) estimation of the real creep curve (Figure 1b). Real polymers exhibit LVE behavior only in a relatively small load range and beyond it they behave in a non-linear manner. It was also proven by Nagy and Vas [19, 20] that at a given creep load the real creep curve can be estimated by a non-linear variable transformation (T) of the LVE estimation that has got a kind of analogy with the load level – time superposition principle described by Urzumtsev and Maksimov [5] similar to that used in the case of the time-temperature superposition principle (Equation (7)):

$$\varepsilon_1(t) \approx T_1(\varepsilon_{L1}(T_2(t))) =: \varepsilon_{LT1}(t) \qquad (7)$$

where T_1 and T_2 are the component transformations of T (Figure 1b). T_2 is determined to be non-linear, however, T_1 can be realized in a linear form as follows (Equation (8)):

$$\varepsilon_{L11}(t) = T_1(\varepsilon_{L1}(t)) = \varepsilon_{L1}(t_0) + c(\varepsilon_{L1}(t) - \varepsilon_{L1}(t_0)) =$$
$$= \varepsilon_0 + c(\varepsilon_{L1}(t) - \varepsilon_0) \qquad (8)$$

where 'c' is a transformation constant and ε_0 is the creep strain load determined by the uploading time and defined by Equation (9):

$$\varepsilon_0 = \varepsilon_{L1}(t_0) = \varepsilon_2(t_0) \qquad (9)$$

Let t_{1B} be the real lifetime at creep hence the creep strain to failure is $\varepsilon_{1B} = \varepsilon_1(t_{1B})$ (Equation (10)) which can be estimated by Equation (8):

$$\varepsilon_{1B} \approx \varepsilon_{L11}(t_{2B}) = T_1(\varepsilon_{L1}(t_{2B})) =$$
$$= \varepsilon_0 + c(\varepsilon_{L1}(t_{2B}) - \varepsilon_0) \qquad (10)$$

It is obvious that the primary LVE estimation of the creep strain to failure is $\varepsilon_{L1}(t_{2B})$.

The steps of the whole calculation process can be summarized as follows (see Figure 1b).
1. Tensile test measurements ($\varepsilon_{2i}(t)$, $i = 1, \ldots, n$) →
2. Mean tensile test curve ($\varepsilon_2(t)$) averaging by point by point → 3. Primary LVE estimation of the creep process ($\varepsilon_{L1}(t)$) according to Equation (6) → 4. Secondary LVE estimation of the creep process ($\varepsilon_{L11}(t)$) by linear transformation T_1 according to Equations (7) and (8) using the mean values of the creep strain to failure measured at higher creep load levels which makes it possible to estimate the mean creep strain to failure → 5. NLVE estimation of the whole creep process by time transformation T_2 according to Equation (7) up to the creep failure using the short term creep measurements on the basis of which, in the knowledge of the mean creep strain to failure, the main creep time to failure can be estimated.

Steps 1.–3. are preparatory operations, in Step 4 we obtain estimation for the creep strain to failure while Step 5 provides the assessment of the measurable creep curve including the creep failure point with co-ordinates creep strain to failure estimated in Step 4 and creep lifetime as a new result.

In this paper the examinations are confined to steps 1–4 and it will be shown that in the case of PP tested Equations (8) and (10) can be used for estimating the creep strain to failure at arbitrary creep load level, as well as the right side of Equation (10) can be described by a stochastic model based on the Weibull distribution that will make it easier to determine the parameters of the tensile-testtime → creep-test-time transformation (T_2) in Step 5 planned to be carried out in a later paper.

3. Material and test methods

An isotactic polypropylene homopolymer (Tipplen H 949A from TVK, Tiszaújváros, Hungary) was applied to constant force rate tensile tests and creep measurements. The material was regranulated with Brabender Plastograph extruder machine to achieve a similar thermal prehistory as the glass fiber reinforced PP composites to be examined later [21].

148 mm long type 1A dumbbell specimens of 10 mm width and 4 mm thickness according to the ISO 527-2 Standard were injection molded on an Arburg Allrounder 320 C-GE 500-170 injection molding machine (Arburg, Germany).

For the tests a Zwick Z-005 universal testing machine (with 5 kN nominal capacity standard load cell) was used in constant force rate mode, where the constant force rate was 50 N/s until the specimen broke in tensile tests or the preset load level was reached in creep tests. The gauge length was 100 mm

long hence the elongation in millimeter equals the strain in percent numerically. In the creep tests after the uploading the load was held constant for 10 hours (or until the specimen failed) and the length variation of the specimen was measured using the crosshead signal. The applied load levels were determined in 10 percent steps of the measured average breaking force. Each test was carried out under uniaxial tensile load and at room temperature (23±1°C).

4. Measurements

Thirty constant force rate tensile tests were performed on injection molded dumbbell specimens. At the starting phase of uploading due to the inertia of the engine system of the universal testing machine and the time-delay of the data collection a zero-point error can be observed which could cause serious difficulties in calculating the correct mean curves. In order to obtain correct averaged characteristics the curves were shifted one by one as a function of time till the initial tangents of the measured strain-time and force-time curves crossed

exactly the origin (Figure 2a). After shifting the curves several starting points were corrected to fit into the initial tangent (Figure 2b).

The corrected results of the tensile measurements were averaged. The averaged tensile curve showed indeterminate strain values not fitted to the mean of the others in the breaking section (Figure 3a). This had to be corrected and smoothed by shifting the end section of the strain-time curve so they could be used for later calculations (Figure 3b). According to the 30 tensile measurements the average breaking strain was 10.69% with a standard deviation of 0.728% and the average breaking force of the measurements was 1610±19.6 N.

On the other hand five creep measurements were performed at every load level that were 10, 20, 30, 40, 50, 60, 65, 70, 75, 80, 85, 90 and 95% of the mean breaking force taken at 1600 N.

Each of the altogether 65 creep tests lasted 10 hours long or till the specimen was failed. The curves were averaged point by point in the way described above and if it was necessary (where the specimen was broken within the creep measurement) smoothed.
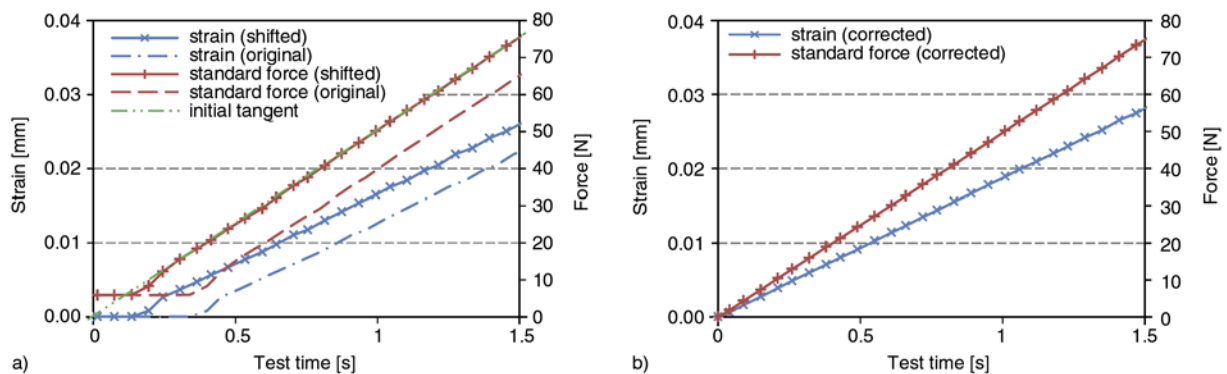
Figure 2. Shifting the tensile curves to the origin using an initial tangent (a) and tensile curves with corrected starting points (b)
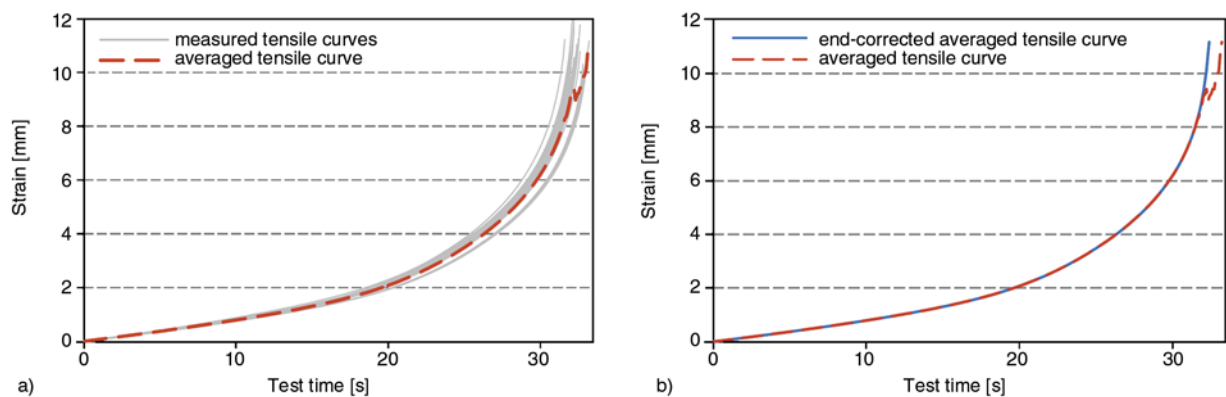
Figure 3. Averaging the tensile curve bundle (a) and smoothing the indeterminate strain values at the breaking range of shifted curves (b)
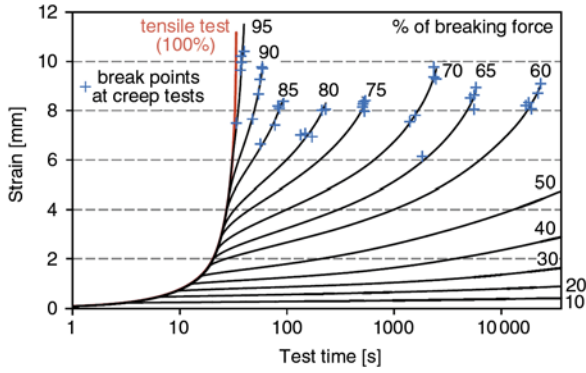
Figure 4. Creep results carried out at different tensile load levels

The averaged and smoothed creep curves can be seen in Figure 4 where all the creep failure points observed are depicted as well.

5. Evaluation and discussion
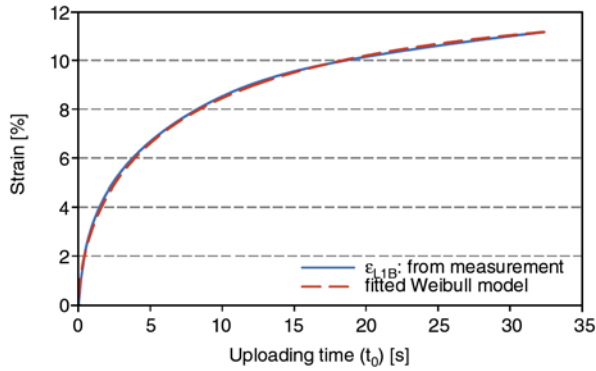### 5.1. Estimation of LVE creep strain to failure based on Weibull distribution

It is obvious that the values of the LVE creep strain to failure, $\varepsilon_{L1B}(t_0)$, determined from the real tensile test curve, $\varepsilon_2(t)$, are dependent on creep load level, F_0, or the uploading time, t_0, that is proportional to F_0, and create a monotonically increasing and convergent sequence with increasing t_0 or F_0 like the measured ones according to Ehrenstein (Figure 88 in page 115 of [2]) therefore there exists a finite value ($0 < \varepsilon_{L1B\infty} < \infty$) as least upper bound. The creep strain to failure values normalized by this upper bound ($\varepsilon_{L1B\infty}$) fall in interval [0,1] and take up value 1 at a certain loading time ($0 \leq t_{0\infty} \leq \infty$). All this means that these normalized failure strain values meet the formal requirements of a probability distribution function. On the other hand, this function can be understood as a distribution characteristic of a strength variable, σ_{B0}, because the values of the independent variable are time values proportional to the load and the dependent variable is a ratio connected to failure events that expresses how close the failure is to the stress $\sigma_{2B} = F_{2B}/A_0$ representing the sure and sudden breakage or fracture (A_0 is the cross section of the specimens before loading and here $A_0 = 40$ mm²). This strength variable, σ_{B0}, is in relation to the real creep strain to failure (ε_{1B}) that can be detailed in the following way. Using the measured creep curve, $\varepsilon_1(t)$, the creep strain to failure, ε_{1B}, belongs to the creep failure time (t_{1B}), that

is the creep lifetime, t_{1B}: $\varepsilon_{1B} = \varepsilon_1(t_{1B})$. The first LVE estimation of ε_{1B} is $\varepsilon_{L1B} = \varepsilon_{L1}(t_{2B})$ (Figure 1b). Considering the intersection point of the tensile test curve, $\varepsilon_2(t)$, and the creep strain to failure level (ε_{1B}) (see Figure 1b), let its projection onto the tensile time axis be denoted by $t^*_{1B} = \varepsilon_2^{-1}(\varepsilon_{1B}) = \varepsilon_2^{-1}(\varepsilon_1(t_{1B}))$ and a first LVE estimation of which can be $t^*_{L1B} = \varepsilon_2^{-1}(\varepsilon_{L1B})$. Because constant load rate tensile test was used ($\dot{F}_0 = 50$ N/s) the stress corresponding to t^*_{L1B} is $\sigma^*_{L1B} = \dot{\sigma}_0 t^*_{L1B}$ where $\dot{\sigma}_0 = \dot{F}_0/A_0$. The distribution function of σ^*_{L1B} is equal to those of σ_{B0} and a kind of transformed creep lifetime variable, $\tau = \sigma_{B0}/\dot{\sigma}_0$, is in strict relation with that of the first LVE estimation of the creep strain to failure (ε_{L1B}). Taking into account that the statistical properties related to failure such as stress-, strain-, and time-to-failure have got a kind of minimum nature therefore they can be described with the Weibull distribution that is the extreme value distribution of minima [22] under sufficiently general conditions in both practice and theory [23] shown by e.g. Phoenix [24, 25], Wagner *et al.* [16], or later Raghavan and Meshii [17], Vujosevic and Krajcinovic [18], or recently Fancey [26]. Hence it can be applied to the distribution of both the strength, σ_{B0}, and the transformed lifetime, τ, as well (Equation (11)). All that can be followed well in Equation (11):

$$P\left(\sigma^*_{L1B} = \dot{\sigma}_0 t^*_{L1B} < \sigma_2 = \dot{\sigma}_0 t_2 = \dot{\sigma}_0 \frac{t_2}{t_0} t_0\right) =$$

$$= P(\sigma_{B0} = \alpha_{20}\sigma^*_{L1B} < \sigma_0 = \dot{\sigma}_0 t_0) =$$

$$= P\left(\tau = \frac{\sigma_{B0}}{\dot{\sigma}_0} = \alpha_{20}t^*_{L1B} = \alpha_{20}\varepsilon_2^{-1}(\varepsilon_{L1B}) < t_0\right) =$$

$$= P\left(\varepsilon_{L1B} = \varepsilon_2\left(\frac{\tau}{\alpha_{20}}\right) < \varepsilon_2\left(\frac{t_0}{\alpha_{20}}\right)\right) =$$

$$= 1 - e^{-\left(\frac{t_0}{a}\right)^k} = \frac{\varepsilon_{L1B}(t_0)}{\varepsilon_{L1B\infty}} \quad (11)$$

where where σ_2 and t_2 are respectively tensile load and tensile time values while $0 < \alpha_{20} = t_0/t_2 < 1$ is a kind of shift factor [4, 5], and $\tau = \alpha_{20}t^*_{L1B} \approx \alpha_{20}t^*_{1B} = \alpha_{20}\varepsilon_2^{-1}(\varepsilon_1(t_{1B}))$ is the first LVE estimation of a sort of creep lifetime transformed to the tensile time range but it is not the creep time failure, as well as 'a' and 'k' are the Weibull scale and modulus parameters, respectively.

Figure 5. LVE estimation of the creep strain to failure calculated from the tensile test measurements and the Weibull distribution based model fitted

Rearranging Equation (11) yields the relationship between the mean LVE creep strain to failure and uploading time (Equation (12)):

$$\varepsilon_{L1B}(t_0) = \varepsilon_{L1B\infty}\left(1 - e^{-\left(\frac{t_0}{a}\right)^k}\right), 0 \le t_0 \le t_{2B} \quad (12)$$

If $t_0 = 0$ then $\varepsilon_{L1B}(0) = 0$, and $t_0 = t_{2B}$ leads to $\varepsilon_{L1B}(t_{2B}) = \varepsilon_{2B}$. According to the measurements the mean values of the latter determined by the endpoint of the averaged tensile test curve are $t_{2B} = 32.37$ s and $\varepsilon_{2B} = 11.17\%$.

Equation (6) at $t = t_{2B}$ gives a possibility to determine $\varepsilon_{L1B}(t_0)$ from the measured tensile test curve, $\varepsilon_2(t)$, because $\varepsilon_{L1B}(t_0) = \varepsilon_{L1}(t_{2B})$ (Figure 5).

Figure 5 shows the LVE estimation of the creep strain to failure as a function of the uploading time determined from the measured tensile test curve and its Weibull distribution based approximation fitted by using Equation (12).

The goodness of this fitting is characterized by the high determination coefficient ($R^2 = 0.995$) (mean squared error in strain is 0.075%) where the parameters a, k, and $\varepsilon_{L1B\infty}$ came about 8.076 s, 0.5875, and 12.47% respectively.

5.2. Weibull distribution based approximation of the tensile test curve

Rearranging Equation (6) gives a recursive formula (Equation (13)) for the tensile test curve:

$$\varepsilon_2(t) = \varepsilon_{L1}(t) + \varepsilon_2(t - t_0), t_0 \le t \le t_{2B} \quad (13)$$

This is also true for $t = t_{2B}$ and since $\varepsilon_2(t_{2B}) = \varepsilon_{2B}$ and $\varepsilon_{L1B}(t_0) = \varepsilon_{L1}(t_{2B})$ hence from Equation (13) we get Equation (14):
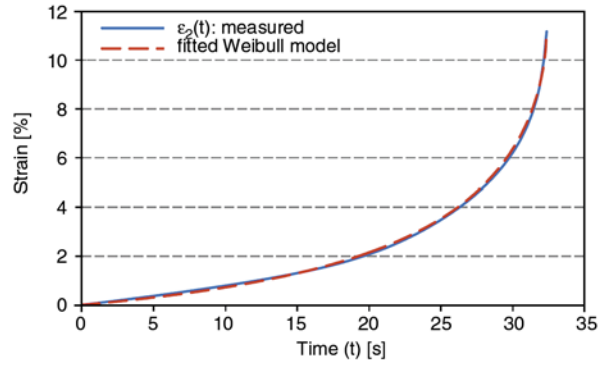
Figure 6. Averaged tensile test curve and its Weibull distribution based approximation

$$\varepsilon_2(t_{2B} - t_0) = \varepsilon_{2B} - \varepsilon_{L1B}(t_0) \quad (14)$$

where the domain of the function on the left side is $[0, t_{2B}]$ therefore its independent variable can be substituted by $t_0 = t_{2B} - t$, $0 \le t \le t_{2B}$ (Equation (15)):

$$\varepsilon_2(t) = \varepsilon_{2B} - \varepsilon_{L1B}(t_{2B} - t) \quad (15)$$

Taking Equation (12) at $t_0 = t_{2B} - t$ and substituting it into Equation (15) provides a Weibull distribution based formula by Equation (16) for approximating the mean tensile test curve as an LVE model (Figure 6; mean squared error of the approximation measured in strain is 0.075%).

$$\varepsilon_2(t) \approx \varepsilon_{L2}(t) = \varepsilon_{2B} - \varepsilon_{L1B\infty}\left(1 - e^{-\left(\frac{t_{2B} - t}{a}\right)^k}\right),$$
$$0 \le t \le t_{2B} \quad (16)$$

Equation (16) gives the breaking strain, ε_{2B}, at setting $t = t_{2B}$ and 0 at $t = 0$.

## 5.3. Relation between creep strain to failure increment and load level

Subtracting the strain loads, ε_0, from values $\varepsilon_{L1B}(t_0)$ and plotting them as a function of the uploading time, t_0, results in a nearly symmetric curve having a maximum that can be described by using the Weibull-distribution based method as well (Equation (17)) (Figure 7).

$$\varepsilon_{L1B}(t_0) - \varepsilon_0 = \varepsilon_{L1B}(t_0) - \varepsilon_2(t_0) =$$

$$= \varepsilon_{L1B\infty}\left(1 - e^{-\left(\frac{t_0}{a}\right)^k} + e^{-\left(\frac{t_{2B}}{a}\right)^k} - e^{-\left(\frac{t_{2B} - t_0}{a}\right)^k}\right),$$
$$0 \le t_0 \le t_{2B} \quad (17)$$
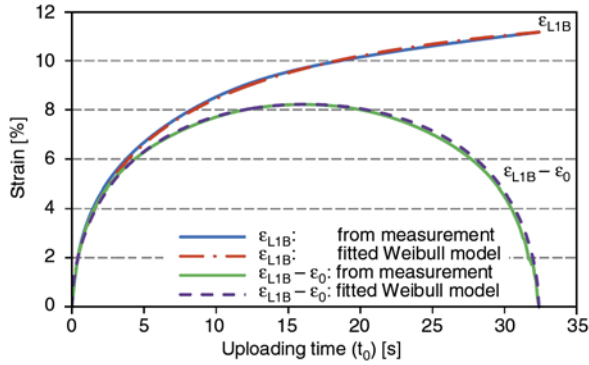
Figure 7. LVE estimation of the creep strain to failure and its increment versus the uploading time (t_0) calculated from tensile measurements and their Weibull distribution based approximation
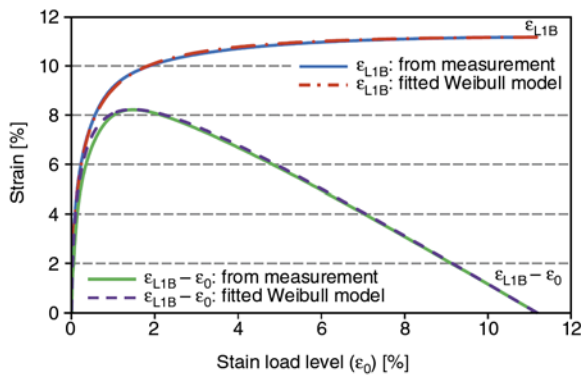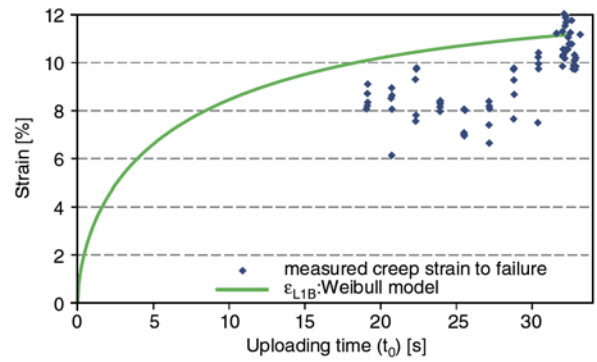

Figure 8. LVE estimation of the creep strain to failure and its increment versus the creep strain load (ε_0) calculated from tensile measurements and their Weibull distribution based approximation

Depicting the curves in Figure 7 as a function of the creep strain load, ε_0, makes the originally nearly symmetric one strongly asymmetric (Figure 8).

The creep strain to failure increment has got a maximum in both cases ($\varepsilon_{L1B} - \varepsilon_0 = 8.23\%$ at $t_0 = 16.2$ s or $\varepsilon_0 = 1.47\%$). The strain value and its place may be characteristic for the material tested therefore it is worth studying the possible changes in structure related to it. The mean squared error of the approximation measured in strain is 0.13%.

5.4. Estimation of the measured creep strain to failure

Using Equation (6) and the tensile test curve modeled with Equation (16) the LVE estimation of the creep curve can be obtained ($t_0 \leq t \leq t_{2B}$) (Equation (18)):

Figure 9. Weibull distribution based LVE estimation and the measured values of the creep strain to failure versus the uploading time

$$\varepsilon_{L1}(t) = \varepsilon_{L2}(t) - \varepsilon_{L2}(t - t_0) =$$

$$= \varepsilon_{L1B\infty}\left(e^{-\left(\frac{t_{2B} - t}{a}\right)^k} - e^{-\left(\frac{t_{2B} - t + t_0}{a}\right)^k}\right),$$

$$t_0 \leq t \leq t_{2B} \qquad (18)$$

If t_{2B} is the mean value of the fracture times obtained by tensile measurements then $\varepsilon_{L1B}(t_0) = \varepsilon_{L1}(t_{2B})$ is the LVE estimation of the real creep strain to failure, $\varepsilon_{1B}(t_0)$, belonging to uploading time t_0. On the basis of the creep measurements done at higher strain load levels these $\varepsilon_{L1B}(t_0)$ values can be considered as an upper estimation of the measured ones (Equation (19)) (Figure 9):

$$\varepsilon_{1B}(t_0) \leq \varepsilon_{L1B}(t_0) = \varepsilon_{L1}(t_{2B}), 0 \leq t_0 \leq t_{2B} \qquad (19)$$

Applying variable transformation T_1 along the strain axis to Equation (18) provides the first nonlinear viscoelastic approximation (NLVE) of the real creep curve ($\varepsilon_{L11}(t)$). Numerical examinations showed that in this case transformation T_1 could be realized as a linear combination using a permanent transformation parameter, $0 < c$, as follows (Equation (20)):

$$\varepsilon_{L11}(t) = \varepsilon_{L1}(t_0) + c(\varepsilon_{L1}(t) - \varepsilon_{L1}(t_0)) =$$

$$= (1-c)\varepsilon_0 + c\varepsilon_{L1B\infty}\left(e^{-\left(\frac{t_{2B}-t}{a}\right)^k} - e^{-\left(\frac{t_{2B}-t+t_0}{a}\right)^k}\right)$$

$$(20)$$

The value of this new approximation of the creep curve set at t_{2B} estimates the real creep strain to fail-
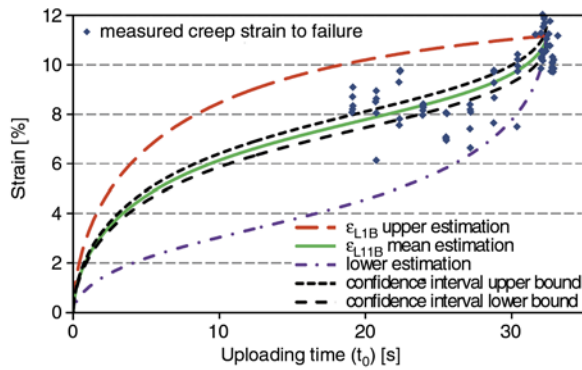
Figure 10. Measured values of the creep strain to failure versus the uploading time and their upper, mean, and lower estimations as well as confidence interval curves for the expected values

ure, $\varepsilon_{1B} = \varepsilon_1(t_{1B})$, observed at instant t_{1B} of the creep failure in a sense of average (Equation (21)):

$$\varepsilon_{1B}(t_0) \approx \varepsilon_{L1B}(t_0) = \varepsilon_{L1}(t_{2B}) =$$

$$= (1 - c)\varepsilon_0 + c\varepsilon_{L1B\infty}\left(1 - e^{-\left(\frac{t_0}{a}\right)^k}\right) \qquad (21)$$

Fitting the measured values of the creep strain to failure by using the least square method in order to estimate the mean values the transformation parameter, c, came about 0.7 (Figure 10) (mean squared error in strain was 0.91% indicating a rather large standard deviation).

According to numerical analysis the measured creep strain to failure can be estimated by the LVE approximation from above and its transformed forms calculated with $c = 0.7$ and 0.3 give estimations for the mean and lower values respectively (Figure 10). Besides the mean values the upper and lower estimations for single values provide a range useful for designers' calculations at arbitrary creep load levels by assessing the probability levels belonging to them. Similarly confidence interval can be constructed for the expected strain to failure values. Let ε_{2B} and $s_{\varepsilon 2B}$ be the mean value and the standard deviation of the breaking strain measured by constant load rate tensile tests and calculated from 'n' measurements. The confidence interval with significance level, $0 < \alpha < 1$, is given for the mean value by Equation (22):

$$\left(\varepsilon_{2B} - t_{\alpha/2,f}\frac{s_{\varepsilon 2B}}{\sqrt{n}}; \ \varepsilon_{2B} + t_{1-\alpha/2,f}\frac{s_{\varepsilon 2B}}{\sqrt{n}}\right) =$$

$$= \left(\varepsilon_{2B}\left[1 - t_{\alpha/2,f}\frac{V_{\varepsilon 2B}}{\sqrt{n}}\right]; \ \varepsilon_{2B}\left[1 + t_{\alpha/2,f}\frac{V_{\varepsilon 2B}}{\sqrt{n}}\right]\right) =$$

$$= (\varepsilon_{2B}[1 - \delta_n]; \ \varepsilon_{2B}[1 + \delta_n]); \ \delta_n = t_{\alpha/2,f}\frac{s_{\varepsilon 2B}}{\sqrt{n}} \quad (22)$$

where $f = n - 1$ is the degree of freedom and $t_{\alpha/2,f}$ is the two sided confidence coefficient taken from the Student table while $V_{\varepsilon 2B} = s_{\varepsilon 2B}/\varepsilon_{2B}$ is the relative standard deviation [27]. This can be extended for the mean creep strain to failure values using the method leading from Equation (12) to Equation (21). For simplicity assume that $V_{\varepsilon 2B}$ is constant a confidence interval range created by upper (U) and lower (L) borderlines can be estimated for the expected creep strain to failure values at arbitrary creep load levels by multiplying Equation (12) by $(1 \pm \delta_n)$ and transforming that according to Equation (21).

$$\varepsilon_{1B}^{U,L}(t_0) \approx \varepsilon_{L1B}^{U,L}(t_0) =$$

$$= (1 - c)\varepsilon_0 + c\varepsilon_{L1B\infty}(1 \pm \delta_n)\left(1 - e^{-\left(\frac{t_0}{a}\right)^k}\right) (23)$$

The lower limit of this confidence interval that is the curve $\varepsilon_{L1B}^{L}(t_0)$ ($n = 30$, $V_{\varepsilon 2B} = 0.068$, $\alpha = 0.001$, $t = 3.659$ [27], and $\delta_n = 0.0455$ in Figure 10) gives a possibility to determine a safety factor based on the expected value. The accuracy can be improved by assessing the relationship between $V_{\varepsilon 2B}$ and t_0 which can be performed in the knowledge of Equation (12).

Figures 11 and 12 show the curves calculated on the basis of those in Figure 10 and the measured creep strain increment values versus the uploading time and the strain load level.

It can be stated that the range bounded by the upper and lower estimations in Figure 10 is also effective in the case of the creep strain to failure increments considering it as a function of the uploading time (Figure 11) or the strain load level (Figure 12).

Figures 11 and 12 confirm the result of analysis that there might exist a maximum for the creep strain to failure increment values when plotting them as a
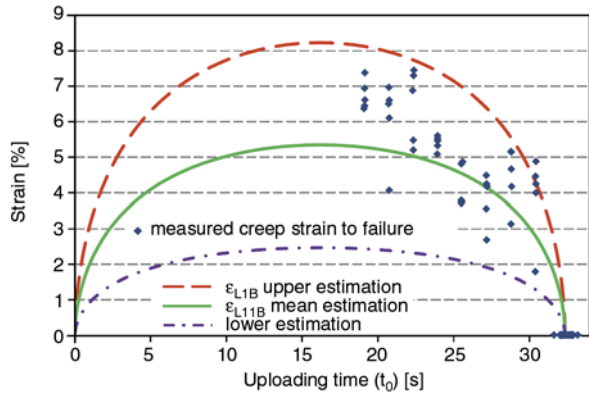
Figure 11. Measured values of the creep strain to failure increments versus the uploading time and their upper, mean, and lower estimations
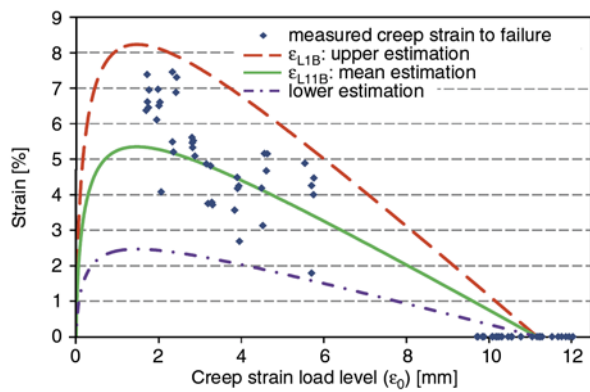
Figure 12. Measured values of the creep strain to failure increments versus the strain load level and their upper, mean, and lower estimations

function of the uploading time or the creep strain load level.

6. Conclusions

In order to study the creep behavior tensile tests and short term creep tests were carried out on injection molded PP specimens at room temperature. After correcting the zero-point error of the tensile measurements the recorded strain-time curves were averaged point- by point. Using an LVE formula developed earlier the LVE creep strain to failure values were estimated from the mean tensile test curve. A Weibull distribution based stochastic model was used to describe the variation of the mean values of these strain to failure estimations where the parameters were found by fitting the measurements. This made it possible to derive an approximating function for the mean tensile test curve as well. By linear variable transformation of the LVE strain characteristics upper, mean, and lower estimations as

well as confidence interval curves for the expected values were determined for the measured creep strain to failure values which give a possibility for designers' calculations at arbitrary creep load levels.

According to the result of analysis the creep strain to failure increment values might have a maximum in the function of the uploading time or the creep strain load level.

The Weibull distribution based mathematical approximation applied gives a hand for developing the non-linear time-transformation for the estimation of the long term creep behavior and the expected lifetime in a next step and a good basis for estimating additional statistical characteristics such as standard deviations and confidence intervals.

References

[1] Ward I. M., Hadley D. W.: Mechanical properties of solid polymers. Wiley, Chichester (1995).
[2] Ehrenstein G. W.: Polymerwerkstoffe – Struktur und mechanisches Verhalten. Hanser, München (1978).
[3] Nielsen L. E., Landel R. F.: Mechanical properties of polymers and composites. Marcel Dekker, New York (1994).
[4] Retting W.: Mechanik der Kunststoffe. Hanser, München (1992).
[5] Urzumtsev J. S., Maksimov R. D.: Deformation of plastics (in Russian). Zinatne, Riga (1975).
[6] Dutta P. K., Hui D.: Creep rupture of a GFRP composite at elevated temperatures. Computers and Structures, **76**, 153–161 (2000).
DOI: 10.1016/S0045-7949(99)00176-5
[7] Guo Y-C., Xin C-L., Song M-S., He Y-D.: Study on short- and long-term creep behavior of plastics geogrid. Polymer Testing, **24**, 793–798 (2005).
DOI: 10.1016/j.polymertesting.2005.02.014

[8] Siengchin S., Karger-Kocsis J.: Structure and creep response of toughened and nanoreinforced polyamides produced via the latex route: Effect of nanofiller type. Composites Science and Technology, **69**, 677–683 (2009).
DOI: 10.1016/j.compscitech.2009.01.003

[9] Izer A., Bárány T.: Effect of consolidation on the flexural creep behaviour of all-polypropylene composite. Express Polymer Letters, **4**, 210–216 (2010).
DOI: 10.3144/expresspolymlett.2010.27

[10] Pandini S., Pegoretti A.: Time and temperature effects on Poisson's ratio of poly(butylene terephthalate). Express Polymer Letters, **5**, 685–697 (2011).
DOI: 10.3144/expresspolymlett.2011.67

[11] Rees D. W. A.: Nutting creep in polymer composites. Journal of Materials Processing Technology, **143**, 164–170 (2003).
DOI: 10.1016/S0924-0136(03)00399-6

[12] Banik K.: Effect of mold temperature on short and long-term mechanical properties of PBT. Express Polymer Letters, **2**, 111–117 (2008).
DOI: 10.3144/expresspolymlett.2008.15

[13] Drozdov A. D.: Creep rupture and viscoelastoplasticity of polypropylene. Engineering Fracture Mechanics, **77**, 2277–2293 (2010).
DOI: 10.1016/j.engfracmech.2010.05.010

[14] Chung P. W., Tamma K. K., Namburu R. R.: A finite element thermo-viscoelastic creep approach for heterogeneous structures with dissipative correctors. Finite Elements in Analysis and Design, **36**, 279–313 (2000).
DOI: 10.1016/S0168-874X(00)00037-8

[15] Baltussen J. J. M., Northolt M. G.: The viscoelastic extension of polymer fibres: Creep behaviour. Polymer, **42**, 3835–3846 (2001).
DOI: 10.1016/S0032-3861(00)00604-2

[16] Wagner H. D., Schwartz P., Phoenix S. L.: Lifetime statistics for single kevlar 49 filaments in creep-rupture. Journal of Materials Science, **21**, 1868–1878 (1986).
DOI: 10.1007/BF00547921

[17] Raghavan J., Meshii M.: Creep of polymer composites. Composites Science and Technology, **57**, 1673–1688 (1997).
DOI: 10.1016/S0266-3538(97)00104-8

[18] Vujosevic M., Krajcinovic D.: Creep rupture of polymers – A statistical model. International Journal of Solids and Structures, **34**, 1105–1122 (1997)
DOI: 10.1016/S0020-7683(96)00067-4

[19] Vas L. M., Nagy P.: Investigating the time dependent behavior of thermoplastic polymers under tensile load. Macromolecular Symposia, **239**, 176–181 (2006).
DOI: 10.1002/masy.200690094

[20] Nagy P., Vas L. M.: Relationship between constant strain rate and stress relaxation behavior of polypropylene. Express Polymer Letters, **1**, 84–91 (2007).
DOI: 10.3144/expresspolymlett.2007.15

[21] Bakonyi P., Vas L. M., Nagy P.: Comparison of long term creep behaviour of PP and its glass fibre reinforced composite. in 'Proceedings of the 14th European Conference on Composite Materials, Budapest, Hungary', Paper ID-325 p9 (2010).

[22] Bolotin V. V.: Statistical methods in structural mechanics. Holden-Day, San Francisco (1969).

[23] Sutherland L. S., Guedes Soares C.: Review of probabilistic models of the strength of composite materials. Reliability Engineering and System Safety, **56**, 183–196 (1997).
DOI: 10.1016/S0951-8320(97)00027-6

[24] Phoenix S. L.: Stochastic models for the tensile strength, fatigue stress-rupture of fiber bundles. Advances in Engineering Science, **1**, 167–181 (1976).

[25] Phoenix S. L.: Statistical aspects of failure of fibrous materials. in 'The Fifth Conference on Composite Materials: Testing and Design, New Orleans, USA' 455–483 (1979).

[26] Fancey K. S.: A mechanical model for creep, recovery and stress relaxation in polymeric materials. Journal of Materials Science, **40**, 4827–4831 (2005).
DOI: 10.1007/s10853-005-2020-x

[27] Himmelblau D. M.: Process analysis by statistical methods. Wiley, New York (1970).

Phenyl hepta cyclopentyl – polyhedral oligomeric silsesquioxane (ph,hcp-POSS)/Polystyrene (PS) nanocomposites: the influence of substituents in the phenyl group on the thermal stability

I. Blanco[1,], L. Abate[1], M. L. Antonelli[2], F. A. Bottino[1], P. Bottino[3]*

[1]Department of Industrial Engineering, University of Catania, V.le A. Doria 6, 95125 Catania, Italy
[2]Department of Chemistry, University 'Sapienza' of Rome, P.le A. Moro 5, 00185 Roma, Italy
[3]Department of Pharmaceutical Sciences, University of Catania, V.le A. Doria 6, 95125 Catania, Italy

Abstract. Some new Polystyrene (PS) nanocomposites were prepared by using two Polyhedral Oligomeric Silsesquioxanes (POSSs), namely $RR'_7(SiO_{1.5})_8$ (where R = 4-methoxyphenyl or 2,4-difluorophenyl and R' = cyclopentyl), as fillers, and their degradation was studied to investigate the effect of the electron-donor or electron-withdrawing character of the phenyl group substituents on thermal stability. Nanocomposites were synthesized by *in situ* polymerization of styrene in the presence of various concentrations of POSS. Proton nuclear magnetic resonance (^{1}H NMR) spectra indicated that the POSS content in the obtained nanocomposites was higher than that in reactant mixtures. Inherent viscosity (η_{inh}) and glass transition temperature (T_g) determinations indicated that the average molar mass of polymer in 4-methoxynanocomposites was the same than neat PS, while it was much lower in 2,4-difluoro derivatives. Degradations were carried out in both flowing nitrogen and static air atmospheres, in the scanning mode, at various heating rates, and temperature at 5% mass loss ($T_{5\%}$) and the activation energy (E_a) of degradation of various nanocomposites were determined. The values obtained for 4-methoxyderivatives were higher than unfilled PS thus indicating higher thermal stability. Conversely, the values found for 2,4-difluoro derivatives were lower, in some cases even than those of neat PS. The results were discussed and interpreted.

Keywords: nanocomposites, thermal properties, polystyrene, POSS

1. Introduction

Even though polymers are compounds largely used in many fields owing to the various and excellent chemical properties, the improvement of their physical and mechanical properties is often requested, thus driving researchers towards the synthesis of composite materials, it means of hybrid materials obtained by coupling organic polymers with inorganic fillers [1]. Silica and layered silicates were first used to this purpose [2], so giving rise to composites showing better mechanical and thermal properties than those of conventional polymers [3–7].

Also, the dispersion at nanoscale level of filler in polymeric matrix generally improves physical, mechanical, barrier and flammability properties in comparison with virgin polymer [8–20]. In addition, it leads to a pronounced increase of thermal stability [20–22], it being important feature because nanocomposites so obtained can be subjected to high temperatures during processing and/or in service.

In the last years a new class of inorganic–organic nanoparticles, namely Polyhedral Oligomeric Silsesquioxanes (POSSs), has awaken increasing interest for the use as filler of polymer based nano-

---

composites [23–29]. The general formula of POSSs is $(RSiO_{1.5})_n$, or R_nT_n, where organic substituents (R = alkyl, aryl or any other) are attached to silicon cage.

We have in progress a wide research, concerning the synthesis and the characterization of new thermally stable nanocomposites of polystyrene (PS) and polyolefins having POSSs as fillers. Some $RR'_7(SiO_{1.5})_8$ POSSs (where R' = cyclopentyl or isobutyl and $R = C_6H_5$- or one of its mono-, di- or tri-substituted derivatives) were previously synthesized and characterized [30, 31], owing to their good compatibility and solubility in polymer matrices due to the presence of aliphatic and cyclo-aliphatic groups linked to silicon cage [32–35].

The results obtained indicated better thermal properties for heptacyclopentyl-POSSs in comparison with the corresponding heptaisobutyl- derivatives, and, in particular, phenyl, heptacyclopentyl-POSS (ph,hcp-POSS) appeared the most thermally stable [30, 31]. Starting from this finding, ph,hcp-POSS/ PS nanocomposites were thus prepared by *in situ* polymerization of styrene in the presence of 3, 5 and 10% w/w of filler [36]. The degradation experiments of all obtained nanocomposites showed a significant thermal stability enhancement in respect to neat polystyrene, which was larger for the sample at 5% filler [36].

On continuing our research in this field, we studied here the thermal degradation of PS based nanocomposites having two phenylsubstituted hcp-POSSs as fillers, namely 4-methoxyphenyl hcp-POSS (Fig-ure 1a), and 2,4-difluorophenyl hcp-POSS (Fig-ure 1b). These two fillers were selected among the various hepta cyclopentyl-POSSs investigated in Ref. [30] aiming to check if the presence of sub-stituents (electron-donor as the methoxy group or electron-withdrawing as fluorine atoms) in the phenyl group is able to affect the thermal stability of nanocomposites obtained.

Various nanocomposites were prepared by *in situ* polymerization of styrene in the presence of the appropriate POSS and will be indicated in the text by the corresponding numbers, as follows:

4-methoxyphenyl hcp-POSS/PS at 3% w/w	**1**
4-methoxyphenyl hcp-POSS/PS at 5% w/w	**2**
4-methoxyphenyl hcp-POSS/PS at 10% w/w	**3**
2,4-difluorophenyl hcp-POSS/PS at 3% w/w	**4**
2,4-difluorophenyl hcp-POSS/PS at 5% w/w	**5**
2,4-difluorophenyl hcp-POSS PS at 10% w/w	**6**

where the 3, 5 and 10% values represent the filler percentages in the reactant mixtures.

The actual filler content in the obtained nanocom-posites was checked by ^{1}H NMR. Also, inherent viscosity (η_{inh}) determinations were carried out in order to verify if the presence of POSS modified the average molar mass of PS, whilst Fourier Trans-form Infrared (FTIR) spectra were recorded to evi-dence the presence of PS-POSS interactions.

The glass transition temperature (T_g) of PS as well as those of the studied nanocomposites were deter-mined by Differential Scanning Calorimetry (DSC). Thermal (in flowing nitrogen) and thermoxidative (in a static air atmosphere) degradations were fol-
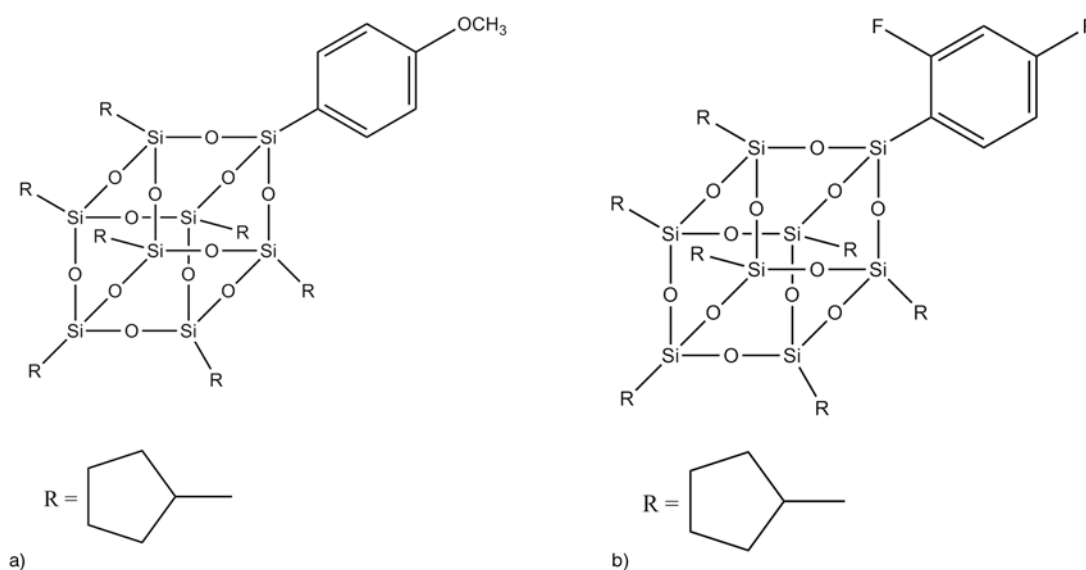
Figure 1. Molecular structure of a) 4-methoxyphenyl hcp-POSS; b) 2,4-difluorophenyl hcp-POSS

lowed by Thermogravimetric (TG) and Differential Thermogravimetric (DTG) analysis, and the parameters associated with the thermal stability, namely temperature at 5% mass loss ($T_{5\%}$) and apparent activation energy (E_a) of degradation, of various nanocomposites were determined and compared with each other and with those of neat PS and of ph,hcp-POSS/PS nanocomposites previously determined [36].

2. Experimental
2.1. Materials
Styrene (Aldrich Co., St. Gallen, CH) was purified by passing it through an inhibitor removal column. 2,2-Azobis(isobutyronitrile) (AIBN) (98% Aldrich Co., St. Gallen, CH) was re-crystallised twice from dry ethanol at temperatures less than 40°C and out of direct light. Toluene was stirred over calcium hydride for 24 h and distilled in a nitrogen atmosphere.

Tetrahydrofuran (THF) was distilled over a Na – benzophenone mixture.

2.2. Synthesis of POSSs
POSSs were first prepared as follows: 4-methoxyphenyltrichlorosilane and 2,4-difluorophenyltrichlorosilane were prepared from the appropriate Grignard reagent and $SiCl_4$ [37, 38]. Cyclopentyltrisilanol (c $C_5H_9)_7$-$Si_7O_9(OH)_3$ was obtained by literature methods [39, 40].

4-methoxyphenyl hcp-POSS and 2,4-difluorophenyl hcp-POSS were prepared by corner capping reaction of cyclopentyltrisilanol with the suitable aryltrichlorosilane in dry THF, according to our previous work [30].

2.3. Synthesis of nanocomposites
Nanocomposites were obtained by *in situ* polymerization of 3, 5 and 10% w/w POSS/styrene mixtures in toluene. The details of free-radical polymerization procedure are described for compound **2**.

Styrene monomer (3,80 g) and 4-methoxyphenyl hcp-POSS (0,20 g) were dissolved in 40 ml of toluene, and AIBN radical initiator (12 mg) was added; the mixture was frozen in a liquid nitrogen bath, degassed with a vacuum pump, and then thawed. This operation was repeated three times and then tube, sealed under vacuum, was heated at 70°C for 24 h under stirring. The clear solution was poured into a large excess of methanol (600 mL), the precipitated nanocomposite was collected by filtration and dried under vacuum at 40°C. The yield was 3.52 g (88%).

The same polymerization procedure was used to prepare neat PS and compounds **1** (yield 85%), **3** (yield 79%), **4** (yield 84%), **5** (yield 81%) and **6** (yield 86 %).

2.4. ^{1}H NMR spectroscopy
^{1}H NMR spectra were recorded by a Varian (Palo Alto, California, USA) Unity Inova instrument (^{1}H 500 MHz), by using $CDCl_3$ as solvent and TMS as internal standard.

2.5. Viscosity measurements
Inherent viscosities ($\eta_{inh} = \ln\eta_r/C$, where η_r = relative viscosity and C = polymer concentration) at 25 ± 0.1°C were measured with an Ubbelohde suspended-level viscometer, using solutions of polymers in chloroform at the concentration of 0.5 g/dL.

2.6. IR spectroscopy
A Perkin Elmer (Waltham, Massachusetts, USA) Spectrum 100 spectrometer was used to record Fourier Transform Infrared (FTIR), using an universal ATR sampling accessory. Spectra were recorded at r.t. from 4000 to 400 cm^{-1} with a resolution of 4.0 cm^{-1}, directly on compounds, without any preliminary treatment.

2.7. DSC measurements
A Mettler (Greifensee, CH) DSC 20 differential scanning calorimeter, coupled with a Mettler (Greifensee, CH) TC 10 A processor as control and evaluation unit, was employed for the determination of glass transition temperature. The enthalpy and temperature calibrations of equipment were made according to the procedure suggested by the manufacturer and reported in our previous work [36]. Calibrations were repeated every two weeks. Samples of about $5.0 \cdot 10^{-3}$ g, held in sealed aluminium crucibles, and a heating rate of 10°C·min^{-1} were used for measurements.

2.8. Thermogravimetric analysis
The thermal degradations of the studied compounds were carried out into a Mettler (Greifensee, CH) TA 3000 thermogravimetric analyser, coupled with the

same Mettler TC 10 A processor used for calorimetric measurements. The temperature calibration of the thermobalance was made according to the reliable procedure suggested by the supplier. The temperature calibration was repeated every month. Degradation experiments were carried out in dynamic heating conditions, from 35 to 700°C, in both flowing nitrogen (0.02 L·min^{-1}) and a static air atmosphere, at various heating rates (Φ = 2, 5, 7.5, 10, 12.5, 15, 17.5 and 20°C·min^{-1}). Samples of about 5·10^{-3} g, held in alumina open crucibles, were used for experiments, and their weights were measured as a function of temperature and stored in the list of data of the appropriate built-in program of processor. The TG and DTG curves were then immediately printed at the end of each experiment, while the list of sample weights at various temperatures was transferred to a PC. These data were afterwards used to plot the percentage of undegraded sample, $(1 - D)$%, as a function of temperature, where $D = (W_0 - W)/W_0$, and W_0 and W were the weights at the starting point and during scanning.

3. Results and discussion

The ^{1}H NMR spectra of the **1–6** nanocomposites were first recorded and the actual POSS content in the various compounds was determined through the ratio of aromatic hydrogen atoms of filler and those of polystyrene. The following POSS percentages, which in all cases were higher than those of reactant mixtures, were found, namely 3.6% (sample **1**), 6.8% (sample **2**), 12.0% (sample **3**), 3.7% (sample **4**), 6.9% (sample **5**) and 11.8% (sample **6**).

Inherent viscosity determinations on studied compounds were thus performed. The η_{inh} values obtained with samples **1**, **2** and **3** were the same than those of neat PS and ph,hcp-POSS/PS nanocomposites pre-

viously determined [36]. Conversely, all values found for samples **4**, **5** and **6** were lower, and, in particular, those at higher POSS content evidenced a dramatic η_{inh} decrease, thus indicating a lower polymer average molar masses. The values of inherent viscosity are reported in Table 1.

The thermal degradations of samples were carried out into our thermobalance, in both inert and oxidative atmospheres. In order to compare the thermal stabilities of our compounds with each other and with those of neat polystyrene and ph,hcp-POSS/PS nanocomposites previously studied, both temperature at 5% mass loss ($T_{5\%}$), which is correlated with initial decomposition temperature (T_i), and activation energy (E_a) of degradation were determined. Temperature at 5% mass loss was chosen because it appears to us more reliable than initial decomposition temperature, because this last parameter largely depends on the slope of the descending piece of TG curve [30, 36, 41–43]. In addition, since to evaluate the comprehensive thermal stability of a polymer it is necessary, in our opinion, to take into account also the degradation rate, in particular if the compared compounds have close initial decomposition temperatures, the apparent activation energy of degradation was determined.

Degradation experiments were first carried out in inert atmosphere, under dynamic heating conditions, at various heating rates ranging from 2 to 20°C·min^{-1}. $T_{5\%}$ values were drawn from the curves traced at the rate of 10°C·min^{-1}, which was selected because it is a medium scanning rate among those used for thermal degradations. The studied nanocomposites degraded completely in flowing nitrogen at all used heating rates. The corresponding TG degradation curves at 10°C·min^{-1} for methoxy- and difluoro- derivatives are reported in Figures 2 and 3,

Table 1. Inherent viscosity (η_{inh}), glass transition temperature (T_g), temperature at 5% mass loss ($T_{5\%}$), apparent activation energy (E_a) of degradation of **PS** and various nanocomposites in static air atmosphere and in flowing nitrogen

Compounds	Air static atmosphere				Nitrogen flow	
	η_{inh} [dL·g^{-1}]	T_g [K]^a	$T_{5\%}$ [K]^a	E_a [kJ·mol^{-1}]	$T_{5\%}$ [K]^a	E_a [kJ·mol^{-1}]
PS	0.17	372	511	141 ($\pm$6)	573	206 ($\pm$11)
1	0.17	372	546	155 ($\pm$ 8)	581	221 ($\pm$ 7)
2	0.17	373	569	168 ($\pm$ 8)	588	242 ($\pm$ 13)
3	0.17	372	558	164 ($\pm$ 7)	583	238 ($\pm$ 13)
4	0.16	369	555	155 ($\pm$ 7)	579	225 ($\pm$ 8)
5	0.12	368	550	152 ($\pm$ 8)	570	224 ($\pm$ 10)
6	0.12	368	530	150 ($\pm$ 8)	567	221 ($\pm$ 11)

^{a}determined at 10°C·min^{-1}
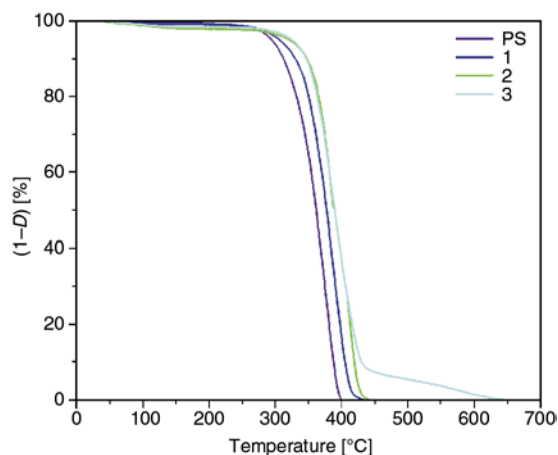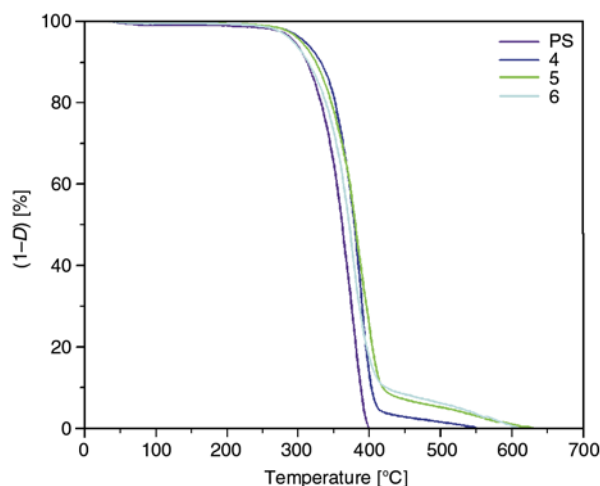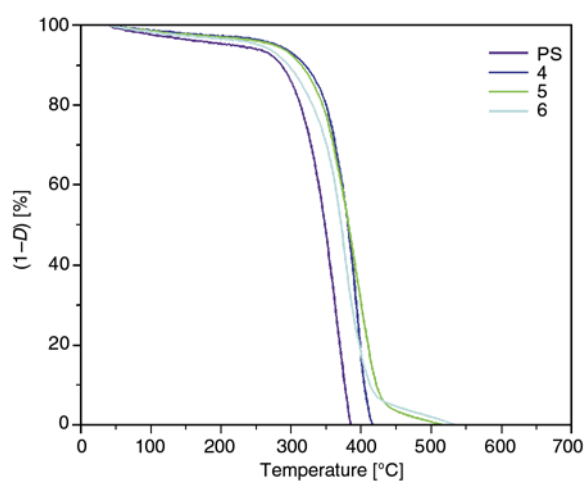
Figure 2. TG degradation curves, at 10°C·min^{-1}, under nitrogen flow of PS and various 4-methoxyphenyl hcp-POSS/PS nanocomposites
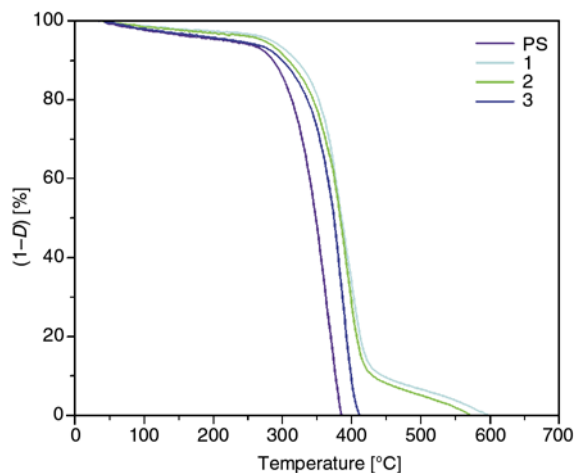
Figure 4. TG degradation curves, at 10°C·min^{-1}, in static air atmosphere of PS and various 4-methoxyphenyl hcp-POSS/PS nanocomposites

Figure 3. TG degradation curves, at 10°C·min^{-1}, under nitrogen flow of PS and various 2,4-difluorophenyl hcp-POSS/PS nanocomposites

Figure 5. TG degradation curves, at 10°C·min^{-1}, in static air atmosphere of PS and various 2,4-difluorophenyl hcp-POSS/PS nanocomposites

respectively, while the determined $T_{5\%}$ values are listed in Table 1. The behaviour of our compounds in oxidative atmosphere (Figures 4 and 5) was similar to that under nitrogen and the corresponding $T_{5\%}$ values are listed in Table 1.

The nanocomposites degraded up to complete mass loss at all used heating rates, but, differently than PS, which completely degraded in a very sharp single stage, they showed a first quick degradation stage, followed by a slow second one in the last piece of TG curve, more evident for the high filler content samples. This behaviour was the same as that of the ph,hcp-POSS/PS nanocomposites previously studied [36], for which it was there demonstrated that during the second low rate degradation stage both polymer and filler were present at tem-

peratures largely higher than that of the complete decomposition of neat PS, thus indicating a thermal stabilisation of polymer.

The degradation E_a values of various compounds, in both flowing nitrogen and static air atmosphere, were thus determined by using the data from DTG degradation curves at the various heating rates. The classical Kissinger method [44] was used to this aim, which is based on Equation (1):

$$\ln\left(\frac{\Phi}{T_m^2}\right) = \ln\left(\frac{n\mathrm{R}AW_m^{n-1}}{E_n}\right) - \frac{E_a}{\mathrm{R}T_m} \qquad (1)$$

where Φ is the heating rate, T_m is the temperature at maximum rate of weight loss, n is the apparent reaction order, R is the universal gas constant, A is the pre-exponential factor and W_m is the weight of

sample at the maximum rate of mass loss. We used as T_m values the temperatures of DTG peaks. The E_a value was obtained through the linear dependence of $\ln(\Phi/T_m^2)$ on $1/T_m$ at various heating rates. The least square treatment of T_m values was then performed according to the Equation (1). Single linear $\ln(\Phi/T_m^2)$ vs $1/T_m$ relationships were obtained for all samples in both studied environments. The corresponding regression coefficients and the calculated degradation E_a values are reported in Tables 2 and 3 for nitrogen and air, respectively.

The glass transition temperatures of the considered compounds were lastly determined by DSC measurements, and the values found are reported in Table 1 together with η_{inh}, $T_{5\%}$ and degradation E_a values.

Some comments about the results reported in Table 1:

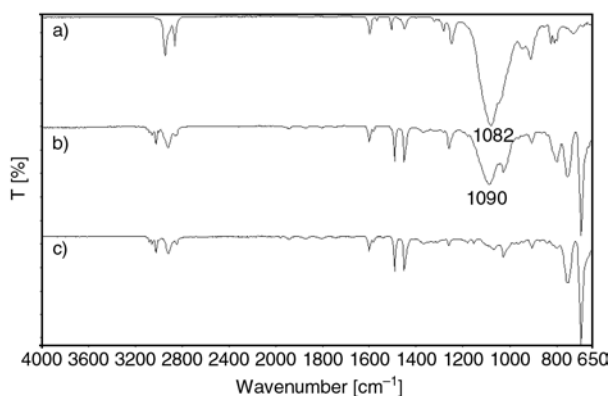– the ^{1}H NMR spectra indicated that the POSS content in nanocomposites is higher than that in the reactant mixtures. This finding is in agreement with the results obtained for ph,hcp-POSS/PS nanocomposites [36];
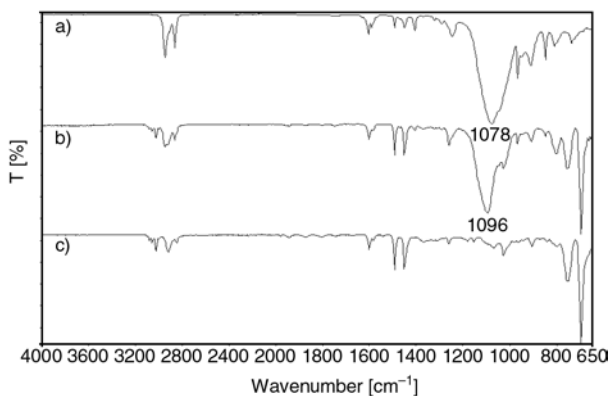
– the much lower η_{inh} values of difluoro- compounds **4**, **5** and **6** in respect to those of both neat PS and methoxy-compounds **1**, **2** and **3** here studied, as well as to those of the previously investigated ph,hcp-POSS/PS nanocomposites, indicate lower average molecular weight, and then a lower polymerization degree of PS. Also, the dramatic η_{inh} decrease observed on increasing the fluorinated POSS concentration suggests that this filler behaves as polymerization inhibitor;

– also glass transition temperatures exhibited different behaviour between the two series of studied compounds: no difference was observed for methoxy-derivatives with each other as well as in respect to neat **PS** and ph,hcp-POSS/PS nanocomposites [36]. Conversely lower T_g values were found for the difluoro- derivates, which decreased on increasing POSS percentage. Since it is well known that glass transition temperature increases with the increase of molecular weight [45], these results appear to be in agreement with viscosimetric measurements and confirm the lower average molar mass of **PS** in the **4**, **5** and **6** nanocomposites;

– as regards degradation experiments, the picture of results in both inert and oxidative environments (Table 1) did not show any substantial difference of behaviour between the 4-methoxyphenyl hcp-POSS/PS nanocomposites (samples **1**, **2** and **3**) here studied and the unsubstituted ph,hcp-POSS/PS nanocomposites previously investigated [36]. Both $T_{5\%}$ and degradation E_a values determined for **1**, **2** and **3** samples were quite higher than those of neat polystyrene, and slightly, but not significantly, different from those found for ph,hcp-POSS/PS nanocomposites [36]. The best values were found for the sample at 5% of POSS, thus suggesting a similar overall thermal stability of the two groups of compounds, in every case better than that of pure polymer. A different behaviour was observed with fluorinated nanocomposites: both $T_{5\%}$ and degradation E_a values of **4**, **5** and **6** samples were lower than those of **1**, **2** and **3** samples. Also, they decreased with the increase of POSS content and, in some cases ($T_{5\%}$ values of samples **5** and **6**

Table 2. Regression coefficients and apparent activation energy (E_a) of degradation by the Kissinger equation for **PS** and nanocomposites in flowing nitrogen

Compounds	a [a)]	$b \cdot 10^{-3}$ [K] [b)]	r [c)]	E_a [kJ·mol^{-1}]
PS	27.3 (± 2.0)	24.8 (± 1.3)	0.9919	206 (± 11)
1	29.5 (± 1.2)	26.6 (± 0.8)	0.9975	221 (± 7)
2	31.9 (± 2.4)	29.1 (± 1.6)	0.9906	242 (± 13)
3	31.3 (± 2.3)	28.6 (± 1.6)	0.9909	238 (± 13)
4	30.3 (± 1.5)	27.1 (± 1.0)	0.9962	225 (± 8)
5	30.4 (± 1.8)	27.0 (± 1.2)	0.9940	224 (± 10)
6	30.2 (± 2.0)	26.6 (± 1.3)	0.9927	221 (± 11)

[a)]$a = \ln(nRAW_m^{n-1}/E_a)$
[b)]$b = E_a/R$
[c)]product moment correlation coefficient

Table 3. Regression coefficients and apparent activation energy (E_a) of degradation by the Kissinger equation for **PS** and nanocomposites in static air atmosphere

Compounds	a [a)]	$b \cdot 10^{-3}$ [K] [b)]	r [c)]	E_a [kJ·mol^{-1}]
PS	15.5 (± 1.1)	17.0 (± 0.7)	0.9950	141 (± 6)
1	17.4 (± 1.5)	18.7 (± 1.0)	0.9915	155 (± 8)
2	19.9 (± 1.3)	20.2 (± 0.9)	0.9944	168 (± 8)
3	19.3 (± 1.2)	19.7 (± 0.8)	0.9950	164 (± 7)
4	17.1 (± 1.4)	18.6 (± 0.9)	0.9927	155 (± 7)
5	16.9 (± 1.5)	18.3 (± 1.0)	0.9916	152 (± 8)
6	17.0 (± 1.5)	18.1 (± 1.0)	0.9911	150 (± 8)

[a)]$a = \ln(nRAW_m^{n-1}/E_a)$
[b)]$b = E_a/R$
[c)]product moment correlation coefficient

under nitrogen), were lower than neat PS. These results suggest a negative influence of our fluorinated POSS on the thermal stability of nanocomposites.

In order to interpret the different behaviour of the two groups of compounds, the IR spectra of neat PS, of both 4-methoxyphenyl hcp-POSS and 2,4-difluorophenyl hcp-POSS, as well as those of compounds **3** and **6**, were carried out. Compounds **3** and **6** were selected for these experiments because they are those with the most high filler content. The IR spectra of methoxy- POSS and methoxy- nanocomposite, as well as those of fluorinated- POSS and fluorinated- nanocomposite, are reported in Figures 6 and 7, respectively, together with that of PS. The spectra of nanocomposites, if compared with those of PS and corresponding POSSs, show the shift of the characteristic sharp band attributable to Si–O bonds from 1082 cm^{-1} (of 4-methoxyphenyl hcp-POSS) and 1078 cm^{-1} (of 2,4-difluorophenyl hcp-POSS), to 1090 cm^{-1} and 1096 cm^{-1} in the IR spectra of compounds **3** and **6**, respectively, thus

suggesting the presence of filler-polymer interactions in both series of nanocomposites, to which the Si–O bond of POSS cage is assigned.

The thermal degradations in air of both **3** and **6** samples were then carried out from r.t. up to 450°C. This temperature, at which the mass of samples is 10% about of initial mass, was chosen because it is roughly the starting temperature of the low rate degradation stage.

The IR spectra of the residues so obtained were compared with the IR spectrum of residue at 380°C (10% about of initial sample mass) from the degradation of neat PS (Figures 8 and 9 for methoxy- and fluorinated- derivatives, respectively).

The presence in both the IR spectra of the residues from samples **3** and **6** of the band at 697 cm^{-1} as well as of some weak bands in the 2900–3100 cm^{-1} range, which are characteristic of PS, clearly indicates that when nanocomposites degrade polymer is still present at temperatures largely higher than that at which the complete mass loss of neat PS is observed (Figure 4).

Figure 6. FTIR spectra of 4-methoxyphenyl hcp-POSS (a), sample **3** (b) and PS (c)
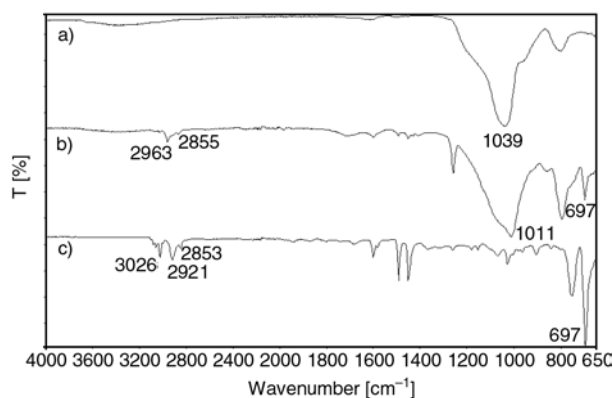
Figure 8. FTIR spectra of the residues of 4-methoxyphenyl hcp-POSS (a), sample **3** (b) and PS (c) after thermal degradation in static air atmosphere

Figure 7. FTIR spectra of 2,4-difluorophenyl hcp-POSS (a), sample **6** (b) and PS (c)
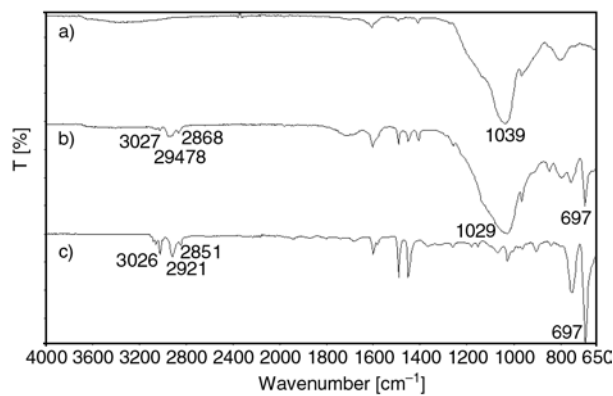
Figure 9. FTIR spectra of the residues of 2,4-difluorophenyl hcp-POSS (a), sample **6** (b) and PS (c) after thermal degradation in static air atmosphere

Since no qualitative difference was found in the IR behaviour of both methoxy- and difluoro- nano-composites before degradation as well as in the final stage of degradation, the worse thermal behaviour of fluorinated nanocomposites can not be due, on the basis of spectrophotometric experiments, to the lack of filler-polymer interactions. It could be thus attributed, in our opinion, to lower average molar mass of PS in fluorinated nanocomposites, as evidenced by both viscosity and glass transition temperature determinations. This hypothesis agrees very well with literature data showing that the onset temperature of PS pyrolysis (which corresponds at $T_{5\%}$ about) in air decreases on decreasing the polymer average molar mass [46].

4. Conclusions

In a previous work we synthesized some ph,hcp-POSS/PS nanocomposites by the direct polymerization *in situ* of styrene in the presence of different amounts of filler, and the obtained results indicated a much higher thermal stability of nanocomposites than that of the virgin polymer. On continuing our research in this field, we would verify, in the present work, if the substitution of hydrogen atoms of POSS phenyl group with electron-donor (methoxy-) or electron-withdrawing (fluorine-) groups was able to affect the thermal stability of nanocomposites through the formation of differently strong (or through the lack of) POSS-polymer interactions. We expected some changes of the characteristic parameters of thermal stability in respect to unsubstituted ph,hcp-POSS/PS nanocomposites, but opposite for the two groups of studied compounds. The results until now obtained drive us to suppose that no significant difference of filler-polymer interactions occurs between the two groups of compounds. The decrease of thermal stability observed for difluoro-nanocomposites appears due to the lower polymerization degree of PS which could be attributable to the presence of fluorinated POSS during the *in situ* polymerization process.

References

[1] Hussain F., Hojjati M., Okamoto M., Gorga R. E.: Polymer-matrix nanocomposites, processing, manufacturing, and application: An overview. Journal of Composite Materials, **40**, 1511–1575 (2006). DOI: 10.1177/0021998306067321

[2] Giannelis E. P.: Polymer layered silicate nanocomposites. Advanced Materials, **8**, 29–35 (1996). DOI: 10.1002/adma.19960080104

[3] Wu C. L., Zhang M. Q., Rong M. Z., Friedrich K.: Tensile performance improvement of low nanoparticles filled-polypropylene composites. Composites Science and Technology, **62**, 1327–1340 (2002). DOI: 10.1016/S0266-3538(02)00079-9

[4] Lee M. W., Hu X., Li L., Yue C. Y., Tam K. C., Cheong L. Y.: PP/LCP composites: Effects of shear flow, extensional flow and nanofillers. Composites Science and Technology, **63**, 1921–1929 (2003). DOI: 10.1016/S0266-3538(03)00156-8

[5] Hasan M. M., Zhou Y., Mahfuz H., Jeelani S.: Effect of SiO$_2$ nanoparticle on thermal and tensile behavior of nylon-6. Materials Science and Engineering A, **429**, 181–188 (2006). DOI: 10.1016/j.msea.2006.05.124

[6] Zhang M. Q., Rong M. Z., Yu S. L., Wetzel B., Friedrich K.: Effect of particle surface treatment on the tribological performance of epoxy based nanocomposites. Wear, **253**, 1086–1093 (2002). DOI: 10.1016/S0043-1648(02)00252-1

[7] Zhou S., Wu L., Sun J., Shen W.: The change of the properties of acrylic-based polyurethane via addition of nano-silica. Progress in Organic Coatings, **45**, 33–42 (2002). DOI: 10.1016/S0300-9440(02)00085-1

[8] Zhang C., Babonneau F., Bonhomme C., Laine R. M., Soles C. L., Hristov H. A., Yee A. F.: Highly porous polyhedral silsesquioxane polymers. Synthesis and characterization. Journal of the American Chemical Society, **120**, 8366–8379 (1998). DOI: 10.1021/ja9808853

[9] Kim S. G., Choi J., Tamaki R., Laine R. M.: Synthesis of amino-containing oligophenylsilsesquioxanes. Polymer, **46**, 4514–4524 (2005). DOI: 10.1016/j.polymer.2005.02.036

[10] Liu H., Kondo S-I., Takeda N., Unno M.: Synthesis of octacarboxy spherosilicate. Journal of the American Chemical Society, **130**, 10074–10075 (2008). DOI: 10.1021/ja803513n

[11] Feher F. J., Wyndham K. D., Scialdone M. A., Hamuro Y.: Octafunctionalized polyhedral oligosilsesquioxanes as scaffolds: Synthesis of peptidyl silsesquioxanes. Chemical Communications, **1998**, 1469–1470 (1998). DOI: 10.1039/A802671H

[12] Li G., Wang L., Ni H., Pittman C.: Polyhedral oligomeric silsesquioxane (POSS) polymers and copolymers: A review. Journal of Inorganic and Organometallic Polymers, **11**, 123–154 (2001). DOI: 10.1023/A:1015287910502

[13] Schwab J. J., Lichtenhan J. D.: Polyhedral oligomeric silsesquioxane(POSS)-based polymers. Applied Organometallic Chemistry, **12**, 707–713 (1998). DOI: 10.1002/(SICI)1099-0739(199810/11)12:10/11<707::AID-AOC776>3.0.CO;2-1

[14] Hanssen R. W. J. M., van Santen R. A., Abbenhuis H. C. L.: The dynamic status quo of polyhedral silsesquioxane coordination chemistry. European Journal of Inorganic Chemistry, **2004**, 675–683 (2004). DOI: 10.1002/ejic.200300412

[15] Phillips S. H., Haddad T. S., Tomczak S. J.: Developments in nanoscience: Polyhedral oligomeric silsesquioxane (POSS)-polymers. Current Opinion in Solid State and Materials Science, **8**, 21–29 (2004). DOI: 10.1016/j.cossms.2004.03.002

[16] Lin H-C., Kuo S-W., Huang C-F., Chang F-C.: Thermal and surface properties of phenolic nanocomposites containing octaphenol polyhedral oligomeric silsesquioxane. Macromolecular Rapid Communications, **27**, 537–541 (2006). DOI: 10.1002/marc.200500852

[17] Gunji T., Okonogi H., Sakan T., Takamura N., Arimitsu K., Abe Y.: Preparation and properties of organic–inorganic hybrid gel films based on polyvinylpolysilsesquioxane synthesized from trimethoxy(vinyl) silane. Applied Organometallic Chemistry, **17**, 580–588 (2003). DOI: 10.1002/aoc.470

[18] Gunji T., Sakai Y., Arimitsu K., Abe Y.: Preparation and properties of polyethoxysilsesquioxane-C60 hybrids. Journal of Polymer Science Part A: Polymer Chemistry, **45**, 3273–3279 (2007). DOI: 10.1002/pola.22076

[19] Takamura N., Gunji T., Hatano H., Abe Y.: Preparation and properties of polysilsesquioxanes: Polysilsesquioxanes and flexible thin films by acid-catalyzed controlled hydrolytic polycondensation of methyl- and vinyltrimethoxysilane. Journal of Polymer Science Part A: Polymer Chemistry, **37**, 1017–1026 (1999). DOI: 10.1002/(SICI)1099-0518(19990401)37:7<1017 ::AID-POLA16>3.0.CO;2-F

[20] Abate L., Blanco I., Bottino F. A., Di Pasquale G., Fabbri E., Orestano A., Pollicino A.: Kinetic study of the thermal degradation of PS/MMT nanocomposites preparedwith imidazolium surfactants. Journal of Thermal Analysis and Calorimetry, **91**, 681–686 (2008). DOI: 10.1007/s10973-007-8577-7

[21] Olewnik E., Garman K., Czerwiński W.: Thermal properties of new composites based on nanoclay, polyethylene and polypropylene. Journal of Thermal Analysis and Calorimetry, **101**, 323–329 (2010). DOI: 10.1007/s10973-010-0690-3

[22] Lomakin S. M., Dubnikova I. L., Shchegolikhin A. N., Zaikov G. E., Kozlowski R., Kim G-M., Michler G. H.: Thermal degradation and combustion behavior of the polyethylene/clay nanocomposite prepared by melt intercalation. Journal of Thermal Analysis and Calorimetry, **94**, 719–726 (2008). DOI: 10.1007/s10973-008-9355-x

[23] Fina A., Tabuani D., Frache A., Camino G.: Polypropylene–polyhedral oligomeric silsesquioxanes (POSS) nanocomposites. Polymer, **46**, 7855–7866 (2005). DOI: 10.1016/j.polymer.2005.06.121

[24] Weickmann H., Delto R., Thomann R., Brenn R., Döll W., Mülhaupt R.: PMMA nanocomposites and gradient materials prepared by means of polysilsesquioxane (POSS) self-assembly. Journal of Materials Science, **42**, 87–92 (2007). DOI: 10.1007/s10853-006-1044-1

[25] Jones I. K., Zhou Y. X., Jeelani S., Mabry J. M.: Effect of polyhedral-oligomeric-sil-sesquioxanes on thermal and mechanical behavior of SC-15 epoxy. Express Polymer Letters, **2**, 494–501 (2008). DOI: 10.3144/expresspolymlett.2008.59

[26] Zaioncz S., Dahmouche K., Paranhos C. M., San Gil R. A. S., Soares B. G.: Relationships between nanostructure and dynamic-mechanical properties of epoxy network containing PMMA-modified silsesquioxane. Express Polymer Letters, **3**, 340–351 (2009). DOI: 10.3144/expresspolymlett.2009.43

[27] Zou J., Chen X., Jiang X. B., Zhang J., Guo Y. B., Huang F. R.: Poly(L-lactide) nanocomposites containing octaglycidylether polyhedral oligomeric silsesquioxane: Preparation, structure and properties. Express Polymer Letters, **5**, 662–673 (2011). DOI: 10.3144/expresspolymlett.2011.65

[28] Spoljaric S., Shanks R. A.: Novel elastomer dye-functionalised POSS nanocomposites: Enhanced colourimetric, thermomechanical and thermal properties. Express Polymer Letters, **6**, 354–372 (2012). DOI: 10.3144/expresspolymlett.2012.39

[29] Wang X., Wu L., Li J.: Preparation of nano poly(phenylsilsesquioxane) spheres and the influence of nano-PPSQ on the thermal stability of poly(methyl methacrylate). Journal of Thermal Analysis and Calorimetry, **105**, 323–329 (2012). DOI: 10.1007/s10973-011-1619-1

[30] Blanco I., Abate L., Bottino F. A., Bottino P., Chiacchio M. A.: Thermal degradation of differently substituted cyclopentyl polyhedral oligomeric silsesquioxane (CP-POSS) nanoparticles. Journal of Thermal Analysis and Calorimetry, **107**, 1083–1091 (2012). DOI: 10.1007/s10973-011-1848-3

[31] Blanco I., Abate L., Bottino F. A., Bottino P.: Hepta isobutyl polyhedral oligomeric silsesquioxanes (hib-POSS): A thermal degradation study. Journal of Thermal Analysis and Calorimetry, **108**, 807–815 (2012). DOI: 10.1007/s10973-011-2050-3

[32] Fina A., Tabuani D., Carniato F., Frache A., Boccaleri E., Camino G.: Polyhedral oligomeric silsesquioxanes (POSS) thermal degradation. Thermochimica Acta, **440**, 36–42 (2006). DOI: 10.1016/j.tca.2005.10.006

[33] Bolln C., Tsuchida A., Frey H., Mülhaupt R.: Thermal properties of the homologous series of 8-fold alkyl-substituted octasilsesquioxanes. Chemistry of Materials, **9**, 1475–1479 (1997).
DOI: 10.1021/cm970090f

[34] Mantz R. A., Jones P. F., Chaffee K. P., Lichtenhan J. D., Gilman J. W., Ismail I. M. K., Burmeister M. J.: Thermolysis of polyhedral oligomeric silsesquioxane (POSS) macromers and POSS–siloxane copolymers. Chemistry of Materials, **8**, 1250–1259 (1996).
DOI: 10.1021/cm950536x

[35] Fina A., Tabuani D., Frache A., Boccaleri E., Camino G.: Octaisobutyl POSS thermal degradation. in 'Fire retardancy of polymers: New applications of mineral fillers' (eds.: Le Bras M., Wilkie C., Bourbigot S.) Royal Society of Chemistry, Cambridge, 202–222 (2005).

[36] Blanco I., Abate L., Bottino F. A., Bottino P.: Thermal degradation of hepta cyclopentyl, mono phenyl-polyhedral oligomeric silsesquioxane (hcp-POSS)/polystyrene (PS) nanocomposites. Polymer Degradation and Stability, **97**, 849–855 (2012).
DOI: 10.1016/j.polymdegradstab.2012.03.041

[37] Rosenberg S. D., Walburn J. J., Ramsden H. E.: Preparation of some arylchlorosilanes with arylmagnesium chlorides. The Journal of Organic Chemistry, **22**, 1606–1607 (1957).
DOI: 10.1021/jo01363a019

[38] Breed L. W., Haggerty W. J. Jr.: Aryl and alkylchloro-dialkoxysilanes. The Journal of Organic Chemistry, **25**, 126–128 (1960).
DOI: 10.1021/jo01071a036

[39] Feher F. J., Newman D. A.: Enhanced silylation reactivity of a model for silica surfaces. Journal of the American Chemical Society, **112**, 1931–1936 (1990).
DOI: 10.1021/ja00161a044

[40] Feher F. J., Budzichowski T. A., Blanski R. L., Weller K. J., Ziller J. W.: Facile syntheses of new incompletely condensed polyhedral oligosilsesquioxanes: $[(c-C_5H_9)_7Si_7O_9(OH)_3]$, $[(c-C_7H_{13})_7Si_7O_9(OH)_3]$, and $[(c-C_7H_{13})_6Si_6O_7(OH)_4]$. Organometallics, **10**, 2526–2528 (1991).
DOI: 10.1021/om00053a070

[41] Abate L., Blanco I., Motta O., Pollicino A., Recca A.: The isothermal degradation of some polyetherketones: A comparative kinetic study between long-term and short-term experiments. Polymer Degradation and Stability, **75**, 465–471 (2002).
DOI: 10.1016/S0141-3910(01)00249-X

[42] Abate L., Blanco I., Orestano A., Pollicino A., Recca A.: Kinetics of the isothermal degradation of model polymers containing ether, ketone and sulfone groups. Polymer Degradation and Stability, **87**, 271–278 (2005).
DOI: 10.1016/j.polymdegradstab.2004.06.011

[43] Abate L., Blanco I., Cicala G., Mamo A., Recca G., Scamporrino A.: The influence of chain rigidity on the thermal properties of some novel random copolyether-sulfones. Polymer Degradation and Stability, **95**, 798–202 (2010).
DOI: 10.1016/j.polymdegradstab.2010.02.002

[44] Kissinger H. E.: Reaction kinetics in differential thermal analysis. Analytical Chemistry, **29**, 1702–1706 (1957).
DOI: 10.1021/ac60131a045

[45] Chartoff R. P.: Thermoplastic polymers. in 'Thermal characterization of polymeric materials' (ed.: Turi A.) Academic Press, San Diego, 621–626 (1997).

[46] Heitz M., Carrasco F., Overend R. P., Chornet E.: Correlation between polystyrene molecular weights and a characteristic temperature derived from the thermogravimetric weight loss curves. Thermochimica Acta, **142**, 83–88 (1989).
DOI: 10.1016/0040-6031(89)85008-7

Investigation of polymer electrolytes based on agar and ionic liquids

R. Leones[1], F. Sentanin[2], L. C. Rodrigues[1], I. M. Marrucho[3], J. M. S. S. Esperança[3], A. Pawlicka[2], M. M. Silva[1*]

[1]Centro de Química, Universidade do Minho, Gualtar, 4710-057 Braga, Portugal
[2]Instituto de Química de São Carlos, Universidade de São Paulo, CxP 780, 13560-970 São Carlos, SP, Brazil
[3]Instituto de Tecnologia Química e Biológica, Universidade Nova de Lisboa, www.itqb.unl.pt, 2780-157 Oeiras, Portugal

Abstract. The possibility to use natural polymer as ionic conducting matrix was investigated in this study. Samples of agar-based electrolytes with different ionic liquids were prepared and characterized by physical and chemical analyses. The ionic liquids used in this work were 1-ethyl-3-methylimidazolium ethylsulfate, $[C_2mim][C_2SO_4]$, 1-ethyl-3-methylimidazolium acetate, $[C_2mim][OAc]$ and trimethyl-ethanolammonium acetate, $[Ch][OAc]$.
Samples of solvent-free electrolytes were prepared and characterized by ionic conductivity measurements, thermal analysis, electrochemical stability, X-ray diffraction, scanning electron microscopy and Fourier Transform infrared spectroscopy. Electrolyte samples are thermally stable up to approximately 190°C. All the materials synthesized are semicrystalline. The electrochemical stability domain of all samples is about 2.0 V *versus* Li/Li$^+$. The preliminary studies carried out with electrochromic devices (ECDs) incorporating optimized compositions have confirmed that these materials may perform as satisfactory multifunctional component layers in the field of 'smart windows', as well as ECD-based devices.

Keywords: biodegradable polymers, smart polymer, thermal properties, Agar matrix

1. Introduction

Polymer electrolytes (PEs) are ionically conducting materials that may be used in the fabrication of solid-state electrochemical devices, particularly rechargeable batteries, electrochromic displays, capacitors and sensors [1, 2]. During the last decades different systems have been extensively studied and most of them were based on poly(ethylene oxide) [2]. More recently new types of electrolytes based on natural polymers (like cellulose derivatives, chitosan, starch or natural rubber) have been proposed due to their biodegradability, low production cost, good physical and chemical properties and good performance as SPEs (solvent-free polymer electrolytes) [3–5]. Among these there is agar, which is an heterogeneous mixture of agaropectin and agarose

[6]. Recently, natural macromolecules are the goal of the new materials research tendencies due to the increasing alerts concerning the contribution of synthetic polymers to the environmental destruction [7, 8]. The main argument for the use of bio-macromolecules is their extraction from renewable sources, as fast growing plants, animals and crustacean or also by bacterial synthesis [9, 10] and consequently their biodegradation properties.

In spite of SPEs potential, their application in commercial devices has been delayed because of their tendency to crystallize, substantially lower ionic conductivity than non-aqueous liquid electrolytes and a tendency to salt exudation at high salt concentration. However, as liquid electrolytes pose significant safety and environmental concerns, in recent

---

*Corresponding author, e-mail: nini@quimica.uminho.pt

years considerable efforts have been devoted to increase the ionic conductivity and improve the mechanical properties of SPEs [1, 2].

In order to do so, many research groups turned their attention to room temperature ionic liquids (RTILs) [11]. The introduction of ionic liquids (ILs) into macromolecules structure has been presented as a very interesting way to obtain good ionic conductivity without liquid components [12–14]. These polymer electrolytes based on ILs have been developed for battery electrolyte and for other solid electrolyte applications [15, 16]. It was successfully demonstrated that the electrochemical stability and ionic conductivity of SPEs are enhanced by the addition of ILs. Also, their addition ensures safety, owing to some intrinsic properties of ILs such as their almost zero volatility [17], zero flammability [18] and high thermal stability [19].

This paper describes the preparation and characterization of agar-based polymer electrolytes with ionic liquids as guest salts. Looking for good conductivity results combined with transparency, flexibility, good adhesion, good mechanical and electrochemical properties, electrolytes were characterized by conductivity measurements, thermal analysis (DSC and TGA), cyclic voltammetry, X-ray diffraction (XRD) and scanning electron microscopy (SEM). These materials were also tested as ionic conductors in electrochromic devices with the following configuration: glass/ITO/WO_3/PolymerElectrolyte/ CeO_2–TiO_2/ITO/glass.

2. Experimental
2.1 Materials
Ionic liquids. The ionic liquids used in this work were 1-ethyl-3-methylimidazolium ethylsulfate (IL-0033-HP/342573-75-5), [C_2mim][C_2SO_4], 1-ethyl-3-methylimidazolium acetate (IL-0189-TG/143314-17-4), [C_2mim][OAc] and trimethyl-ethanolammonium acetate, [Ch][OAc]. [C_2mim][C_2SO_4] and [C_2mim][OAc] were supplied by Iolitec (Heilbronn, Germany) with a stated purity of 99 and 95%, respectively. [Ch][OAc] was supplied by Solchemar with a purity of 95%. To reduce the water and other volatile substances contents, vacuum (10 Pa) and moderate temperature (ca. 47°C) were always applied to all samples of ionic liquids for several days prior to their use. After degassing, the purity was checked by ^{1}H NMR. The ^{1}H spectra confirmed purity levels

higher than 99% for [C_2mim][C_2SO_4] and 98% for [C_2mim][OAc] and [Ch][OAc]. The final water mass fraction was measured by Karl Fischer coulometric titration (Metrohm 831 KF Coulometer). The dried samples contained less than 500 ppm of water for all ionic liquids.

2.2. Sample preparation
Samples were prepared according to a procedure optimized by E. Raphael *et al.* [6]. In a glass flask, 0.5 g of agar (W201201, Aldrich, Madrid, Spain) was dispersed in 30 mL of Milli-Q water and heated under magnetic stirring for a few minutes up to 100°C for complete dissolution. Next, 0.5 g of ILs, 0.5 g of glycerol (RM1027-1L, Himedia, Mumbai, India, 99.5%) as plasticizer, 0.5 g of formaldehyde as crosslinking agent (131328, Panreac, Barcelona, Spain, 37–38% wt/wt), were added to this solution under stirring. This solution was then poured on Petri plates, let to dry up for 8–10 days at ambient temperature, to form transparent membranes. The film was transferred to an oven at 60°C, for final drying, and the sample was aged for a period of 1 week resulting in the homogeneous and transparent membranes with thickness of 150 μm as shown in Figure 1.

Figure 1. Physical appearance of a sample, incorporating the [C_2mim][OAc]

2.3. Measurements
2.3.1. Ionic conductivity
The total ionic conductivity of the samples was determined by locating an electrolyte disk between two 10 mm diameter ion-blocking gold electrodes (Goodfellow, >99.95%) to form a symmetrical cell.

The electrode/polymer electrolyte/electrode assembly was secured in a suitable constant volume support and installed in a Büchi TO51 tube oven with a type K thermocouple placed close to the electrolyte disk to measure the sample temperature. Bulk conductivities of the electrolyte samples were obtained during heating cycles using the complex plane impedance technique (Autolab PGSTAT-12 (Eco Chemie)) between 25 and 100°C and at approximately 7°C intervals.

2.3.2. Thermal analysis
The DSC measurements were performed under a flowing nitrogen atmosphere at 30 mL·min^{-1} in the temperature range of –110 to 200°C and at a heating rate of 20°C·min^{-1} using a TA Instruments DSC-Q20 apparatus. The first run was up to 100°C to remove adsorbed water and the second and third runs were performed up to 200°C.

Samples for thermogravimetric studies were prepared in a similar manner, transferred to open crucibles and analyzed using a Rheometric Scientific TG1000 thermobalance operating under flowing argon, between 30 and 700°C and at a heating rate of 10°C·min^{-1}.

2.3.3. Electrochemical stability
The evaluation of the electrochemical stability window of electrolyte compositions was carried out under an argon atmosphere using a two-electrode cell configuration. The preparation of a 25 μm diameter gold microelectrode surface, by polishing it with a moist cloth and 0.05 μm alumina powder (Buehler), was completed outside the drybox. The cell was assembled by locating a clean lithium disk counter electrode (cut from Aldrich, 99.9%, 19 mm diameter, 0.75 mm thick) on a stainless steel current collector and centering a sample of electrolyte on the electrode surface. A small volume (2 μL) of THF was placed on the microelectrode surface. The microelectrode was then located on the electrolyte surface and supported firmly by means of a clamp. The use of THF to soften the electrolyte was necessary to achieve a reproducible microelectrode/electrolyte interfacial contact. An Autolab PGSTAT-12 (Eco Chemie) was used to record voltammograms at scan rate of 30 mV/s. Measurements were performed at room temperature, within a Faraday cage.

2.3.4. X-ray diffraction
The structure of the film was examined on silicon wafer by X-ray Rigaku Utma 4 diffractometer, power of 50 kV/50 mA and CuKα irradiation, speed of 2 °/min, in an angle range (2θ) of 5 to 60°, at room temperature.

2.3.5. SEM
SEM micrographies were obtained with LEO model 440.

2.3.6. FTIR
Infrared spectra were measured by using an ATR-FTIR BOMEM MB 102 spectrophotometer. The films were placed in the holder directly in the IR laser beam. Spectra were recorded in scanning range from 650 to 4000 cm^{-1} at a resolution of 4 cm^{-1} and 16 scans.

2.3.7. Electrochromic cell assembly
Electrochromic devices with the configurations glass/ITO/WO$_3$/electrolyte/CeO$_2$–TiO$_2$/ITO/glass were obtained by assembling the 2 pieces of coated glasses. Electrolytes in the form of hydrated membranes were deposited on glass/ITO/WO$_3$ coatings and 1 cm free space was left for the electrical contact. Then the other coated substrate was pressed onto the membrane in such a way that the two coatings faced each other inside the assembled window. A 1 cm wide Cu-conducting tape (3M) was glued to the free edge of each substrate for electrical connection. The mounted cells were finally sealed with a protective tape (3M).

The electrochemical measurements were performed with Autolab 302N with FRA 2 module.

3. Results and discussion
3.1. FTIR analysis
The infrared spectra of the pure agar membrane and of the membranes containing agar and ionic liquids are shown in Figure 2. In this figure it is observed a significant change in the FTIR spectra with the addition of ionic liquids. The broadband at 3416 cm^{-1}, attributed to the stretching of OH hydroxyl groups of agar that participate in hydrogen bond formation in inter-and intramolecular bonds or in hydrogen inter and intramolecular bond formation, shifts to shorter wavelengths numbers with the addition of
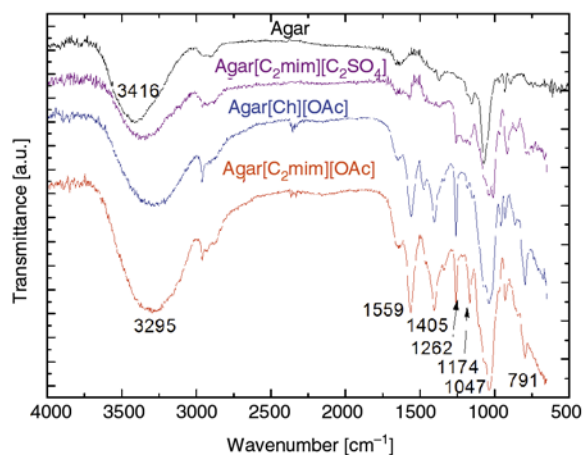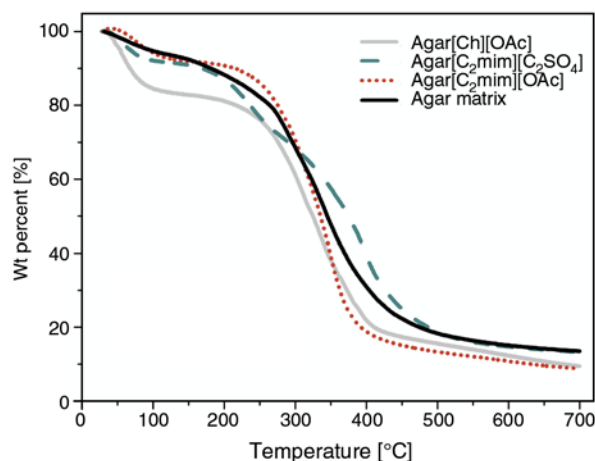
Figure 2. FTIR spectra of agar and agar-based membranes

Figure 3. TGA results for membranes based agar and ionic liquids

ILs [20, 21]. The bands at 2934 and 2887 cm^{-1} refer to the CH asymmetrical stretching, which increase in intensity due to its presence in both glycerol and in the ILs [22, 23]. The band at 2360 cm^{-1} is due to the CO_2 from air and at 1653 cm^{-1} is due to adsorbed water. Samples with ILs present a new band at 1559 cm^{-1}, probably due to C=C imidazolium ring [24] assigned to be at 1562 cm^{-1} [23]. The shift of this band is also an indication of interaction between polysaccharide and IL. The band at 1405 cm^{-1} is assigned to CH bending. The sharp bands at 1262 cm^{-1} in the FTIR spectra of the samples with [Ch][OAc] and [C$_2$mim][OAc] are probably due to C–C stretching in the sample Agar[C$_2$mim][C$_2$SO$_4$] can be due to C–O–SO$_3$ asymmetric stretching. The bands at 1174 cm^{-1} can be assigned to C–O–C from agar as in the case of cellulose dissolved in the 1-butyl-3-methylimidazolium chloride [23] and at 1168 cm^{-1} to ring in-plane assymetric stretching, C–C and (N)CH$_2$ stretching [25]. The stretching of the COH alcohol bond shifts from 1087 to 1038 cm^{-1}, which is probably due to the hydrogen bond formation between glycerol and macromolecule. Other bands from 920 to 960 cm^{-1}, depending on the sample, can be assigned to C–O–SO$_3$ or C–C stretching from polymer ring [26] and at 780; 790 cm^{-1} to IL ring HCCH symmetric bending [22] or 3,6-anhydro-β-galactose skeletal bending [26].

3.2. Thermal behaviour of electrolytes

The onset of thermal decomposition was estimated through thermogravimetric analysis (Figure 3). All samples show a weight loss of 5% for the pure agar membrane, Agar[C$_2$mim][C$_2$SO$_4$], and Agar[C$_2$mim][OAc] and 18% for the sample Agar[Ch][OAc] in

between room temperature and about 100°C, which can be explained as a water loss in the sample. The moisture content (as observed in FTIR spectra and also DSC first run) in the Agar[Ch][OAc] is higher when compared to agar and Agar[C$_2$mim] samples probably due to the hydrophilic properties of the choline ion. In the region of 220–400°C, the film of agar matrix showed a very accentuated mass loss of 65%, which marks the decomposition of the sample, and slowly continues as the temperature is increased up to 700°C. The remaining residue was 15% in mass of the starting material. In the case of the samples with ILs, the loss mass behavior as a function of temperature is different. The degradation process occurs in two stages for the agar based electrolytes with [C$_2$mim][C$_2$SO$_4$], assuming that the negligible initial mass loss observed (<5%) is exclusively associated with the release of solvents, such as water adsorbed or coordinated. For these samples the first stage starts at 200°C for a weight percent of 90% and the second starts at 300°C for a weight percent of 68%. These stages are due to the agaropectin and agarose presence in the samples and the different interactions with ILs. The onset temperature of thermal decomposition was estimated by thermogravimetric analysis using extrapolation of the baseline and tangent of the curve of thermal events to identify the initiation of sample weight loss. The degradation process occurs in one stage for the agar based electrolytes with Agar[C$_2$mim][OAc] and Agar[Ch][OAc], assuming that the negligible initial mass loss observed (<5% for sample Agar[C$_2$mim][OAc] and <20% for Agar[Ch][OAc]) is exclusively associated with the release of solvents,
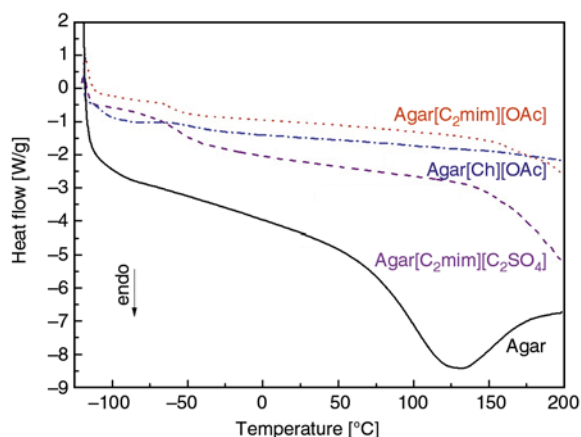
Figure 4. DSC curves obtained for membranes of Agar[C$_2$mim][C$_2$SO$_4$] (– – –), Agar[C$_2$mim][OAc] (· · ·) and Agar[Ch][OAc] (· – · – ·)

such as water adsorved or coordinated. The polymer electrolyte Agar[Ch][OAc] loses more solvents probably because the [Ch][OAc] IL used had more water. The second stage of the samples degradation for a mass loss of 80% starts at 200°C and ends at 550°C and slowly continues at 700°C. The remaining residue was 10% for the samples Agar[C$_2$mim][OAc] and Agar[Ch][OAc].

The DSC results obtained for the materials are illustrated in Figure 4 and in all cases a very accentuated change of the baseline is observed at –58, –60 and –44°C for the samples Agar[C$_2$mim][C$_2$SO$_4$], Agar[C$_2$mim][OAc] and Agar[Ch][OAc], respectively. It was already reported that glass transition in agar samples can be found or observed in the range of temperature between 60 and 130°C depending on the molecular mass and moisture content [27, 28]. However, no linebase changes were observed in the agar matrix used for this study. Therefore, the change of baseline in Figure 4 is probably due to the T_g of glycerol-rich domains [25] or also to glycerol-water [29] or glycerol-agar associations. This last supposition/possibility can be supported by other studies on natural macromolecules gel membranes with glycerol as plasticizer [5]. Above 150°C two samples, Agar[C$_2$mim][C$_2$SO$_4$] and Agar[C$_2$mim][OAc], exhibit a start of an endothermic peak, attributed to the start of the degradation of the sample, as observed by TGA measurements. No endothermic peak up to 200°C is observed for the sample Agar[Ch][OAc]. The obtained results confirm that all the polymer electrolytes produced have predominantly amorphous nature.

3.3. Structure and morphology

Figure 5 shows the typical X-ray diffraction patterns obtained for the sample Agar[C$_2$mim][C$_2$SO$_4$] measured at room temperature. The diffractogram of agar matrix (not shown here) revealed an ordered structure due to the presence of a very accentuated peak at 18.6° 2θ and a slight shoulder at 14.3° 2θ, similarly to the results of 19.9 and 13.83°, respectively, reported for pristine agar films [30]. The deconvolution of the diffraction profile (Figure 5) in different Gaussian lines reveals very broad components on the fully disordered part of the sample and the three narrower bands are attributed to the ordered regions. From the deconvoluted plot, the degree of crystallinity of this sample is found to be about 25%. Moreover, through the SEM pictures one can observe the homogeneity without any phase separation and good surface uniformity of agar-based electrolyte with ionic liquid samples (Figure 6). Agar-ILs-based SPE samples were translu-
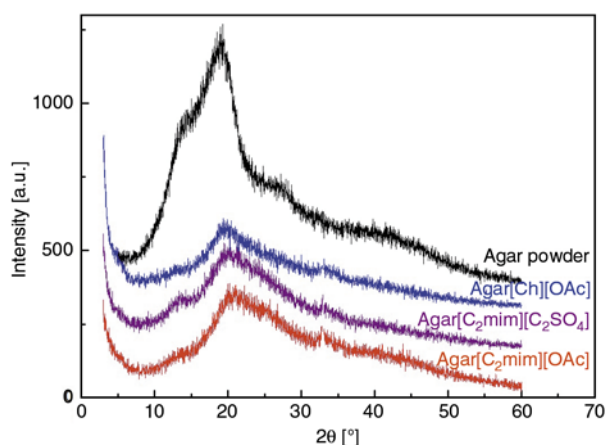
Figure 5. X-ray diffractogram for agar matrix and agar-based membranes on glass XDR support
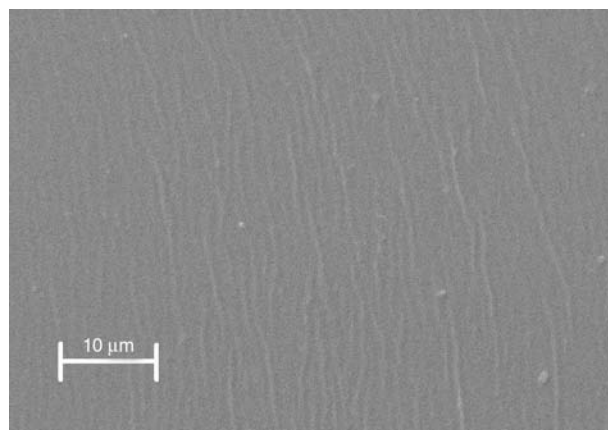
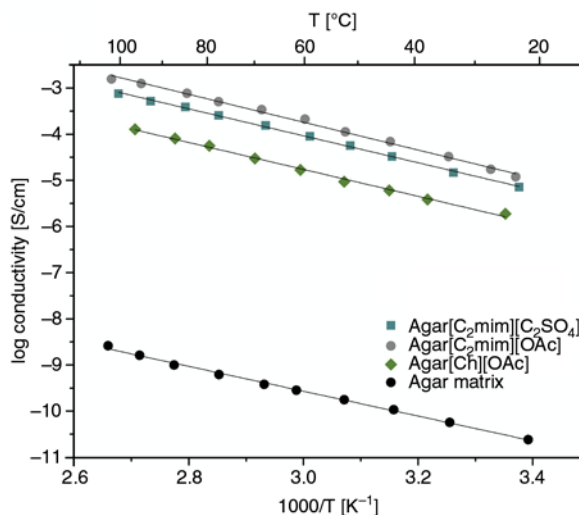**Figure 6.** SEM picture of the sample, incorporating the [C$_2$mim][C$_2$SO$_4$]
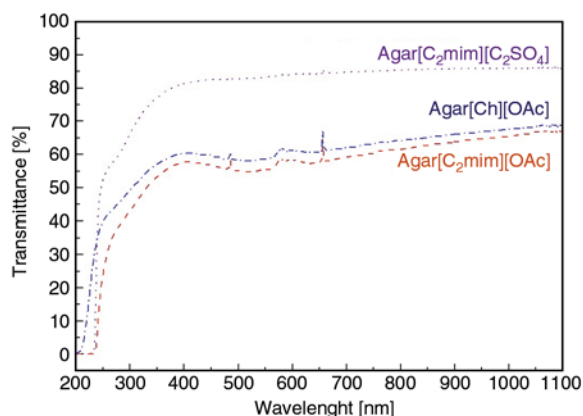
Figure 7. Optical transmittance measurement for membranes of Agar[C_2mim][C_2SO_4] (– – –), Agar[C_2mim][OAc] (· · ·) and Agar[Ch][OAc] (· – · – ·)

Figure 8. Variation of ionic conductivity with $1/T$ for selected electrolyte

cent (Figure 1) and showed very good adhesion properties to glass and steel.

Figure 7 shows the optical transmittance of a 0.52, 0.12 and 0.46 mm thick layer of the Agar[C_2mim][C_2SO_4], Agar[C_2mim][OAc] and Agar[Ch][OAc] electrolytes as well as almost zero transmission intensity below 230 nm, which starts to increase until reaching 81, 57 and 60% at 400 nm, respectively. For the 400 to 1100 nm wavelength interval the transmission is practically constant increasing only few percent. From the obtained results it is possible to observe that ILs with acetate ion promote a decrease of the transparency similar to a previous study [31, 32].

3.4. Ionic conductivity of electrolytes

The ionic conductivities of various polymer electrolytes over the temperature range from 25 to 105°C and as a function of different ionic liquids are illustrated in Figure 8. From this figure we can observe that all samples exhibit a linear variation of log conductivity with reciprocal temperature, which is typical of polymer electrolytes where hopping mechanism of ionic charge species is predominant. From this figure it is also possible to observe that the addition of any ILs studied, produces an increase of ionic conductivity values, when compared to the matrix. The highest room temperature ($T = 30$°C) conductivity of the electrolyte system is $2.35 \cdot 10^{-5}$ S·cm^{-1}, registered for the agar based on 1-ethyl-3-methylimidazolium acetate composition. At 100°C, this electrolyte exhibits a conductivity of about $1.58 \cdot 10^{-3}$ S·cm^{-1}. The small differences in the conductivity values as a function of temperature of

the samples with ILs may be due to the type of ILs, its dielectric constant, viscosity, interaction with the host polymer and molecular weight [33]. The temperature dependence of the ionic conductivity values shows an Arrhenius behavior, where the ionic transport is promoted by the hopping of ionic species. In this, the ILs probably promotes a better separation of polymeric chains and, consequently, its more pronounced movements.

The fitted value of the E_a for the electrolyte based on 1-ethyl-3-methylimidazolium acetate is 24.27 K·J·mol^{-1}. This is smaller than those reported by Raphael *et al.* [6] for agar-acetic acid-based electrolytes or other natural macromolecules [31, 32, 34]. The E_a values decrease with the addition of ILs and this is in agreement with the fact that the amount of ions in polymer electrolyte increases, and the energy barrier to the ion transport decreases, leading to a decrease in the activation energy.

3.5. Electrochemical stability

Cyclic voltammetry was employed to evaluate the chemical and electrochemical stability of the solid polymer electrolytes. In the cyclic voltammetric analysis the sweep potential was firstly scanned in the positively going direction and then the reversed direction. The addition of ionic liquid doesn't deplete the electrochemical stability of the electrolytes. A very low current flow was observed up to the anodic breakdown voltage, thus supporting the high purity of the RTIL-based polymer electrolytes.
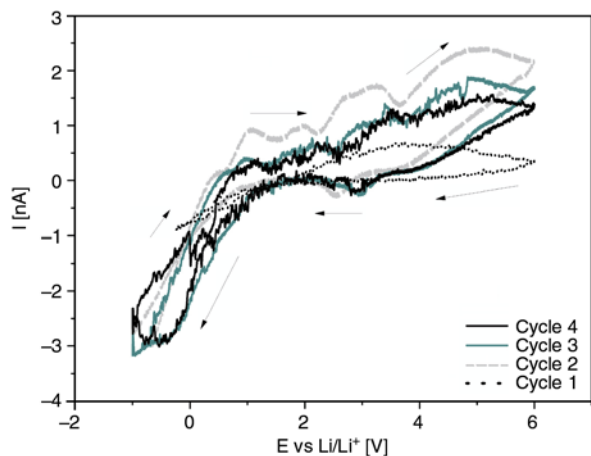
Figure 9. Voltammogram of the Agar[C$_2$mim][C$_2$SO$_4$] sample at a 25 μm diameter gold microelectrode versus Li/Li$^+$. Initial sweep direction is anodic and different sweep rate.

The electrochemical stabilities of the polymer electrolytes based on ILs (Figure 9) were determined by microelectrode cyclic voltammetry over the potential ranging from –2.0 to 6.0 V at scan rate 30 mV·s^{-1} and at ambient temperature. The anodic current onset may be associated with the decomposition of the polymer electrolyte. The voltammetric stability of the electrolytes containing ILs was checked by the repetitive potential sweep at a scan rate of 30 mV·s^{-1}. The results are shown in Figure 9. The peak currents decrease with the increase of the scan numbers, which may be due to the detach of the samples from the electrode surface.

It is noted that a small reduction peak around 1.5–2.0 V appeared for the electrolytes films based on [C$_2$mim][C$_2$SO$_4$] (Figure 9). Previously, the peak in this region had been ascribed to the reduction of low level of water present in IL or oxygen impurities. These measurements are made in glove box and probably oxygen impurities are not present. Similar behavior has been observed for other systems based on PEO, lithium salt and IL [35].

As can be seen, all the electrolytes show good stability of 2.0 V windows versus Li/Li$^+$. They display a wide electrochemical window (–2.0 to + 2.0 V) over which the polymer electrolytes based on ILs can be used safely without decomposition. A large electrochemical window is a valuable property for the fabrication of stable and durable electrochemical devices.

3.6. Electrochromic device

A preliminary evaluation of the performance of the agar based materials as electrolytes in all solid-state ECDs was carried out using the five layer-sandwich configuration.

Typical cyclic voltammograms of an ECD containing Agar[C$_2$mim][C$_2$SO$_4$] measured during the 10th, 50th, 100th, 150th and 200th chronoamperometric cycles are shown in Figure 10. One cathodic peak centered at –1.3 V is observed and is accompanied by the coloring of the device while the other, centered around –0.3 V, is anodic and is accompanied by the bleaching of the device. The feature of the voltammograms doesn't changes during 200 cycles, however a small shift to more positive potentials is observed.

The charge density responses measured by chronoamperometry (–2 V/+1.8 V; 15 s/15 s) of ECD containing solid electrolyte based on agar and ILs for the cycle 10th, 50th , 100th, 150th and 200th are shown in Figure 11. From these measurements, it can be stated that the insertion (coloration) is fast. For instance, for the 10th cycle, the inserted charge at –2 V reaches –0.76 mC·cm^{-2} in 15 s. The consecutive chronoamperometric cycling promotes a decrease of the inserted charge values reaching –0.4 mC·cm^{-2} for the 200 cycles. The reverse potential, i.e., +1.8 V promotes an extraction and consequent bleaching of the device. This phenomenon occurs faster than coloring and after 2 s the ECD is already transparent. However, as can be observed from this experiment for the initial cycles extracted charge value is lower when compared with the inserted one, indicating
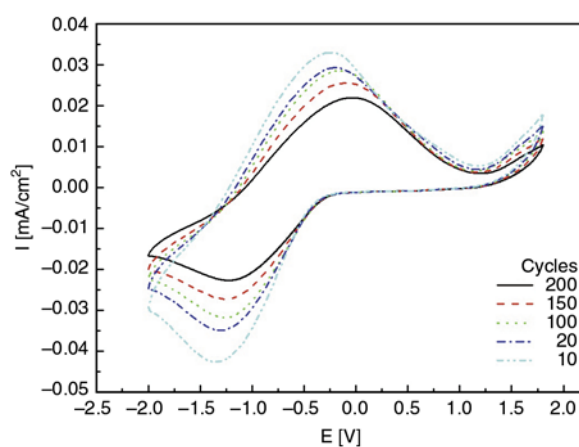
Figure 10. Cyclic voltammetries of electrochromic window with WO$_3$/Agar[C$_2$mim][C$_2$SO$_4$]/CeO$_2$–TiO$_2$ configuration
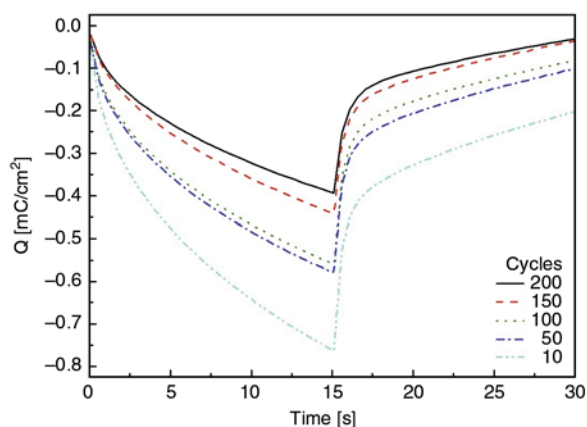
Figure 11. Charges densities for ECDs electrochromic window with WO_3/Agar$[C_2mim][C_2SO_4]$/CeO_2–TiO_2 configuration of 10th to 200th cycles

that some part of the charge remains in the electrochromic coating and is probably responsible for the not complete reversibility of the device. As a consequence a successive decrease of the inserted charge density as a function of number of cycles is observed.

The UV-vis transmission spectra of the electrochromic device in the range from 200 to 1100 nm for the 200th cycle are measured (not shown). A transmittance variation of 13% between the bleached (63% of transmittance) and colored states (50% of transmittance) occurs in the visible range of the spectra with a maximum at 550 nm. This result is comparable to the results obtained with electrochromic devices containing ormolytes-based electrolytes with potassium salt [36]. The promising tests performed in the present work based on ILs support the idea that these materials may find application in polymer science, like others [37].

4. Conclusions

Polymer electrolytes based on agar and containing ILs were prepared and characterized. The obtained results revealed that the ILs influence the ionic conductivity of electrolytes and the best values of $2.35 \cdot 10^{-5}$ S·cm^{-1} were registered for the agar based on 1-ethyl-3-methylimidazolium acetate composition at ambient temperature. At 100°C, this electrolyte exhibits a conductivity of about $1.58 \cdot 10^{-3}$ S·cm^{-1}. These results show a Arrhenius behavior with an activation energy of $E_a =$ 24.27 kJ/mol.

In ECDs very specific conditions must be fulfilled by the electrolyte component. These include high

transparency to maximize chromatic contrast in the case of see-through displays, adequate room temperature conductivity to permit rapid color response, mechanical flexibility to form an appropriate electrode/electrolyte interface and low thermal expansion or component volatility so that the device may operate over a wide range of temperatures. The samples applied in small electrochromic devices evidenced the reversible insertion/extraction process during 200 chronoamperometric cycles. The inserted charge was –0.40 mC·cm^{-2} during 15 s and the extraction occurred in 2 s.

The encouraging results of the thermal (DSC and TGA), electrochemical (ionic conductivity and CV), and structural (XRD) investigation of a novel series of agar – ILs membranes are sufficient to justify further studies. The preliminary tests performed in this study using prototype ECDs suggest that these materials may find application in 'smart windows' devices, as well as other electrochromic displays.

References

[1] Armand M. B., Chabagno J. M., Duclot M. T.: Polymeric solid electrolytes. in 'Proceeding of the Second International Meeting on Solid State Electrolytes, St. Andrews, Scotland' 6.5.1. (1978).

[2] Gray F. M.: Solid polymer electrolytes: Fundamentals and technological applications. VCH, New York (1991).

[3] Pawlicka A., Danczuk M., Wieczorek W., Zygadlo-Monikowska E.: Influence of plasticizer type on the properties of polymer electrolytes based on chitosan. Journal of Physical Chemistry A, **112**, 8888–8895 (2008).
DOI: 10.1021/jp801573h

[4] Avellaneda C. O., Vieira D. F., Al-Kahlout A., Leite E. R., Pawlicka A., Aegerter M. A.: Solid-state electrochromic devices with Nb_2O_5:Mo thin film and gelatin-based electrolyte. Electrochimica Acta, **53**, 1648–1654 (2007).
DOI: 10.1016/j.electacta.2007.05.065

[5] Machado G. O., Ferreira H. C. A., Pawlicka A.: Influence of plasticizer contents on the properties of HEC-based solid polymeric electrolytes. Electrochimica Acta, **50**, 3827–3831 (2005).
DOI: 10.1016/j.electacta.2005.02.041

[6] Raphael E., Avellaneda C. O., Manzolli B., Pawlicka A.: Agar-based films for application as polymer electrolytes. Electrochimica Acta, **55**, 1455–1459 (2010).
DOI: 10.1016/j.electacta.2009.06.010

[7] Florjanczyk Z., Debowski M., Chwojnowska E., Lokaj K., Ostrowska J.: Synthetic and natural polymers in modern polymeric materials. Part I. Polymers from renewable resources and polymer nanocomposites. Polimery, **54**, 691–705 (2009).

[8] Aimé C., Coradin T.: Nanocomposites from biopolymer hydrogels: Blueprints for white biotechnology and green materials chemistry. Journal of Polymer Science Part B: Polymer Physics, **50**, 669–680 (2012).
DOI: 10.1002/polb.23061

[9] Legnani C., Vilani C., Calil V. L., Barud H. S., Quirino W. G., Achete C. A., Ribeiro S. J. L., Cremona M.: Bacterial cellulose membrane as flexible substrate for organic light emitting devices. Thin Solid Films, **517**, 1016–1020 (2008).
DOI: 10.1016/j.tsf.2008.06.011

[10] Nogi M., Yano H.: Transparent nanocomposites based on cellulose produced by bacteria offer potential innovation in the electronics device industry. Advanced Materials, **20**, 1849–1852 (2008).
DOI: 10.1002/adma.200702559

[11] Ohno H.: Electrochemical aspects of ionic liquids. Wiley, USA (2005).

[12] Thayumanasundaram S., Piga M., Lavina S., Negro E., Jeyapandian M., Ghassemzadeh L., Müller K., Di Noto V.: Hybrid inorganic–organic proton conducting membranes based on Nafion, SiO_2 and triethylammonium trifluoromethanesulfonate ionic liquid. Electrochimica Acta, **55**, 1355–1365 (2010).
DOI: 10.1016/j.electacta.2009.05.079

[13] Cheng H., Zhu C., Huang B., Lu M., Yang Y.: Synthesis and electrochemical characterization of PEO-based polymer electrolytes with room temperature ionic liquids. Electrochimica Acta, **52**, 5789–5794 (2007).
DOI: 10.1016/j.electacta.2007.02.062

[14] Ohno H., Yoshizawa M., Ogihara W.: Development of new class of ion conductive polymers based on ionic liquids. Electrochimica Acta, **50**, 255–261 (2004).
DOI: 10.1016/j.electacta.2004.01.091

[15] Kim G. T., Appetecchi G. B., Carewska M., Joost M., Balducci A., Winter M., Passerini S.: UV cross-linked, lithium-conducting ternary polymer electrolytes containing ionic liquids. Journal of Power Sources, **195**, 6130–6137 (2010).
DOI: 10.1016/j.jpowsour.2009.10.079

[16] Kim J-K., Manuel J., Chauhan G. S., Ahn J-H., Ryu H-S.: Ionic liquid-based gel polymer electrolyte for $LiMn_{0.4}Fe_{0.6}PO_4$ cathode prepared by electrospinning technique. Electrochimica Acta, **55**, 1366–1372 (2010).
DOI: 10.1016/j.electacta.2009.05.043

[17] Earle M. J., Esperança J. M. S. S., Gilea M. A., Lopes J. N. C., Rebelo L. P. N., Magee J. W., Seddon K. R., Widegren J. A.: The distillation and volatility of ionic liquids. Nature, **439**, 831–834 (2006).
DOI: 10.1038/nature04451

[18] Smiglak M., Reichert W. M., Holbrey J. D., Wilkes J. S., Sun L., Thrasher J. S., Kirichenko K., Singh S., Katritzky A. R., Rogers R. D.: Combustible ionic liquids by design: Is laboratory safety another ionic liquid myth? Chemical Communications, **24**, 2554–2556 (2006).
DOI: 10.1039/B602086K

[19] Baranyai K. J., Deacon G. B., MacFarlane D. R., Pringle J. M., Scott J. L.: Thermal degradation of ionic liquids at elevated temperatures. Australian Journal of Chemistry, **57**, 145–147 (2004).
DOI: 10.1071/CH03221

[20] Takano R., Yoshikawa S., Ueda T., Hayashi K., Hirase S., Hara S.: Sulfation of polysaccharides with sulfuric acid mediated by dicyclohexylcarbodiimide. Journal of Carbohydrate Chemsitry, **15**, 449–457 (1996).
DOI: 10.1080/07328309608005665

[21] Xing D. Y., Peng N., Chung T-S.: Investigation of unique interactions between cellulose acetate and ionic liquid [EMIM]SCN, and their influences on hollow fiber ultrafiltration membranes. Journal of Membrane Science, **380**, 87–97 (2011).
DOI: 10.1016/j.memsci.2011.06.032

[22] Kiefer J., Fries J., Leipertz A.: Experimental vibrational study of imidazolium-based ionic liquids: Raman and infrared spectra of 1-ethyl-3-methylimidazolium bis(trifluoromethylsulfonyl)imide and 1-ethyl-3-methylimidazolium ethylsulfate. Applied Spectroscopy, **61**, 1306–1311 (2007).
DOI: 10.1366/000370207783292000

[23] Vitz J., Erdmenger T., Haensch C., Schubert U. S.: Extended dissolution studies of cellulose in imidazolium based ionic liquids. Green Chemistry, **11**, 417–424 (2009).
DOI: 10.1039/B818061J

[24] Sadlej J., Jaworski A., Miaskiewicz K.: A theoretical study of the vibrational spectra of imidazole and its different forms. Journal of Molecular Structure, **274**, 247–257 (1992).
DOI: 10.1016/0022-2860(92)80161-A

[25] Anglès M. N., Dufresne A.: Plasticized starch/tunicin whiskers nanocomposites. 1. Structural analysis. Macromolecules, **33**, 8344–8353 (2000).
DOI: 10.1021/ma0008701

[26] Prasad K., Mehta G., Meena R., Siddhanta A. K.: Hydrogel-forming agar-*graft*-PVP and κ-carrageenan-*graft*-PVP blends: Rapid synthesis and characterization. Journal of Applied Polymer Science, **102**, 3654–3663 (2006).
DOI: 10.1002/app.24145

[27] Robitzer M., Tourrette A., Horga R., Valentin R., Boissière M., Devoisselle J. M., Di Renzo F., Quignard F.: Nitrogen sorption as a tool for the characterisation of polysaccharide aerogels. Carbohydrate Polymers, **85**, 44–53 (2011).
DOI: 10.1016/j.carbpol.2011.01.040

[28] Mitsuiki M., Mizuno A., Motoki M.: Determination of molecular weight of agars and effect of the molecular weight on the glass transition. Journal of Agricultural and Food Chemistry, **47**, 473–478 (1999).
DOI: 10.1021/jf980713p

[29] Li D-X., Liu B-L., Liu Y-S., Chen C-L.: Predict the glass transition temperature of glycerol–water binary cryoprotectant by molecular dynamic simulation. Cryobiology, **56**, 114–119 (2008).
DOI: 10.1016/j.cryobiol.2007.11.003

[30] Freile-Pelegrín Y., Madera-Santana T., Robledo D., Veleva L., Quintana P., Azamar J. A.: Degradation of agar films in a humid tropical climate: Thermal, mechanical, morphological and structural changes. Polymer Degradation and Stability, **92**, 244–252 (2007).
DOI: 10.1016/j.polymdegradstab.2006.11.005

[31] Vieira D. F., Avellaneda C. O., Pawlicka A.: A.C Impedance, X-Ray diffraction and DSC investigation on gelatin based-electrolyte with LiClO$_4$. Molecular Crystals and Liquid Crystals, **506**, 178 (2009).
DOI: 10.1080/15421400903162486

[32] Raphael E., Avellaneda C. O., Aegerter M. A., Silva M. M., Pawlicka A.: Agar-based gel electrolyte for electrochromic device application. Molecular Crystals and Liquid Crystals, **554**, 264–272 (2012).
DOI: 10.1080/15421406.2012.634349

[33] Shaplov A. S., Lozinskaya E. I., Ponkratov D. O., Malyshkina I. A., Vidal F., Aubert P. H., Okatova O. V., Pavlov G. M., Komarova L. I., Wandrey C., Vygodskii Y. S.: Bis(trifluoromethylsulfonyl)amide based 'polymeric ionic liquids': Synthesis, purification and peculiarities of structure–properties relationships. Electrochimica Acta, **57**, 74–90 (2011).
DOI: 10.1016/j.electacta.2011.06.041

[34] Marcondes R. F. M. S., D'Agostini P. S., Ferreira J., Girotto E. M., Pawlicka A., Dragunski D. C.: Amylopectin-rich starch plasticized with glycerol for polymer electrolyte application. Solid State Ionics, **181**, 586–591 (2010).
DOI: 10.1016/j.ssi.2010.03.016

[35] Aurbach D., Daroux M., Faguy P., Yeager E.: The electrochemistry of noble metal electrodes in aprotic organic solvents containing lithium salts. Journal of Electroanalytical Chemistry and Interfacial Electrochemistry, **297**, 225–244 (1991).
DOI: 10.1016/0022-0728(91)85370-5

[36] Nunes S. C., de Zea Bermudez V., Silva M. M., Smith M. J., Ostrovskii D., Sá Ferreira R. A., Carlos L. D., Rocha J., Gonçalves A., Fortunato E.: Sol–gel-derived potassium-based di-ureasils for 'smart windows'. Journal of Materials Chemistry, **17**, 4239–4248 (2007).
DOI: 10.1039/B708905H

[37] Lu J., Yan F., Texter J.: Advanced applications of ionic liquids in polymer science. Progress in Polymer Science, **34**, 431–448 (2009).
DOI: 10.1016/j.progpolymsci.2008.12.001

Enhancement of dispersion and bonding of graphene-polymer through wet transfer of functionalized graphene oxide

M. Moazzami Gudarzi, F. Sharif[*]*

Department of Polymer Engineering and Color Technology, Amirkabir University of Technology, Tehran, Iran

Abstract. Dispersion of nanomaterials in polymeric matrices plays an important role in determining the final properties of the composites. Dispersion in nano scale, and especially in single layers, provides best opportunity for bonding. In this study, we propose that by proper functionalization and mixing strategy of graphene its dispersion, and bonding to the polymeric matrix can be improved. We then apply this strategy to graphene-epoxy system by amino functionalization of graphene oxide (GO). The process included two phase extraction, and resulted in better dispersion and higher loading of graphene in epoxy matrix. Rheological evaluation of different graphene-epoxy dispersions showed a rheological percolation threshold of 0.2 vol% which is an indication of highly dispersed nanosheets. Observation of the samples by optical microscopy, scanning electron microscopy (SEM), and atomic force microscopy (AFM), showed dispersion homogeneity of the sheets at micro and nano scales. Study of graphene-epoxy composites showed good bonding between graphene and epoxy. Mechanical properties of the samples were consistent with theoretical predictions for ideal composites indicating molecular level dispersion and good bonding between nanosheets and epoxy matrix.

Keywords: nanocomposites, graphene, epoxy, functionalization, rheology

1. Introduction

Carbon nanomaterials have emerged as a rising star in the material science community, during the past two decades [1–3]. Exceptional physical and mechanical properties of carbon nanomaterials can be incorporated into polymers resulting in composite materials with improved properties [4, 5]. Hybridization of carbon nanomaterials and polymers has led to the production of composites with enhanced electrical and mechanical properties for new applications such as solar cells [6], electromagnetic interference shielding [7], and sensors [8].

Due to the high surface area, nanofillers tend to agglomerate and stick to each other, forming micro particles [9, 10]. Therefore, dispersion of nanofiller into individual particles throughout the matrix, especially molecular level dispersion, is an essential step [10]. Agglomeration is even more severe for anisotropic nanoparticles such as nanotubes and nanosheets due to the high interparticle interaction. Emerging graphene and its derivatives as fillers for polymeric materials has led to the production of a new class of nanocomposites [5, 11]. Remarkable improvements in physical and mechanical properties of polymer have been reported upon addition of a small amount of graphene [11, 12]. Similar to other layered nanofillers, graphene sheets are prone to restacking due to the high aspect ratio and strong interparticle interaction [11]. Although, chemically derived graphene is available as single layer dispersion in liquids, retaining the single layer state of graphene in polymer media is not easy [11–13].

Chemically derived graphene is commonly produced by oxidizing graphite to graphite oxide with a layered hydrophilic structure, which is then exfoliated into the graphene oxide (GO) in aqueous media or polar solvents, possibly by mechanical shearing [14, 15]. Because of the hydrophilic nature of GO, it is not easily dispersed in weakly polar organic solvents, and polymers [16]. Reduction of GO usually results in serve aggregation of reduced GO (rGO) [11].

Many attempts have been made to disperse chemically derived graphene in low polarity organic media by functionalization of GO. However; employing aqueous dispersion of GO to fabricate graphene-based composite is more attractive, since it can be easily combined with water soluble polymers and then reduced to rGO [17] without using organic solvents or chemical functionalization which can be toxic and/or costly [18–20].

Furthermore, colloidal polymer particles may be mixed with GO to incorporate graphene into non-water soluble polymers [21–24]. Our recent study also shows GO can be employed as a surfactant in emulsion polymerization to produce polymer-graphene nanocomposites [25]. Therefore it is a practical and environmentally friendly strategy, to use aqueous dispersion of GO to produce polymer graphene and GO composites.

In this paper we have used the case of epoxy-functionalized GO to address the challenges of well dispersing graphenic sheets in a thermoset resin and show the success of the proposed strategy. Fabrication of epoxy composites with grapheme, GO, and functionalized graphene is mostly performed through [26–31]:

i) Dispersion of graphene (obtained via different chemical pathways including thermal expansion of graphite oxide) in organic solvents such as acetone [27, 31]

ii) Multi-step chemical functionalization of graphene (oxide) and then removing solvent from the mixture of epoxy and graphene [28].

Direct mixing of graphenic powder in viscous epoxy resin usually results in poor dispersion. It should be noted that even ultrasonication of graphenic sheets in organic solvent for a long period of time does not guarantee a good dispersion especially for higher graphenic contents [28]. On the other hand, GO sheets easily restack during drying, and form a layered material consisting of GO sheets that are strongly bonded together by hydrogen bonding [32]. To ensure well dispersion of GO in polymer, restacking of the graphenic sheets must be avoided.

Recently, Li and coworkers [33, 34] uncovered that in 'wet' graphenic sheets, water acts as 'spacer' keeping the nanosheets separated. Therefore, wet transfer of GO into organic phase, *i.e.* epoxy resin, can prevent restacking and agglomeration of nanolayers [33–35].

In addition to good dispersion, we need to ensure good GO-matrix bonding, to obtain superior mechanical properties [28, 36]. In the next section we describe a novel and single-step method to functionalize and disperse GO nanosheets in epoxy and obtain high performance nanocomposites by achieving a high degree of dispersion and good bonding to the matrix.

Although graphite oxide has been synthesised long ago, its exact molecular structure is not well known [17–19, 37]. However, presence of epoxy and carboxyl groups has been confirmed [16]. Presence of epoxy groups is valuable as they facilitate the GO functionalization, compared to other groups such as the carboxyl group which needs activation in the absence of water [16]. Strong nucleophilic agents such as amines can readily react with the epoxy group through a ring opening reaction without any activation. Therefore, amines have extensively been employed for the functionalization of GO [16]. The reaction is carried out in aqueous media and ambient atmosphere without catalyst. The reaction is relatively fast, due to the high reactivity of amine and epoxy groups.

Amino functionalization of carbon nanotubes (CNTs) has been extensively used to improve interfacial interaction with epoxy matrices [38–40]. In analogy to CNTs, covalent bond formation between amino functionalized GO surface and epoxy resin is anticipated [41, 42].

The method serves two simultaneous purposes of accommodating graphenic sheets at the molecular level and furnishing the interfacial bonding with the matrix which are highly desirable. Higher dispersion means higher area per volume and better bonding means efficient use of filler presence in the matrix to improve mechanical properties. Direct impact of higher quality dispersion and interfacial bonding on the mechanical properties are shown to approach theoretical predictions for ideal composites.

2. Experimentals
2.1. Materials
Natural graphite flake (< 50 μm) was purchased from Merck Chemicals, Germany. Epoxy resin (diglycidyl ether of bisphenol A, Epon828) was obtained from Shell, USA. Isophoronediamine (IPDA) from Fluka, USA was used as hardener. All other reagents were purchased from Merck Chemicals, Germany and used as received.

2.2. Functionalization of GO
Graphite oxide was synthesized from natural graphite flakes using Hummers' method [20, 37]. Homogeneous dispersion of GO was obtained by sonication of the graphite oxide suspension in water for an hour and centrifuging for 10 minutes at 4000 rpm. An aromatic diamine (PPDA) was used to functionalize GO sheets to increase compatibility of GO sheets with epoxy resin, although other diamines (aliphatic or aromatic) can be used for amino-functionalization of GO through the same mixing strategy (wet transfer). The excess amount of diamine was used to ensure that at least one of the amine groups has reacted with epoxy groups on GO and have amine groups on the surface of GO. In order to functionalize GO sheets, p-Phenylenediamine (PPDA) was dissolved in hot water and mixed with GO suspension (2.5 mg/mL), resulting in a GO/PPDA mass ratio of 1 to 5. The mixture was then heated to 80°C for 30 minutes to complete the reaction. The result was a dark violet precipitation which was washed several times with water to remove the excess PPDA.

2.3. Preparation of nanocomposites
The functionalized GO (fGO) slurry was mixed with epoxy resin. The mixture was sonicated with a tip sonicator for 5 minutes transferring the fGO particles from water to epoxy. The water was then removed by decanting and heating at 100°C for 48 hours resulting in a dark violet epoxy-fGO.The mixture was further sonicated for 5 minutes.
The stochiometric amount of hardener (IPDA) was added to cure the resin at room temperature for 24 hr and then post-cured at 100°C for 2 hours. Volume fractions of fGO in final composites were calculated considering the density of epoxy and graphenic sheets 1.16 and 2.2 g/cm^3; respectively.

2.4. Characterization
Scanning electron microscope (SEM, LEO 1455VP, USA) was used to evaluate the morphology of graphite, graphite oxide, GO and fractured surface of the composites. A thin layer of platinum was coated on the samples to avoid electron charging.
X-ray diffraction experiments were performed at ambient temperature to study crystalline structure of materials, using an X-ray diffraction system (Philips X'Pert, Neitherland) employing CuK$_\alpha$ radiation (X-ray wavelength $\lambda = 1.5406$ Å) under normal laboratory conditions.
Optical micrographs of dispersions on a transparent glass slide were taken using Leica DMR microscope, USA.
Fourier transform infrared spectroscopy (FTIR, Perkin-Elmer Spectrum One, USA) was employed to study functionalization. GO and fGO powder were molded into discs using KBr.
X-ray photoelectronic spectroscopy (XPS) was utilized to evaluate the chemical structure of the GO and fGO. The measurements were carried out by a Gammadata-scienta ESCA 200 hemispherical analyzer equipped with a monochromatic Al K$_\alpha$ X-ray source (X-ray wavelength $\lambda = 8.34$ Å; $h\upsilon = 1486.6$ eV), USA.
Rheological measurements were conducted in an oscillatory mode on a rheometer (Anton Paar, MCR300, Austria) equipped with parallel plate geometry. Dynamic viscoelastic material functions of the epoxy-fGO mixtures were measured as a function of frequency for small strains at room temperature. The frequency sweeps were run using strain values in the linear viscoelastic region at angular frequencies (ω) of 0.1–100 s^{-1}.
AFM pictures were taken on Dualscope DS 95-200, DME, Denmark. Samples for AFM were prepared by spin coating (2000 rpm) of aqueous dispersions of GO on a freshly cleaved mica surface. In addition, fractured surface topography of epoxy and nanocomposites was evaluated by AFM.
A three-point flexural test was used to evaluate the mechanical properties of composites. Samples were molded into 12.7 mm wide ×70 mm long ×3 mm thick, using silicone mold. The samples were then subjected to bending by a support span of 50 mm at a constant cross-head speed of 1 mm/min on universal testing machine Galdabini Sun 2500, Italy. Five specimens were tested for each set of conditions.
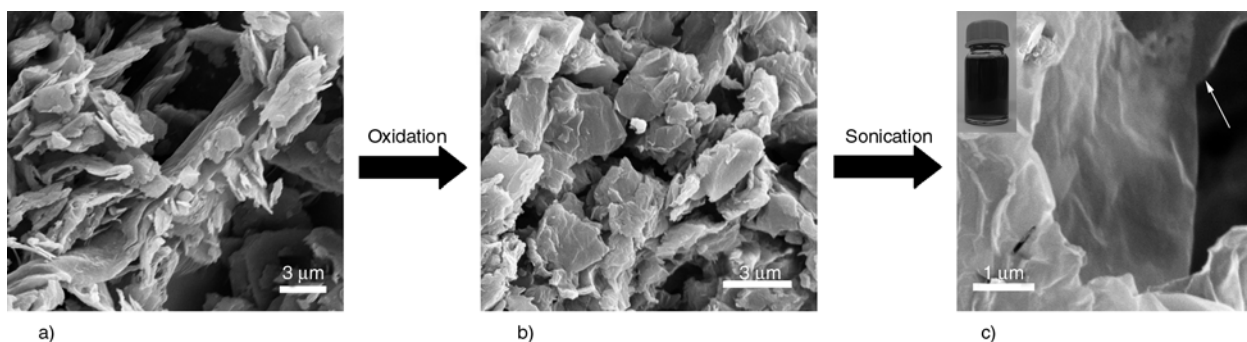
Figure 1. SEM images of (a) graphite flakes (b) graphite oxide (c) GO

3. Results and discussion
3.1. Study of GO morphology
A natural graphite flake is composed of thousands of graphene layers firmly stacked on each other. Strong oxidization of graphite converts it to a hydrophilic layered compound, *i.e.* graphite oxide [16]. Morphologies of graphite and graphite oxide, are shown in Figure 1a and 1b. Graphite flakes with few micrometers lateral size and sub-micron thickness can be observed. On the other hand, an image of graphite oxide, shows a large increase in the thickness of graphite flakes during oxidization, whereas the lateral size of flakes shows marginal decrease, which is in agreement with recent mechanism proposed by Pan and Aksay [16] that small graphite flakes are less prone to lateral cleavage. (Figure 1b). Such remarkable increase in the thickness of graphite flakes during the oxidization stems from formation of oxygen groups in the basal plane of graphite [14, 16]. In addition, the presence of oxygen groups in the structure of graphite oxide facilitates intercalation of water molecules into graphite oxide interlayer. Therefore exfoliation of

graphite oxide is not only due to the hydrophilization of graphene layers, but also because of substantial decrease in the interlayer interaction, caused by intense intercalation of the graphite oxide.

XRD was also employed to evaluate effects of oxidization on the interlayer distance of graphite. Figure 2 depicts XRD patterns of graphite and graphite oxide showing diffraction peaks at 26.58 and 11.6° for graphite and graphite oxide; respectively. This indicates intense intercalation of graphite during oxidization. Increase of d-spacing from 3.35 to
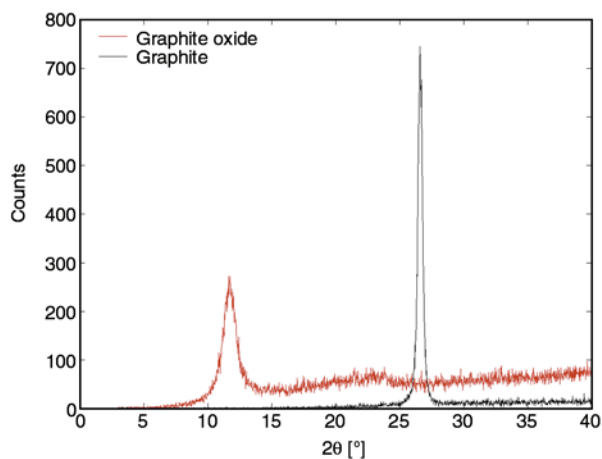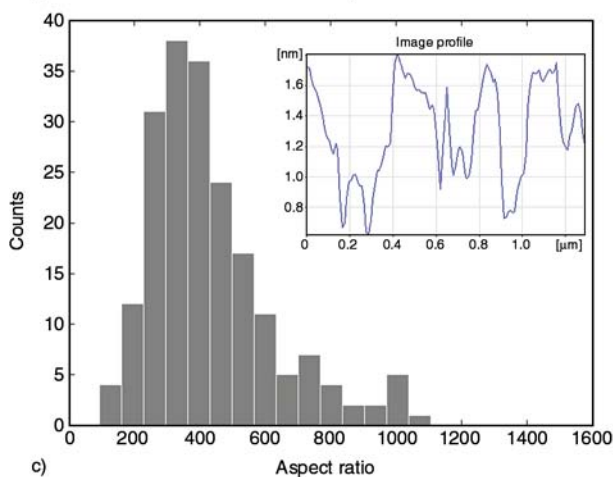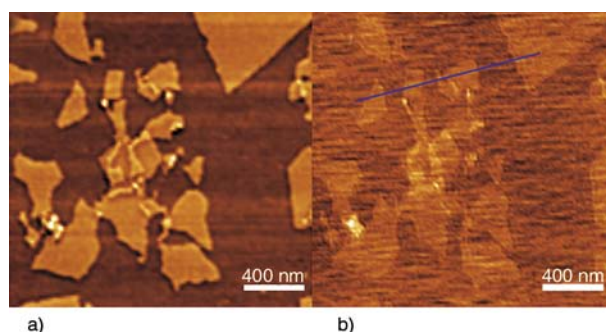

Figure 3. AFM (a) phase and (b) topograph images of graphene oxide spin coated on a mica substrate from GO dispersion in water. (c) Histogram of GO sheets aspect ratio obtained from AFM images analysis.

**Figure 2.** XRD patterns of graphite flakes and graphite oxide

7.63 Å is a typical increase in the interlayer distance for oxidization of graphite [16].

Ultrasonication of aqueous slurry of graphite oxide was used to exfoliate graphite oxide flakes into GO. Exfoliation of aqueous dispersion of graphite oxide resulted in GO dispersion which was stable for months. Figure 1c shows SEM micrographs of the ultrathin GO sheets formed by exfoliation of graphite oxide. AFM was also utilized to characterize size and thickness of GO nanolayers. Figure 3b shows a typical AFM topography of GO on a mica substrate. Image analyses reveal presence of nanolayers, with a thickness of 0.7–1.5 nm and average thickness of 1 nm, indicating that the product is mostly GO monolayer [11]. On the other hand, the lateral size of GO sheets ranges from 150 to 1000 nm and average size of 380 nm. The aspect ratio of nanolayer plays a crucial role in determining the final properties of the composite; therefore, distribution of aspect ratio of the resulting GO nanolayer was obtained from AFM and presented in Figure 3c. The average aspect ratio of GO is roughly 350.

3.2. Functionalization of GO

Many researchers have employed multi-step procedures for amino functionalization of CNTs and graphene using a large amount of organic solvents. In addition, presence of some chemical groups such as acyl chloride, which are very sensitive to moisture and impurities, makes it difficult to control the reaction [38–40]. Therefore a fast and effective amino functionalization of GO through a one pot reaction with diamines is highly desirable. Similar processes have been employed for amino functionalization of clay nanosheets [43].

Figure 4 shows FTIR spectra for GO and fGO. Peaks at 3420 and 1722 cm^{-1} indicate the presence of hydroxyl and carboxyl groups in the structure of GO [41]. Epoxide groups are evidenced by the peak at 1226 cm^{-1}. The adsorption intensity is higher at the peaks of 1226 cm^{-1} in GO spectrum compared with fGO (Figure 4) which may be attributed to the reaction of epoxide groups through the ring opening [44, 45]. It should be noted, that Chen *et al.* [45] recently found that PPDA can effectively reduce GO. However, no remarkable increase in electrical conductivity of GO was observed after functionalization which implies that reduction of GO did not occur significantly. On the other hand, the intensity
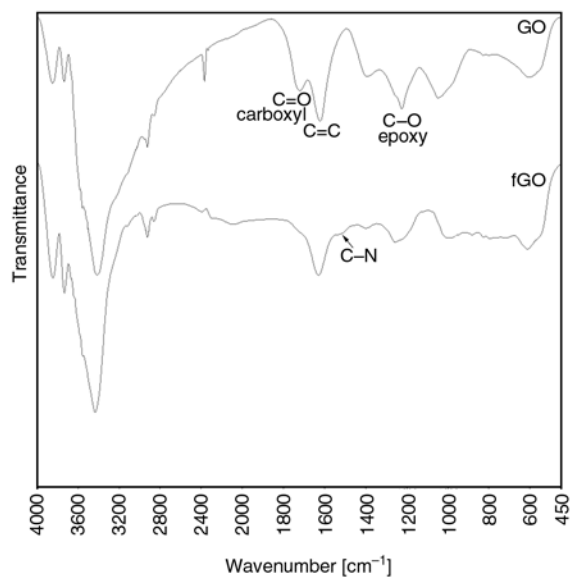

Figure 4. FTIR spectra for (a) graphite oxide powders and (b) PPDA functionalized graphene oxide powders

of the peak at 1722 cm^{-1} which is the indication of the carbonyl group (C=O), is weaker hinting to the formation of ammonium carboxylate complex [41, 44]. Furthermore, disappearance of sharp peak at 2350 cm^{-1} which is attributed to the stretching of hydroxyl of carboxyl acid groups, is another sign of formation of ammonium-carboxylate complex. There is also a new peak at 1500 cm^{-1} for fGO which is the indication of C–N bond stretch in fGO [44]. C–N bond formation can be attributed to a S_N2 nucleophilic substitution and ring opening reaction resulting in new bond formation between carbon atoms in GO and nitrogen in PPDA. In addition, attachment of PPDA moieties on the surface of GO creates some amine groups with the C–N bond.

XPS was employed to analyze the chemical structure of GO and fGO (Figure 5). Figure 5a presents the XPS spectrum of GO in the region of 0 to 800 eV. In the broad scan of the GO spectrum, presence of carbon and oxygen is confirmed with C/O ratio of 1.88. This is consistent with the reported chemical composition of GO in the literature where the C/O ratio is around 2 [14, 16]. The GO spectrum in N1s region (400 eV) reveals that the nitrogen content in the GO is less than 0.1 wt% (Figure 5b).

After GO was functionalized by PPDA, in the broad scan spectrum, a new peak around 400 eV appears which is attributed to N1s component (Figure 5c). This indicates successful amino functionalization of GO using PPDA. Amine treated GO, has C/O ratio of 2.43 which is slightly higher than GO itself. This
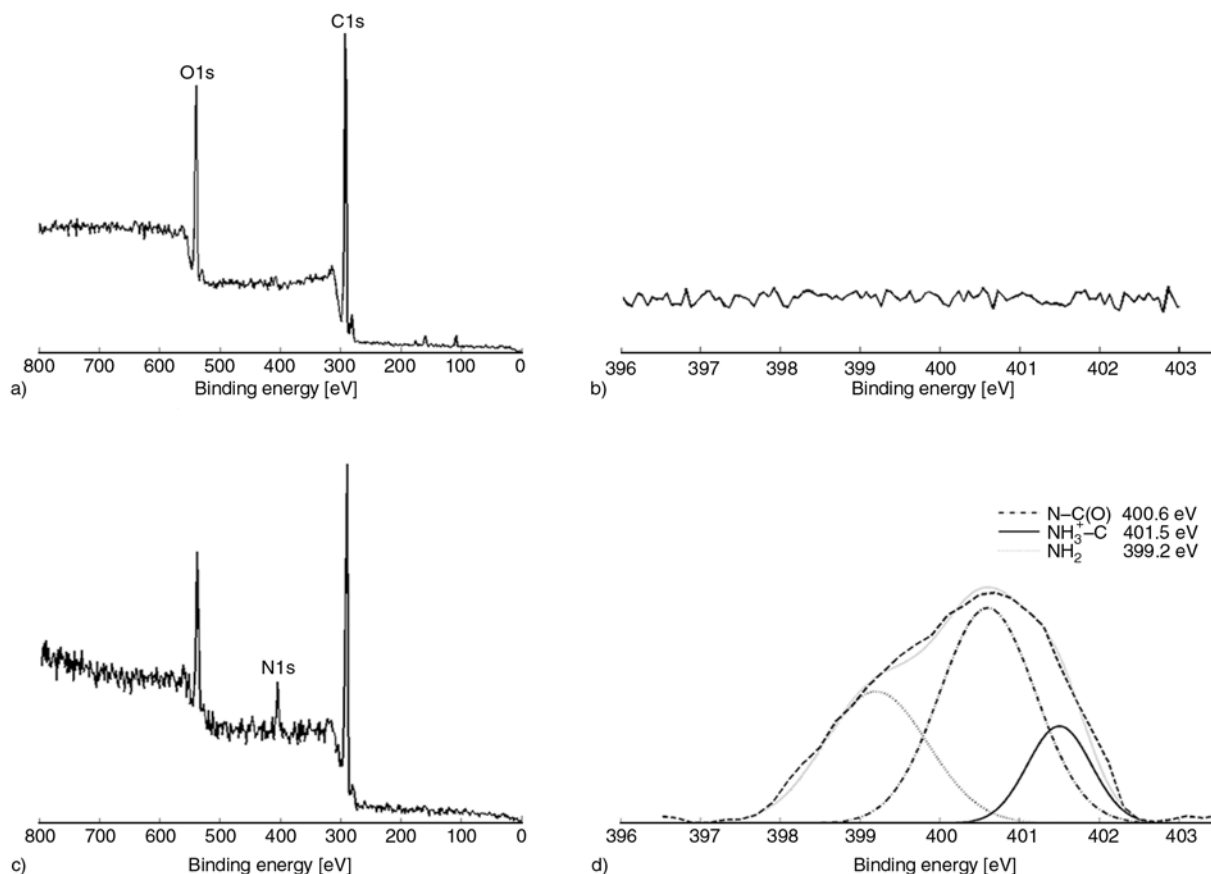
Figure 5. XPS spectra of (a, b) GO and (c, d) fGO samples, (a, c) wide region and (b, d) spectra in the N1s region

increase in C/O ratio might be attributed to incorporation of carbon atoms after functionalization by PPDA. The nitrogen content in fGO is remarkably higher, compared with GO. C/N ratio reaches to 14.5 which is similar to alkylamines modified GO [41, 42]. Considering the chemical structure of PPDA ($C_6N_2H_8$), it is realized that there is one PPDA moiety for every 23 carbon atoms in the reaction product. In addition, these analysis give $C_{2.0}O_{1.04}$-$(PPDA)_{0.087}$ empirical formula for the fGO. Thus, the ratio of carbon to oxygen in fGO after subtracting PPDA contribution is around 1.93 which shows no reduction during functionalization reaction indicating that no significant oxidizative or polymerization reaction have occurred, in contrast to Chen *et al.* [45] report where formation of oxidized-PPDA byproducts is observed. Figure 5d which is the deconvoluted N1s spectrum of fGO supports the presence of nitrogen in the forms of NH_2 (399.2 eV), N–C(O) (400.6 eV), NH_3^+–C (401.5 eV). This suggests reaction of PPDA with GO through both ring opening and ammonium carboxylate formation.

As mentioned earlier aqueous GO dispersion was stable for months. However, the reaction between GO and amine results in fGO agglomeration in a few minutes. Previous studies have revealed that aqueous dispersion of GO is stable because of electrostatic stabilization resulting from ionization of carboxyl groups [15]. Destabilization of GO during the reaction with amine appears to be the result of neutralization of carboxyl ion as supported by FTIR and XPS observations [44].

Based on above observations and analyses, a scheme for functionalization is proposed (Figure 6a). Diamine molecules react with GO through a ring opening reaction and covalently graft on the surface of GO. Due to the excess amount of diamine, mostly one amine group participates in this reaction. Meanwhile, PPDA molecules form ammonium carboxylate complex with carboxyl groups in the structure of GO. Therefore, formation of amine groups at both basal plane and the edge of GO sheets is possible due to the presence of epoxy group at basal plane and carboxyl group at the edges.
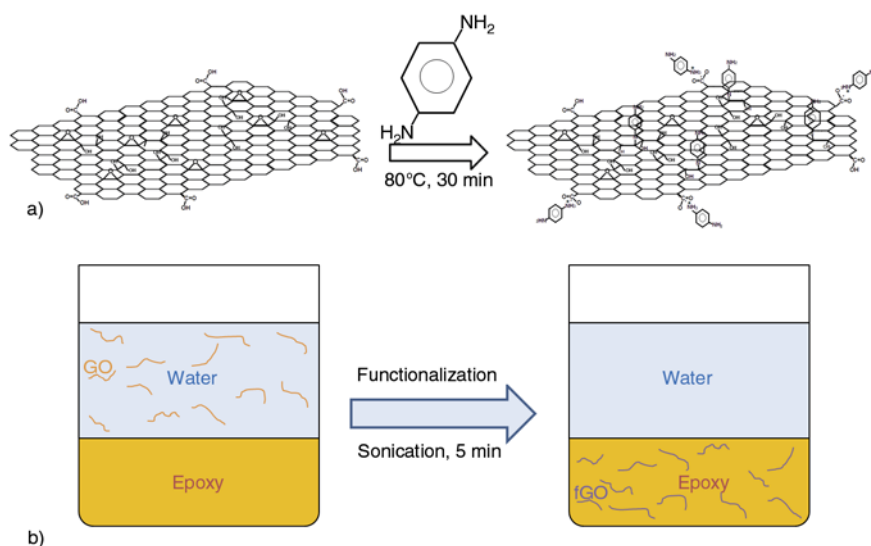
Figure 6. (a) Schematic representation diamine bonding to GO. (b) Schematic illustration of transferring GO sheets from water to epoxy phase after functionalization.

3.3. Dispersing fGO in epoxy

Immiscible 'target' phase, *e.g.* epoxy, and 'transfer' phase, *e.g.* water, were mixed to produce a mixture of highly dispersed fGO in epoxy (Figure 6b). Untreated GO sheets, which are dispersed in the transfer phase migrate to the target phase, while the reaction takes place and sheets become compatible with the epoxy. As mentioned earlier, 'wet' transfer of GO sheets prohibits restacking and agglomeration of nanosheets [33]. Also addition of amine to GO dispersion destabilizes the graphene sheets, aggregates of fGO are still loose since water molecules act as spacer among them. These loose aggregates are more compatible with epoxy resin due to amino-functionalization and migrate to organic phase. Our attempts fail to achieve homogeneous dispersion of fGO in epoxy when dried powder of fGO directly mixed with epoxy resin clearly illustrates the crucial role of mixing strategy to fine dispersion of graphenic sheets. This method has been employed to disperse clay [46], silica [47], and graphene [26, 48, 49] in organic media. Presence of oxygen groups, amine groups and aromatic rings in the structure of fGO, makes it compatible with epoxy resin, facilitating the dispersion of fGO sheets in epoxy and formation of possible hydrogen or covalent bonds. The result was a dark violet homogeneous dispersion of fGO in the epoxy.

Dispersion of the fGO sheets in the final mixture was studied using optical microscopy. Figure 7 shows that fGO sheets have been dispersed homo-

Figure 7. Optical microscopy images of uncured epoxy containing 0.26 vol% fGO coated on glass substrate. Inset shows a picture of the dispersion between glass slides

geneously throughout the matrix. Due to the high specific surface area of graphene sheets, they can be observed thoroughly in the micrograph, even at very low concentrations (0.26 vol%).

The quality of dispersion was also examined by SEM and shown in Figure 8. Figure 8c–8e are the SEM images of the fractured surface of the epoxy-fGO composite. Similar to the optical micrograph observations, there is no sign of agglomeration of graphene sheets. Roughness of the fractured surface
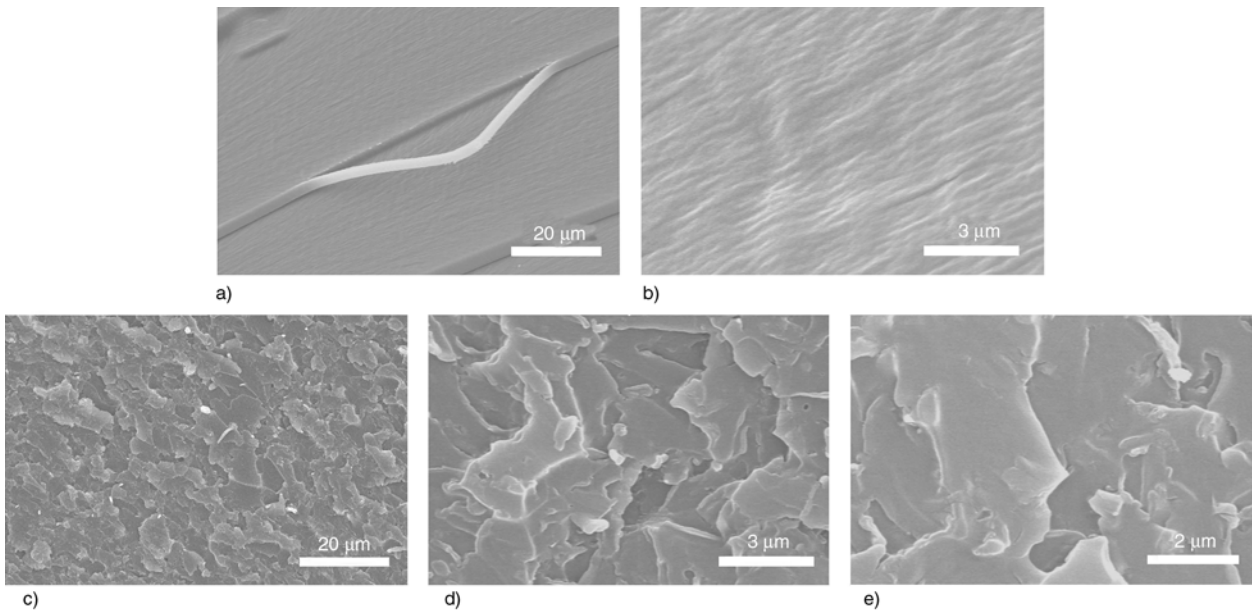
Figure 8. SEM images of fracture surface of (a, b) neat resin and (c–e) composite containing 0.2 vol% fGO at different magnifications

of the composite drastically increases upon addition of the fGO sheet to matrix compared to the neat resin, probably because of the fine dispersion of graphene sheets throughout the matrix. The fractographs of the pristine resin illustrate a very smooth surface with some stripes in the direction of fracturing force (Figure 8a and 8b). On the other hand, incorporating the fGO sheets into the matrix resulted in the formation of irregular protuberances evenly distributed in the whole fractured surface of the composites. These protuberances come into sight in the form of the bright lines with sizes of few hundreds of nanometers to few microns. Formation of these homogenously dispersed lines arise from fine embedding of graphenic layers which are strongly bonded with epoxy matrix without any debonding or pull-out of nanolayers. The strong attachment may be attributed to the covalent bond formation between epoxy matrix and fGO sheets during the curing process. Improved dispersion and bonding of graphene sheets can significantly affect the final mechanical properties of composites [12].

Changes in fractured surface of composites, and dispersion state of graphene sheets in the matrix were also examined by AFM. Figure 9 shows topology of fracture surface of pristine epoxy and composite containing 0.2 vol% fGO. Similar to SEM analysis, the fracture surface of neat resin appears very smooth (Figure 9a). The average roughness of the resulting surface was found to be around
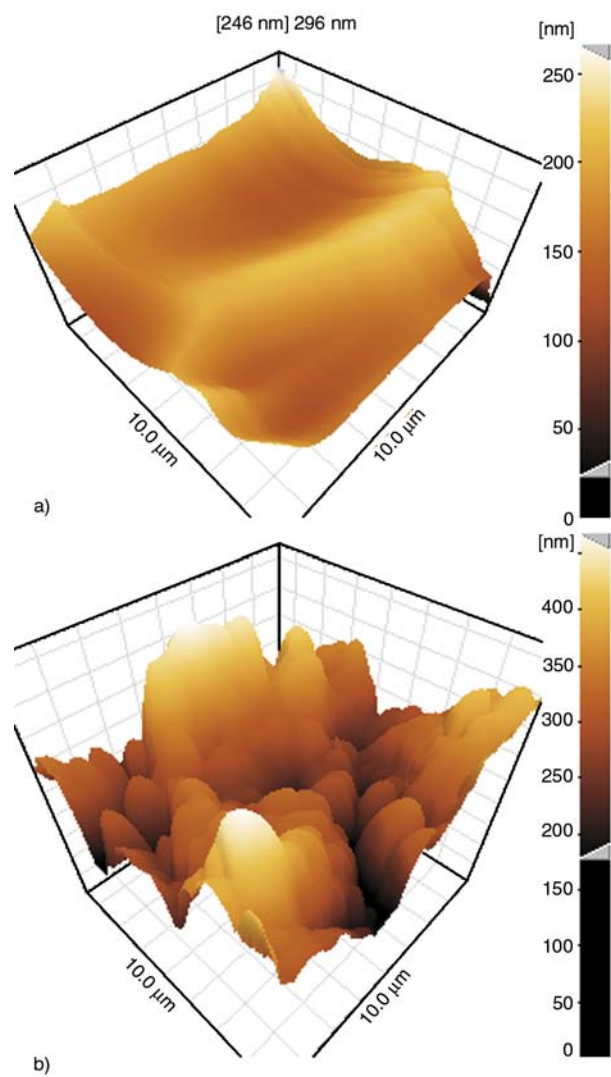
Figure 9. AFM images of fracture surface of (a) neat resin and (b) composite containing 0.4 wt% fGO

0.03±0.01 μm. On the other hand, incorporating fGO nanosheets into epoxy resin makes the fracture surface bumpy which is consistent with SEM observations (Figure 9b). The average roughness of the surface remarkably increases to 0.1±0.02 μm, after addition of 0.2 vol% fGO. The increase in the surface roughness indicates induced crack deflection by graphenic sheets, during the fracture. This may improve not only the stiffness but also fracture toughness and ductility of the composite [27].

Chemical treatment of nanofillers surfaces has been widely reported to improve final properties of the composites [11, 38–40]. Recently, Rafiee *et al*. [27] has reported significant improvement in mechanical properties of the epoxy matrix by addition of a very small amount of graphene sheets. However, mechanical properties of composites diminished, as the graphene content increased to more than 0.1 wt%. The diminishing effect has been attributed to the lack of proper dispersion. Recently reported two-phase extraction method, for production of the epoxy-GO composite was not able to load graphene higher than 0.15 wt% [26], while we were able to load graphene into epoxy up to 0.5 vol% (~1 wt%). A recent work on fabrication of epoxy-amine rich graphene dealt with a laborious and time consuming functionalization procedure [28] whereas one can produce epoxy-GO nanocomposites through fast and facile reaction of diamines with GO, and two phase extraction method, in large scale and for industrial purposes.

Although SEM and optical microscope images demonstrate a homogeneous dispersion of the fGO sheets in the epoxy matrix, rheological measurements have been used to show that the nano sheets are dispersed as single layers.

Rheological percolation threshold of a mixture, containing anisotropic particles is inversely proportional to the aspect ratio of particles and dispersion state of the filler [11, 50–53]. For a given aspect ratio, the percolation threshold of composites decreases as dispersion of the filler improves. In addition, many models have been developed to calculate the percolation threshold of the composite system as a function of aspect ratio [50, 52]. Thus, it is possible to assess the dispersion state of filler in a composite by comparing the predicted percolation threshold and the actual one. AFM observation (Figure 3) of the samples gave an average aspect ratio of 350. For randomly oriented ellipsoids with an aspect ratio of 350 the theoretical percolation threshold is estimated to be around 0.2 vol% [50].

Figure 10a is the graph of complex viscosity of uncured epoxy composites as a function of frequency. Neat resin, and mixtures containing up to 0.05 vol% fGO, have a Newtonian behavior. For mixtures containing 0.16 vol% of fGO, a shear thinning behavior is observed. The flow index reaches to 0.7 for 0.26 vol% accompanied by a significant increase in complex viscosity. Storage modulus of resin increases by addition of the filler (Figure 10b). At low frequency, storage modulus (G') significantly
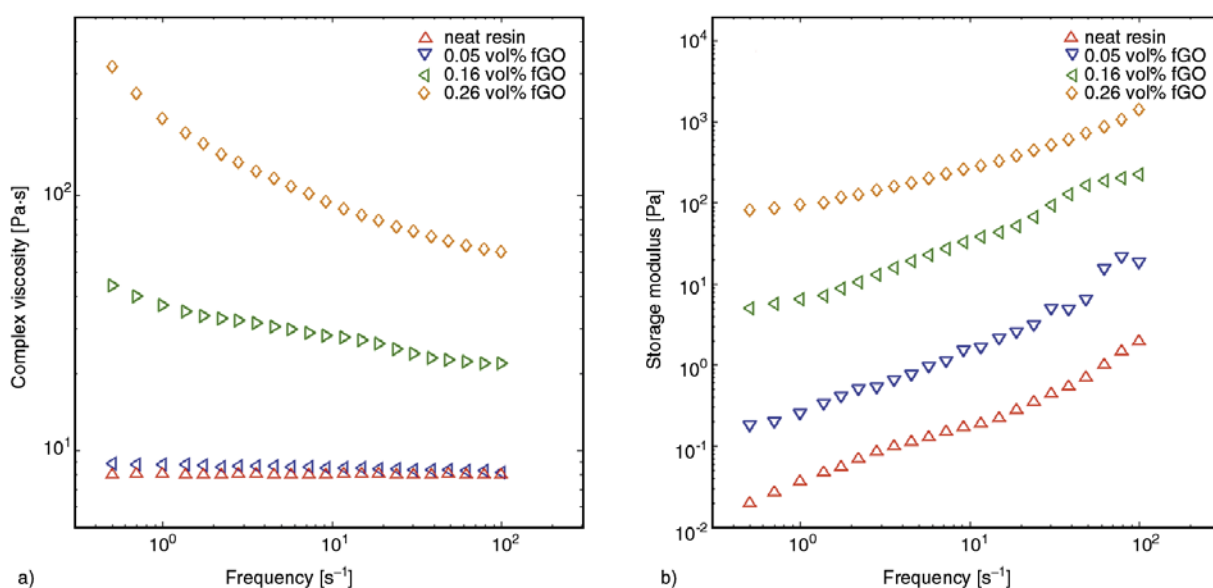
Figure 10. Results of rheometery for uncured epoxy-fGO mixtures with different fGO content (0 to 0.26 vol%) as a function of frequency at room temperature (a) complex viscosity and (b) storage modulus

increases and dependency on frequency decreases as fGO concentration increases and reaches a plateau for 0.26 vol% mixtures, showing solid-like flow behavior. These transitions in flow properties of resin upon addition of fGO are typical when a percolating network exists [51]. In other words, such behavior was an indication of network formation involving assembly of single nanolayers into a 3D network at very low concentration [53].

Therefore, the percolation threshold of the mixture is between 0.16 and 0.26 vol%. Such a low percolation threshold is strong evidence for excellent homogenous dispersion of monolayers throughout the matrix. Surprisingly, the obtained value for percolation threshold agrees very well with the predicted one (~0.2 vol%), substantiating the dispersion of monolayers, namely molecular level dispersion [11].

Recent studies on polymer-graphene nanocomposites have reported percolation thresholds, electrical or rheological, higher than theoretical values [54–57]. The use of melt mixing and even solution mixing of graphene sheets in different polymer matrices has resulted in a percolation threshold of 0.5 to 1 vol% of graphene [54–57]. An exceptionally low percolation threshold of epoxy-fGO composite, which is competitive with solution processed polymer-graphene, is an evidence for success of this method in dispersion of graphenic sheets [11].

3.4. Tensile properties

Mechanical properties of composites containing fGO were also studied in order to evaluate the effect of functionalization on the final composites. Figure 11 shows typical stress-strain curves from three points bending test. Flexural modulus of epoxy increased monotonically by addition of fGO and increased from 2800±25 MPa (neat resin) to 3670±60 MPa for composites containing 0.4 vol% fGO. In addition, ultimate flexural stresses increased by addition of graphenic nanosheets reaching up to 170 MPa after addition of 0.4 vol% fGO while strain to break shows marginal decrease at all fGO content. These notable enhancements in the mechanical properties of the epoxy-fGO composites can be attributed to strong bonding of nanosheets and matrix arising from covalent bonding between them and also fine dispersion of graphene layers through the matrix. However, compared with the neat epoxy,
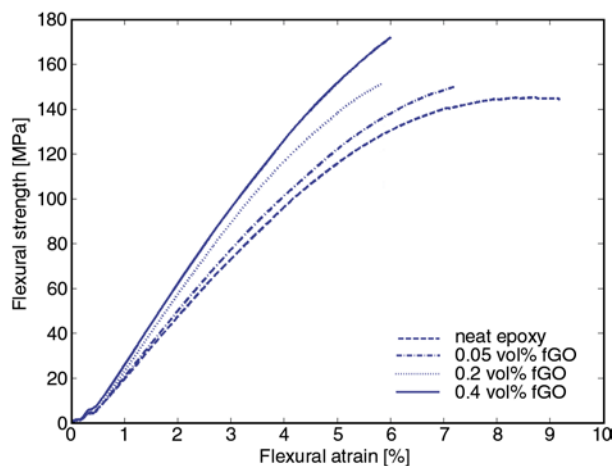
Figure 11. Typical flexural strength versus strain curves for neat resin and composites containing different fGO content

one can find just about a 30 and 12% increase in Young's modulus and ultimate strength by addition of 0.4 vol% fGO, respectively.

From composite science point of view, reinforcing a stiff matrix is more difficult rather than a soft polymer. As a result, comparing the relative enhancement of mechanical properties is not a fair way. Reasonable comparison can be performed through the calculating the reinforcing efficiency of reinforcing phase, *i.e.* graphene. One can estimate the mechanical properties of a composite material according rule of mixture as Equation (1) [58]:

$$Y_c = \varepsilon \cdot Y_f \cdot \varphi + Y_m(1 - \varphi) \tag{1}$$

where Y is mechanical property (modulus or strength) of composite, filler or matrix and φ is volume fraction (Equation 1). ε is reinforcing efficiency factor and therefore $0 < \varepsilon < 1$. In fact, $\varepsilon \cdot Y_f$ can be considered as efficient mechanical property of filler which is sensed by matrix. This parameter represents the efficiency of filler as reinforcing phase and is a good measure of comparing the composite systems having similar filler. At low filler content (Equation (2)):

$$\varepsilon \cdot Y_f \approx \frac{Y_c - Y_m}{\varphi} \tag{2}$$

In our system, efficient modulus and strength of graphene therefore is about 217 and 7.5 GPa (at volume fraction of 0.4 vol%), respectively (Equation (2)). Figure 12a shows comparison of this

parameter in different polymer-graphene systems prepared with various methods. The results obtained in this study are located at top fraction of those calculated from literature [12, 28, 29, 59–70], reflecting the superior performance of developed method to incorporate graphene in thermoset matrix.

Apart from effective stiffening of epoxy resin, no limitation in reinforcing of matrix was observed by increasing the graphene content except thickening of resin whereas degradation in use of nanofiller as stiffening phase at high loading is quite common. For epoxy-graphene nanocomposites, Rafiee *et al.* [27] found remarkable enhancement in tensile properties of epoxy after addition of less than 0.125 wt% functionalized graphene (50% in Young's modulus and ~45% in ultimate strength) whereas tensile properties dropped to even lower than baseline epoxy after addition of 0.5 wt% graphene. In their recent work on epoxy-graphene nanoribbon nanocomposites, similar degradation in the performance of graphene for reinforcing epoxy has been observed after the addition of just 0.3 wt% graphene nanoribbon [71]. In our case, no degradation is observed in the superior performance of graphene sheets for reinforcing polymer matrix which is based on strong interaction of filler and matrix and molecular level dispersion of fGO sheets through the epoxy matrix.

The Halpin-Tsai model is widely used to calculate the modulus of nanocomposites containing platelet or fibril like fillers [72]. For a randomly distributed platelet with modulus of E_f in a matrix with modulus of E_m, the modulus of a composite containing φ vol% of filler is estimated as Equation (3):

$$\frac{E}{E_m} = \frac{1 + 2\alpha\eta\varphi}{1 - \eta\varphi} \tag{3}$$

where α is the aspect ratio of platelet and η is given as Equation (4):

$$\eta = \frac{\dfrac{E_f}{E_m} - 1}{\dfrac{E_f}{E_m} + 2\alpha} \tag{4}$$

Considering the modulus of chemically derived graphene to be roughly 250 GPa [73], and an average aspect ratio of 350 for fGO sheets, the theoretical modulus of composites can be calculated as a function of graphene content (Equations (3) and (4)). Figure 12b shows theoretical modulus of composites compared with the experimental data. The close agreement between theoretical predictions and experimental measurements further confirms that graphene is indeed dispersed as single layers with a strong bond to the resin which has resulted in perfect load transfer to graphene sheets. If the aspect ratio of fGO considered lower than one for GO (350) due to the short sonication (10 minutes) for homogenization, the theoritical prediction would be lower than experimental results which is usually attributed to the formation of a stiffened interphase [58].
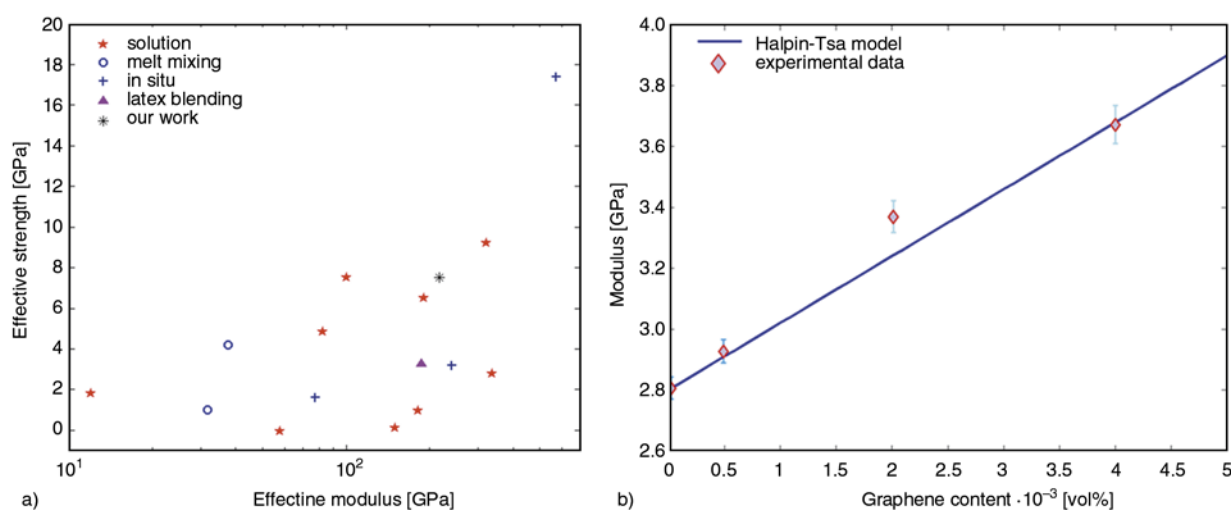
Figure 12. (a) Comparison of effective modulus and strength of graphene in polymer-graphene composites fabricated through different methods [12, 28, 29, 59–70] and the result obtained in this study. (b) Young's modulus of epoxy composites as a function of graphene content. The line illustrates Halpin-Tsai prediction for Young's modulus of composites containing ellipsoids with random dispersion as a function of graphene volume fraction showing agreement of theoretical prediction and experimental data.

Finally, it is worth noting that the above analysis shows that there is still large room for improving final mechanical properties and possibly other properties of nanocomposites by using graphene with larger aspect ratio and higher content. However, high viscosity of highly filled epoxy-graphene nanocomposites challenges the processing and application. Interfacial interaction of graphene and matrix can also be tuned by using amines with different molecular stiffness [28]. We believe this work paves the way for production of highly dispersed epoxy-graphene nanocomposites using a general approach.

4. Conclusions

The application of a two phase reacting system for functionalization of graphene oxide is shown to result in a very ideal graphene epoxy composite. It is ideal in the sense that graphene sheets are well dispersed to single layers and have very good bonding with the epoxy. It is observed that good dispersion and bonding can be maintained up to 0.5 vol% (~1 wt%). Therefore, functionalization of GO using the two phase method has served three purposes that are all important in improvement of epoxy-graphene composite; increasing the graphene content while maintaining good dispersion and furnishing good bonding between graphene and epoxy.

Acknowledgements

References

[1] Kroto H. W., Heath J. R., O'Brien S. C., Curl R. F., Smalley R. E.: C$_{60}$: Buckminsterfullerene. Nature, **318**, 162–163 (1985).
DOI: 10.1038/318162a0

[2] Iijima S.: Helical microtubules of graphitic carbon. Nature, **354**, 56–58 (1991).
DOI: 10.1038/354056a0

[3] Geim A. K., Novoselov K. S.: The rise of graphene. Nature Materials, **6**, 183–191 (2007).
DOI: 10.1038/nmat1849

[4] Coleman J. N., Khan U., Blau W. J., Gun'ko Y. K.: Small but strong: A review of the mechanical properties of carbon nanotube–polymer composites. Carbon, **44**, 1624–1652 (2006).
DOI: 10.1016/j.carbon.2006.02.038

[5] Potts J. R., Dreyer D. R., Bielawski C. W., Ruoff R. S.: Graphene-based polymer nanocomposites. Polymer, **52**, 5–25 (2011).
DOI: 10.1016/j.polymer.2010.11.042

[6] Liu Q., Liu Z., Zhang X., Yang L., Zhang N., Pan G., Yin S., Chen Y., Wei J.: Polymer photovoltaic cells based on solution-processable graphene and P3HT. Advanced Functional Materials, **19**, 894–904 (2009).
DOI: 10.1002/adfm.200800954

[7] Li N., Huang Y., Du F., He X., Lin X., Gao H., Ma Y., Li F., Chen Y., Eklund P. C.: Electromagnetic interference (EMI) shielding of single-walled carbon nanotube epoxy composites. Nano Letters, **6**, 1141–1145 (2006).
DOI: 10.1021/nl0602589

[8] Kauffman D. R., Star A.: Carbon nanotube gas and vapor sensors. Angewandte Chemie International Edition, **47**, 6550–6570 (2008).
DOI: 10.1002/anie.200704488

[9] Baughman R. H., Zakhidov A. A., de Heer W. A.: Carbon nanotubes – The route toward applications. Science, **297**, 787–792 (2002).
DOI: 10.1126/science.1060928

[10] Du J-H., Bai J., Cheng H-M.: The present status and key problems of carbon nanotube based polymer composites. Express Polymer Letters, **1**, 253–273 (2007).
DOI: 10.3144/expresspolymlett.2007.39

[11] Stankovich S., Dikin D. A., Dommett G. H. B., Kohlhaas K. M., Zimney E. J., Stach E. A., Piner R. D., Nguyen S. T., Ruoff R. S.: Graphene-based composite materials. Nature, **442**, 282–286 (2006).
DOI: 10.1038/nature04969

[12] Ramanathan T., Abdala A. A., Stankovich S., Dikin D. A., Herrera-Alonso M., Piner R. D., Adamson D. H., Schniepp H. C., Chen X., Ruoff R. S., Nguyen S. T., Aksay I. A., Prud'Homme R. K., Brinson L. C.: Functionalized graphene sheets for polymer nanocomposites. Nature Nanotechnology, **3**, 327–331 (2008).
DOI: 10.1038/nnano.2008.96

[13] Tjong S. C.: Graphene and its derivatives: Novel materials for forming functional polymer nanocomposites. Express Polymer Letters, **6**, 437 (2012).
DOI: 10.3144/expresspolymlett.2012.46

[14] Park S., Ruoff R. S.: Chemical methods for the production of graphenes. Nature Nanotechnology, **4**, 217–224 (2009).
DOI: 10.1038/nnano.2009.58

[15] Li D., Müller M. B., Gilje S., Kaner R. B., Wallace G. G.: Processable aqueous dispersions of graphene nanosheets. Nature Nanotechnology, **3**, 101–105 (2008).
DOI: 10.1038/nnano.2007.451

[16] Pan S., Aksay I. A.: Factors controlling the size of graphene oxide sheets produced *via* the graphite oxide route. ACS Nano, **5**, 4073–4083 (2011).
DOI: 10.1021/nn200666r

[17] Gudarzi M. M., Sharif F.: Characteristics of polymers that stabilize colloids for the production of graphene from graphene oxide. Journal of Colloid and Interface Science, **349**, 63–69 (2010).
DOI: 10.1016/j.jcis.2010.05.064

[18] Qiu S. L., Wang C. S., Wang Y. T., Liu C. G., Chen X. Y., Xie H. F., Huang Y. A., Cheng R. S.: Effects of graphene oxides on the cure behaviors of a tetrafunctional epoxy resin. Express Polymer Letters, **5**, 809–818 (2011).
DOI: 10.3144/expresspolymlett.2011.79

[19] Lomeda J. R., Doyle C. D., Kosynkin D. V., Hwang W-F., Tour J. M.: Diazonium functionalization of surfactant-wrapped chemically converted graphene sheets. Journal of the American Chemical Society, **130**, 16201–16206 (2008).
DOI: 10.1021/ja806499w

[20] Allen M. J., Tung V. C., Kaner R. B.: Honeycomb carbon: A review of graphene. Chemical Reviews, **110**, 132–145 (2010).
DOI: 10.1021/cr900070d

[21] Tkalya E., Ghislandi M., Alekseev A., Koning C., Loos J.: Latex-based concept for the preparation of graphene-based polymer nanocomposites. Journal of Materials Chemistry, **20**, 3035–3039 (2010).
DOI: 10.1039/B922604D

[22] Gudarzi M. M., Sharif F.: Molecular level dispersion of graphene in polymer matrices using colloidal polymer and graphene. Journal of Colloid and Interface Science, **366**, 44–50 (2012).
DOI: 10.1016/j.jcis.2011.09.086

[23] Yousefi N., Gudarzi M. M., Zheng Q., Aboutalebi S. H., Sharif F., Kim J-K.: Self-alignment and high electrical conductivity of ultralarge graphene oxide–polyurethane nanocomposites. Journal of Materials Chemistry, **22**, 12709–12717 (2012).
DOI: 10.1039/c2jm30590a

[24] Yoonessi M., Gaier J. R.: Highly conductive multifunctional graphene polycarbonate nanocomposites. ACS Nano, **4**, 7211–7220 (2010).
DOI: 10.1021/nn1019626

[25] Gudarzi M. M., Sharif F.: Self assembly of graphene oxide at the liquid–liquid interface: A new route to the fabrication of graphene based composites. Soft Matter, **7**, 3432–3440 (2011).
DOI: 10.1039/C0SM01311K

[26] Yang H., Shan C., Li F., Zhang Q., Han D., Niu L.: Convenient preparation of tunably loaded chemically converted graphene oxide/epoxy resin nanocomposites from graphene oxide sheets through two-phase extraction. Journal of Materials Chemistry, **19**, 8856–8860 (2009).
DOI: 10.1039/B915228H

[27] Rafiee M. A., Rafiee J., Srivastava I., Wang Z., Song H., Yu Z-Z., Koratkar N.: Fracture and fatigue in graphene nanocomposites. Small, **6**, 179–183 (2009).
DOI: 10.1002/smll.200901480

[28] Fang M., Zhang Z., Li J., Zhang H., Lu H., Yang Y.: Constructing hierarchically structured interphases for strong and tough epoxy nanocomposites by amine-rich graphene surfaces. Journal of Materials Chemistry, **20**, 9635–9643 (2010).
DOI: 10.1039/C0JM01620A

[29] Bortz D. R., Heras E. G., Martin-Gullon I.: Impressive fatigue life and fracture toughness improvements in graphene oxide/epoxy composites. Macromolecules, **45**, 238–245 (2012).
DOI: 10.1021/ma201563k

[30] Wang S., Tambraparni M., Qiu J., Tipton J., Dean D.: Thermal expansion of graphene composites. Macromolecules, **42**, 5251–5255 (2009).
DOI: 10.1021/ma900631c

[31] Rafiee M. A., Rafiee J., Wang Z., Song H., Yu Z-Z., Koratkar N.: Enhanced mechanical properties of nanocomposites at low graphene content. ACS Nano, **3**, 3884–3890 (2009).
DOI: 10.1021/nn9010472

[32] Aboutalebi S. H., Gudarzi M. M., Zheng Q. B., Kim J-K.: Spontaneous formation of liquid crystals in ultralarge graphene oxide dispersions. Advanced Functional Materials, **21**, 2978–2988 (2011).
DOI: 10.1002/adfm.201100448

[33] Yang X., Zhu J., Qiu L., Li D.: Bioinspired effective prevention of restacking in multilayered graphene films: Towards the next generation of high-performance supercapacitors. Advanced Materials, **23**, 2833–2838 (2011).
DOI: 10.1002/adma.201100261

[34] Yang X., Qiu L., Cheng C., Wu Y., Ma Z-F., Li D.: Ordered gelation of chemically converted graphene for next-generation electroconductive hydrogel films. Angewandte Chemie – International Edition, **50**, 7325–7328 (2011).
DOI: 10.1002/anie.201100723

[35] Luo J., Jang H. D., Sun T., Xiao L., He Z., Katsoulidis A. P., Kanatzidis M. G., Gibson J. M., Huang J.: Compression and aggregation-resistant particles of crumpled soft sheets. ACS Nano, **5**, 8943–8949 (2011).
DOI: 10.1021/nn203115u

[36] Kim H., Abdala A. A., Macosko C. W.: Graphene/polymer nanocomposites. Macromolecules, **43**, 6515–6530 (2010).
DOI: 10.1021/ma100572e

[37] Hummers Jr W. S., Offeman R. E.: Preparation of graphitic oxide. Journal of the American Chemical Society, **80**, 1339 (1958).
DOI: 10.1021/ja01539a017

[38] Gojny F. H., Wichmann M. H. G., Köpke U., Fiedler B., Schulte K.: Carbon nanotube-reinforced epoxy-composites: enhanced stiffness and fracture toughness at low nanotube content. Composites Science and Technology, **64**, 2363–2371 (2004).
DOI: 10.1016/j.compscitech.2004.04.002

[39] Shen J., Huang W., Wu L., Hu Y., Ye M.: The reinforcement role of different amino-functionalized multi-walled carbon nanotubes in epoxy nanocomposites. Composites Science and Technology, **67**, 3041–3050 (2007).
DOI: 10.1016/j.compscitech.2007.04.025

[40] Zheng Y., Zhang A., Chen Q., Zhang J., Ning R.: Functionalized effect on carbon nanotube/epoxy nano-composites. Materials Science and Engineering A, **435–436**, 145–149 (2006).
DOI: 10.1016/j.msea.2006.07.106

[41] Wang S., Chia P-J., Chua L-L., Zhao L-H., Png R-Q., Sivaramakrishnan S., Zhou M., Goh R-G. S., Friend R-H., Wee A. T-S., Ho P. K-H.: Band-like transport in surface-functionalized highly solution-processable graphene nanosheets. Advanced Materials, **20**, 3440–3446 (2008).
DOI: 10.1002/adma.200800279

[42] Wang G., Shen X., Wang B., Yao J., Park J.: Synthesis and characterisation of hydrophilic and organophilic graphene nanosheets. Carbon, **47**, 1359–1364 (2009).
DOI: 10.1016/j.carbon.2009.01.027

[43] Zaarei D., Sarabi A. A., Sharif F., Gudarzi M. M., Kassiriha S. M.: Using of p-phenylenediamine as modifier of montmorilonite for preparation of epoxy-clay nano-composites: Morphology and solvent resistance properties. Polymer-Plastics Technology and Engineering, **49**, 285–291 (2010).
DOI: 10.1080/03602550903413946

[44] Park S., Dikin D. A., Nguyen S. T., Ruoff R. S.: Graphene oxide sheets chemically cross-linked by polyallylamine. Journal of Physical Chemistry C, **113**, 15801–15804 (2009).
DOI: 10.1021/jp907613s

[45] Chen Y., Zhang X., Yu P., Ma Y.: Stable dispersions of graphene and highly conducting graphene films: A new approach to creating colloids of graphene monolayers. Chemical Communications, **45**, 4527–4529 (2009).
DOI: 10.1039/B907723E

[46] Ma J., Yu Z-Z., Zhang Q-X., Xie X-L., Mai Y-W., Luck I.: A novel method for preparation of disorderly exfoliated epoxy/clay nanocomposite. Chemistry of Materials, **16**, 757–759 (2004).
DOI: 10.1021/cm0349203

[47] Stelzig S. H., Klapper M., Müllen K.: A simple and efficient route to transparent nanocomposites. Advanced Materials, **20**, 929–932 (2008).
DOI: 10.1002/adma.200701608

[48] Liang Y., Wu D., Feng X., Müllen K.: Dispersion of graphene sheets in organic solvent supported by ionic interactions. Advanced Materials, **21**, 1679–1683 (2009).
DOI: 10.1002/adma.200803160

[49] Wei T., Luo G., Fan Z., Zheng C., Yan J., Yao C., Li W., Zhang C.: Preparation of graphene nanosheet/polymer composites using in situ reduction–extractive dispersion. Carbon, **47**, 2296–2299 (2009).
DOI: 10.1016/j.carbon.2009.04.030

[50] Garboczi E. J., Snyder K. A., Douglas J. F., Thorpe M. F.: Geometrical percolation threshold of overlapping ellipsoids. Physical Review E, **52**, 819–828 (1995).
DOI: 10.1103/PhysRevE.52.819

[51] Kharchenko S. B., Douglas J. F., Obrzut J., Grulke E. A., Milger K. B.: Flow-induced properties of nanotube-filled polymer materials. Nature Materials, **3**, 564–568 (2004).
DOI: 10.1038/nmat1183

[52] Sun L., Boo W-J., Liu J., Clearfield A., Sue H-J., Verghese N. E., Pham H. Q., Bicerano J.: Effect of nanoplatelets on the rheological behavior of epoxy monomers. Macromolecular Materials and Engineering, **294**, 103–113 (2008).
DOI: 10.1002/mame.200800258

[53] Zaarei D., Sarabi A. A., Sharif F., Kassiriha S. M., Gudarzi M. M.: Rheological studies of uncured epoxy–organoclaynanocomposite coatings. e-Polymers, no.117 (2008).

[54] Villar-Rodil S., Paredes J. I., Martínez-Alonso A., Tascón J. M. D.: Preparation of graphene dispersions and graphene-polymer composites in organic media. Journal of Materials Chemistry, **19**, 3591–3593 (2009).
DOI: 10.1039/B904935E

[55] Kim H., Macosko C. W.: Processing-property relationships of polycarbonate/graphene composites. Polymer, **50**, 3797–3809 (2009).
DOI: 10.1016/j.polymer.2009.05.038

[56] Raghu A. V., Lee Y. R., Jeong H. M., Shin C. M.: Preparation and physical properties of waterborne polyurethane/functionalized graphene sheet nanocomposites. Macromolecular Chemistry and Physics, **209**, 2487–2493 (2008).
DOI: 10.1002/macp.200800395

[57] Liang J., Wang Y., Huang Y., Ma Y., Liu Z., Cai J., Zhang C., Gao H., Chen Y.: Electromagnetic interference shielding of graphene/epoxy composites. Carbon, **47**, 922–925 (2009).
DOI: 10.1016/j.carbon.2008.12.038

[58] Coleman J. N., Cadek M., Blake R., Nicolosi V., Ryan K. P., Belton C., Fonseca A., Nagy J. B., Gun'ko Y. K., Blau W. J.: High performance nanotube-reinforced plastics: Understanding the mechanism of strength increase. Advanced Functional Materials, **14**, 791–798 (2004).
DOI: 10.1002/adfm.200305200

[59] Liang J., Huang Y., Zhang L., Wang Y., Ma Y., Guo T., Chen Y.: Molecular-level dispersion of graphene into poly(vinyl alcohol) and effective reinforcement of their nanocomposites. Advanced Functional Materials, **19**, 2297–2302 (2009).
DOI: 10.1002/adfm.200801776

[60] Kim H., Macosko C. W.: Morphology and properties of polyester/exfoliated graphite nanocomposites. Macromolecules, **41**, 3317–3327 (2008).
DOI: 10.1021/ma702385h

[61] Vadukumpully S., Paul J., Mahanta N., Valiyaveettil S.: Flexible conductive graphene/poly(vinyl chloride) composite thin films with high mechanical strength and thermal stability. Carbon, **49**, 198–205 (2011).
DOI: 10.1016/j.carbon.2010.09.004

[62] Zhao X., Zhang Q., Chen D., Lu P.: Enhanced mechanical properties of graphene-based poly(vinyl alcohol) composites. Macromolecules, **43**, 2357–2363 (2010).
DOI: 10.1021/ma902862u

[63] Yang S-Y., Lin W-N., Huang Y-L., Tien H-W., Wang J-Y., Ma C-C. M., Li S-M., Wang Y-S.: Synergetic effects of graphene platelets and carbon nanotubes on the mechanical and thermal properties of epoxy composites. Carbon, **49**, 793–803 (2010).
DOI: 10.1016/j.carbon.2010.10.014

[64] Wang Y., Shi Z., Fang J., Xu H., Yin J.: Graphene oxide/polybenzimidazole composites fabricated by a solvent-exchange method. Carbon, **49**, 1199–1207 (2011).
DOI: 10.1016/j.carbon.2010.11.036

[65] Rafiq R., Cai D., Jin J., Song M.: Increasing the toughness of nylon 12 by the incorporation of functionalized graphene. Carbon, **48**, 4309–4314 (2010).
DOI: 10.1016/j.carbon.2010.07.043

[66] Song P., Cao Z., Cai Y., Zhao L., Fang Z., Fu S.: Fabrication of exfoliated graphene-based polypropylene nanocomposites with enhanced mechanical and thermal properties. Polymer, **52**, 4001–4010 (2011).
DOI: 10.1016/j.polymer.2011.06.045

[67] Potts J. R., Lee S. H., Alam T. M., An J., Stoller M. D., Piner R. D., Ruoff R. S.: Thermomechanical properties of chemically modified graphene/poly(methyl methacrylate) composites made by *in situ* polymerization. Carbon, **49**, 2615–2623 (2011).
DOI: 10.1016/j.carbon.2011.02.023

[68] Yun Y. S., Bae Y. H., Kim D. H., Lee J. Y., Chin I-J., Jin H-J.: Reinforcing effects of adding alkylated graphene oxide to polypropylene. Carbon, **49**, 3553–3559 (2011).
DOI: 10.1016/j.carbon.2011.04.055

[69] Chen D., Zhu H., Liu T.: In situ thermal preparation of polyimide nanocomposite films containing functionalized graphene sheets. ACS Applied Materials and Interfaces, **3**, 3702–3708 (2011).
DOI: 10.1021/am1008437

[70] Gonçalves G., Marques P., Barros-Timmons A., Bdkin I., Singh M. K., Emami N., Grácio J.: Graphene oxide modified with PMMA *via* ATRP as a reinforcement filler. Journal of Materials Chemistry, **20**, 9927–9934 (2010).
DOI: 10.1039/c0jm01674h

[71] Rafiee M. A., Lu W., Thomas A. V., Zandiatashbar A., Rafiee J., Tour J. M., Koratkar N. A.: Graphene nanoribbon composites. ACS Nano, **4**, 7415–7420 (2010).
DOI: 10.1021/nn102529n

[72] Wu Y-P., Jia Q-X., Yu D-S., Zhang L-Q.: Modeling Young's modulus of rubber–clay nanocomposites using composite theories. Polymer Testing, **23**, 903–909 (2004).
DOI: 10.1016/j.polymertesting.2004.05.004

[73] Gómez-Navarro C., Burghard M., Kern K.: Elastic properties of chemically derived single graphene sheets. Nano Letters, **8**, 2045–2049 (2008).
DOI: 10.1021/nl801384y

Influence of chemical treatment on the tensile properties of kenaf fiber reinforced thermoplastic polyurethane composite

Y. A. El-Shekeil[1*], *S. M. Sapuan*[1], *A. Khalina*[2], *E. S. Zainudin*[3], *O. M. Al-Shuja'a*[4]

[1]Department of Mechanical and Manufacturing Engineering, Universiti Putra Malaysia, 43400 Serdang, Selangor, Malaysia

[2]Department of Biological and Agricultural Engineering, Universiti Putra Malaysia, 43400 Serdang, Selangor, Malaysia

[3]Laboratory of Bio-Composite Technology, Institute of Tropical Forestry and Forest Products, Universiti Putra Malaysia, 43400 Serdang, Selangor, Malaysia

[4]Department of Chemistry, Faculty of Applied Science,Thamar University, Thamar, Yemen

Abstract. In this study, the effect of polymeric Methylene Diphenyl Diisocyanate (pMDI) chemical treatment on kenaf (*Hibiscus cannabinus*) reinforced thermoplastic polyurethane (TPU/KF) was examined using two different procedures. The first consisted of treating the fibers with 4% pMDI, and the second involved 2% NaOH + 4% pMDI. The composites were characterized according to their tensile properties, Fourier Transform Infrared Spectroscopy (FTIR) and Scanning Electron Microscopy (SEM). The treatment of the composite with 4% pMDI did not significantly affect its tensile properties, but the treatment with 2% NaOH + 4% pMDI significantly increased the tensile properties of the composite (i.e., 30 and 42% increases in the tensile strength and modulus, respectively). FTIR also showed that treatment with 2% NaOH + 4% pMDI led to the strongest H-bonding. Additionally, the surface morphology of specimens after tensile fracture confirmed that the composite treated with 2% NaOH + 4% pMDI had the best adhesion and wettability.

1. Introduction

Natural fiber composites are having a strong influence in the field of composite materials. Cost effectiveness, a lighter weight, lower abrasion of equipment and renewability are amongst the benefits of natural fiber composites. However, natural fiber composites face some difficulties that prevent their widespread use. Fiber-polymer incompatibility has been the subject of previous studies [1–4]. This incompatibility is caused by the hydrophilic nature of the fibers and the hydrophobic nature of many polymers used in this field. The presence of hemi-cellulose, lignin and other impurities also causes a lack of adhesion between fibers and polymers.

The kenaf plant has a single, straight, unbranched stem. It has a short growing period, high biomass output and good mechanical properties. It reaches 3–4 meters in height in 4–5 months. It is reported that kenaf can yield three times a year in Malaysian climates [5], and in terms of quantity it can yield 2 to 25 ton/acre, depending on many factors such as soil type, variety and the month of planting [6]. Kenaf is traditionally used in cordage, canvas and sacking [7]. Kenaf is a good alternative to wood in the pulp and paper industry [3].

---

*Corresponding author, e-mail: y_shekeil@yahoo.com

Kenaf reinforced thermoplastic polyurethane was developed by the authors in a previous study [8]. Kenaf bast fiber was used because of its fast growth and good mechanical properties. Kenaf also absorbs nitrogen and phosphorus from the soil and accumulates carbon dioxide at a considerably high rate [9]. Thermoplastic polyurethane (TPU) was chosen due to its good mechanical properties and rubber-like elasticity. Another reason for selecting TPU is that polyurethane is polar, which reduces the fiber-polymer incompatibility.

Previously, the effect of various treatments on TPU/KF composites has been considered. The pretreatment of fibers with different concentrations of NaOH resulted in deterioration of its mechanical properties [10]. This result was supported by FTIR, thermogravimetrical analysis TGA and SEM studies.

Using pMDI isocyanate as an additive also showed no significant effect on the properties of the composite when pMDI was placed into the mixer directly before adding the fibers [11]. The NCO active group of isocyanate might have reacted with the matrix before the fibers were added to the mixer, which most likely resulted in the negligible effect on the properties of the composite.

Alkali treatment of natural fibers has several advantages for the removal of undesired substances; it affects the properties of the fibers and fiber-matrix interlocking [12]. Isocyanate has also shown a positive effect when used as a coupling agent between natural fibers and polymers. Previous studies have used isocyanates as coupling agents and reported their positive effect on fiber-matrix interfacial bonding [13–16]. Therefore, in this study, the same treatments (i.e., alkalization and isocyanate) were used with some modifications. Instead of charging the isocyanate into the mixer directly, it was used to pretreat the natural fibers, and in this case, it is referred to as pMDI chemical treatment. Alternatively, the fibers were first mercerized with NaOH and then treated with pMDI. Details on the chemical treatments are given in the methodology. The aim of this research is to investigate the effect of pMDI chemical treatment on TPU/KF composites.

2. Experimental
2.1. Materials
TPU (Texin®) and pMDI (Desmodur® 44V10L) were obtained from Bayer Co. (Malaysia) Sdn Bhd,

Table 1. Characteristics of TPU

Specific gravity	1.21
Tensile strength	48 MPa
Melting temperature	210°C
Hardness	55D

Petaling Jaya, Selangor, Malaysia. The TPU used in this study was polyester based, and the properties are shown in (Table 1). pMDI isocyanate has an NCO content of 30.5 to 32.5 wt%. The kenaf V36 bast fiber used in this study was supplied by KEFI (Malaysia) Sdn Bhd, Setiu, Terengganu, Malaysia.

2.2. Fiber preparation
Mechanical decortication was used to extract the bast fibers. The fibers were pulverized using a Fritsch Power Cutting Mill PULVERISETTE 25 (Fritsch GmbH, Laborgeraetebau, Germany). The fibers were subsequently sieved using an automatic shaker sieve with meshes of 50 to 120 to a size range of 125–300 µm. This fiber size exhibited the optimum mechanical properties for TPU/KF composites [8].

2.3. Fiber treatments
2.3.1. Alkali treatment
The fibers were treated using a 2% aqueous solution of NaOH (by weight). The fibers were soaked in the solution for 3 hours. Subsequently, the fibers were washed 6 times with distilled water and oven dried at 80°C for 24 hours.

2.3.2. pMDI chemical treatment
Kenaf was pre-treated with 4% pMDI by weight of the fiber as follows. First, kenaf was mixed with toluene in a flask. Then, pMDI was mixed with toluene in a dropping funnel and then dropped into the flask over 20 minutes. The flask was heated at 50°C on a flat heater with continuous mixing for one hour. After the treatment, the treated fibers were separated by filtration, washed several times with toluene and dried in an oven at 70°C for 2 hours.

2.4. Composite preparation
2.4.1. Internal mixer
The TPU/KF composite was mixed using a Haake Polydrive R600 internal mixer at 190°C for 11 minutes at 40 rpm. These parameters were used because they led to the optimum tensile strength of the TPU/KF composite [8]. A 30% fiber loading was used

Table 2. The four different formulations prepared in this study

Formulation	Treatment	
	NaOH [%]	pMDI [%]
COMP1	–	–
COMP2	2	–
COMP3	–	4
COMP4	2	4

throughout the study because it resulted in the optimal strength of the composite [17]. TPU was charged into the mixer until the torque was stabilized, and then the fiber was added into the mixer. This procedure is explained in detail in a previous study [8]. Four different formulations were prepared in this study, as shown in (Table 2).

2.4.2. Compression molding
The sample was pre-heated for 7 minutes at 190°C. Then sample was hot-pressed using a Vechno Vation 40 ton compression molding device for 10 minutes at 190°C. Afterwards, the sample was cold pressed at 25°C for 5 minutes.

2.5. Tensile testing
The tensile properties were measured using an Instron 3365 electronic universal testing machine (Instron Co., Norwood, MA, USA) according to ASTM D 638(2010). The specimens were prepared by cutting them into dumbbell shapes using a hydraulic cutter machine. Five specimens were tested with a crosshead speed of 5 mm/min.

2.6. FTIR spectra characterization
The FTIR spectra of raw fibers, treated fibers and composites with and without treatment were recorded in the range of 4000 to 400 cm^{-1} using an FTIR machine Model Perkin-Elmer Spectrum 100 FT-IR Spectrometer (Perkin-Elmer, Norwalk, CT, USA). The samples were compacted into thin pellets with potassium bromide.

2.7. Surface characterization
The morphology of the tensile fracture surfaces of the treated and untreated composites were investigated using a scanning electron microscopy (SEM) on (S-3400 SEM, Hitachi Ltd., Ibaraki, Japan). The voltage used in the test was 5 kV.

3. Results and discussion
3.1. Effect of chemical treatment on the tensile properties of TPU/KF
Figure 1 shows the effect of various treatments on the tensile properties of TPU/KF. NaOH treatment of COMP2 decreased the tensile strength and strain; however, it slightly increased the tensile modulus. The pMDI chemical treatment of COMP3 resulted in a slight increase in the tensile strength and modulus and a slight decrease in the strain. The tensile strength of COMP4 showed a significant increase from 33 MPa for the untreated composite (COMP1)
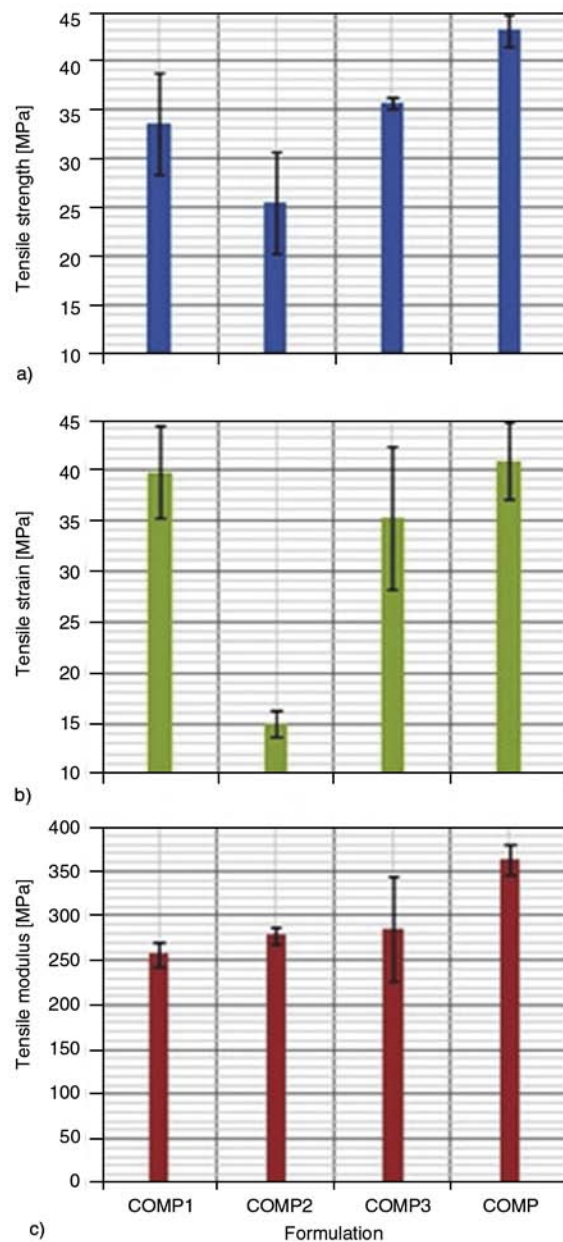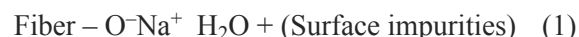

Figure 1. Effect of various treatments on the tensile properties of TPU/KF. (a) tensile strength, (b) tensile strain, (c) tensile modulus.

to a mean value of 43 MPa after treatment, which is an increase of approximately 30%. The modulus also increased from 257 MPa for the untreated composite to 364 MPa after treatment, about a 42% increase, while strain to failure increased only slightly.

In COMP1, the fibers were untreated, and the fiber bundles were still strongly bonded to each other with high stacking. Mixing the fibers with TPU led to interfacial bonding with the surface without reaching the inside of the structure of the fiber bundles. The strength of the COMP1 was most likely a result of the natural cohesion of the untreated fiber bundles.

In COMP2, the fibers were treated with NaOH, which cleaned them and provided a rougher surface; however, it softened the inter-febrillar matrix, which negatively affected the stress transfer in the fibers [12]. Alkali treatment uncovers the fibrils and gives the fibers a rough surface topography [18]. Alkali treatment also changes the fine structure of the native cellulose I to cellulose II by a process known as alkalization [18–20]. The reaction of NaOH with cellulose is shown in Equation (1). Figure 2a shows the surface of an untreated fiber. The fiber surface is smooth as a result of oils and waxes. Figure 2b shows kenaf fibers treated with 2% NaOH. It is clear that the treatment removes a certain amount of hemicellulose, lignin, wax, oils, and other impurities, and the surface becomes rougher. Similar observations were found in a previous study [21]. It has been demonstrated that TPU is not compatible with NaOH treatment [10]. NaOH treatment was used in this study to compare COMP2 with COMP4, which was treated with pMDI at the same alkali dosage (Equation (1)):

$$\text{Fiber} - \text{OH} + \text{NaOH} \rightarrow$$
$$\text{Fiber} - \text{O}^-\text{Na}^+\_\text{H}_2\text{O} + (\text{Surface impurities}) \quad (1)$$

In COMP3, the fibers were treated with pMDI. The NCO groups are believed to react with the OH groups of the cellulose; therefore, the composite exhibited better interfacial bonding between the treated fibers and the matrix. However, the increment of the tensile strength was not significant, which is attributed to the availability of other materials, such as hemicellulose, lignin, waxes, and oils, which may have prevented the full effect of the isocyanate treatment. Therefore, in the next formulation, the fibers were first treated with NaOH to remove the undesirable impurities that reduce the ability of pMDI to form effective crosslinks during the treatment of fibers.

In COMP4, the fibers were treated with NaOH, which removed undesirable materials; thus, more reactive sites (i.e., hydroxyl groups) of cellulose were revealed [12]. Then, the fibers were treated with pMDI. In general, polyurethane consists of two main components: isocyanates and polyols. The main reaction that forms polyurethane is the reaction between the isocyanate NCO groups and the OH groups of the polyols. Isocyanate represents the rigid segment while polyol represents the soft component [22]. It is believed that isocyanate played the same role when utilized as a chemical treatment for the NaOH pretreated kenaf fibers; thus, by adding isocyanate to the fibers, they became more rigid. More rigid fibers have a better ability to transfer the load to the matrix. In other words, the NCO groups could react more effectively with the OH groups after NaOH treatment because the fibers had more
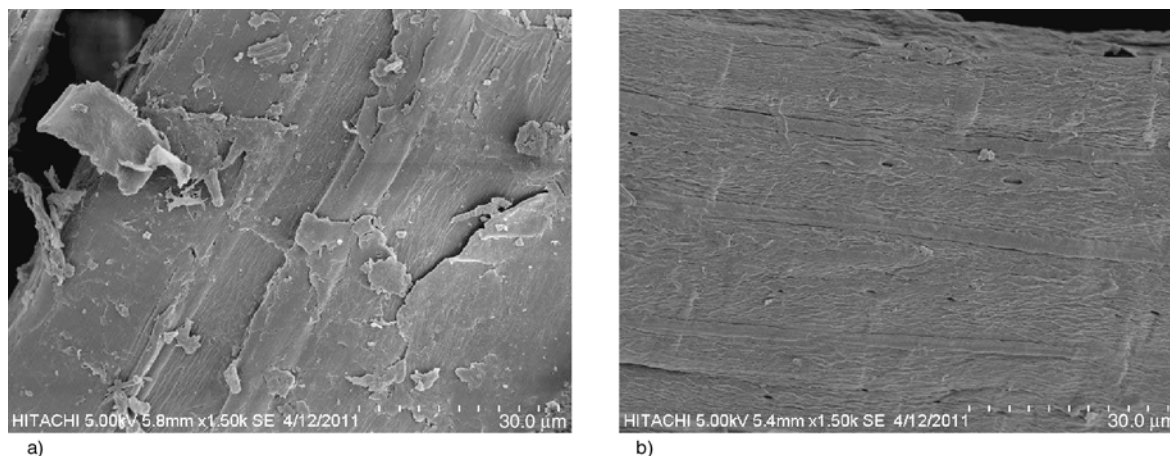
Figure 2. SEM of (a) untreated kenaf fiber and (b) kenaf fiber treated with 2% NaOH [10]
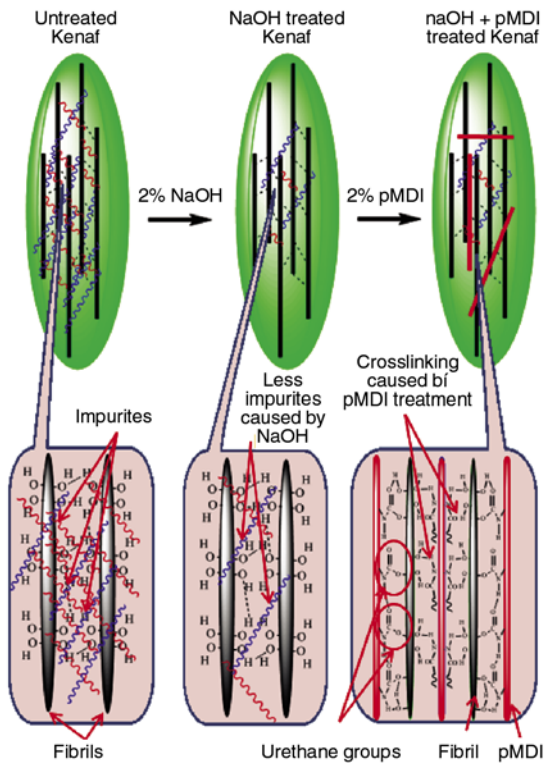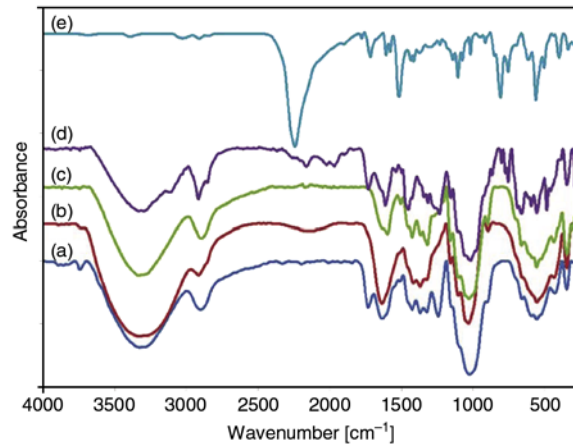
Figure 3. Schematic hypothetical chemical structure of kenaf fibers treated with 2% NaOH + 4% pMDI

Figure 4. FTIR spectra of (a) untreated kenaf fibers, (b) kenaf fibers treated with 2% NaOH, (c) kenaf fibers treated with 4% pMDI, (d) kenaf fibers treated with 2% NaOH + 4% pMDI and (e) pMDI
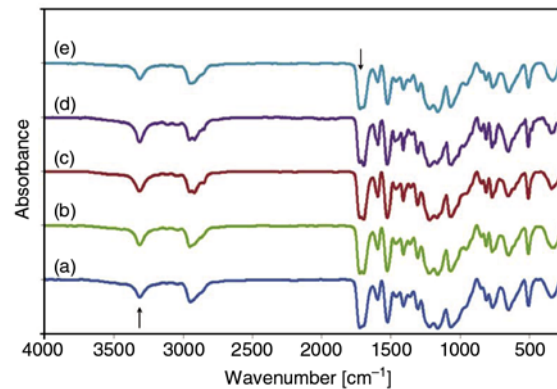
Figure 5. FTIR spectra of (a) COMP1, (b) COMP2, (c) COMP3, (d) COMP4 and (e) TPU

available reactive sites for the NCO groups. The crosslinking reconstructed the fibers and made them stronger; thus, they were able to transfer more load. In addition, the increase of strength in COMP4 could be ascribed to the increased strength of the interface between the fibers and the matrix, thereby allowing the fibers to positively contribute.

A schematic hypothetical chemical structure of the fibers treated with 2% NaOH + 4% pMDI is shown in Figure 3. In this drawing, untreated kenaf is covered with undesirable materials. However, after treatment with NaOH, the fibers were coated with fewer impurities. After treatment with pMDI, crosslinking can be observed between the OH groups of the fibrils and pMDI to form urethane groups.

3.2. FTIR spectra of treated and untreated fibers and composites

Figure 4 shows the FTIR spectra of curve (a) untreated kenaf fibers, curve (b) kenaf fibers treated with 2% NaOH, curve (c) kenaf fibers treated with 4% pMDI, curve (d) kenaf fibers treated with 2% NaOH + 4% pMDI, and curve (e) pMDI. Figure 5 shows the FTIR spectra of COMP1, COMP2, COMP3, COMP4, and pure TPU. The main IR bands

for all of the previous materials are summarized in (Table 3).

In the untreated kenaf spectra, the absorption peak was observed at approximately 1736 cm^{-1}, corresponding to the C=O stretching of hemicellulose, but this peak was almost missing in the spectrum of the 2% NaOH treated fibers, indicating the elimination of hemicelluloses and lignin as a result of alkali treatment. The elimination of this peak was observed in a previous study [23]. It is observed again at 1730 cm^{-1} in some materials after alkali treatment such as kenaf treated with 2% NaOH + 4% pMDI, TPU/KF, TPU/KF treated with 2% NaOH, TPU/KF treated with 4% pMDI, and TPU/KF treated with 2% NaOH + 4% pMDI as a result of the formation of v(C=O) of free urethane.

The strong absorption at 2250 cm^{-1} corresponds to the –N=C=O stretching of pMDI. This peak was

Table 3. Main FTIR bands of kenaf, pMDI, TPU, kenaf treated with 2% NaOH, kenaf treated with 4% pMDI, kenaf treated with 4% pMDI, kenaf treated with 2% NaOH + 4% pMDI, COMP1, COMP2, COMP3, and COMP4

Main peaks — Materials		Kenaf	pMDI	TPU	Kenaf + NaOH	Kenaf + pMDI	Kenaf + NaOH + pMDI	COMP1	COMP2	COMP3	COMP4
Chemical structure	P L										
NH[a]	3420–3200	–	–	3324	–	3351	3346	3325	3322	3325	3324
OH[a]	3300–3400	3340	–	–	3347	3313	3300	–	–	–	–
C–H[a]	3100–3000	–	3040	–	–	–	–	–	–	3060	–
CH$_2$[a] and CH$_3$[a]	3000–2800	2924	2927	2985, 2936	2931	2910	2910	2958	2961, 2935	2961, 2927	2961, 2925
–N=C=O[b]	2250	–	2250	–	–	–	–	–	–	–	–
NH[c]	1590–1650	–	1603	–	1602	1603	1603	1603	1601	1600	1598
C=O[d]	1690	1736	–	1729	–	–	–	1728	1729	1729	1730
C=O[e]	1740	–	–	1715	–	–	–	1713	1703	1705	1702
C=C[a]	1600	1647	1610, 1521	–	–	1641	–	–	–	–	–
H–N–C=O Amide II[f]	1550–1510	–	–	1530	–	–	–	1531	1532	1531	1531
CH$_2$[c] and CH$_3$[c]	1500–1300	–	–	–	–	1428, 1323	1426, 1321	–	–	1415	1414, 1312
C–O[a]	1300–1000	1042	–	–	1044	1040	1038	1075	1078	1076	1076

P L; peak location [cm^{-1}], [a]stretching, [b]isocyanate, [c]bending, [d]non-bonded urethane stretching, [e]associated urethane, [f]combined motion

almost missing in the spectrum of the pMDI treated fibers (Figure 4) and composites (Figure 5), which confirms that presence of the urethane group formed between kenaf and pMDI in pMDI chemically treated fibers and between pMDI chemically treated fibers and TPU in TPU/KF. The elimination of the peak at 2250 cm^{-1} indicating –N=C=O stretching of pMDI, with a corresponding increase in the peak at 1730 cm^{-1}, mentioned in the previous paragraph, suggests the formation of carbamate esters as a result of the reaction between –N=C=O and OH [24].

The following observations were made for untreated kenaf, kenaf treated with 2% NaOH, kenaf treated with 4% pMDI, and kenaf treated with 2% NaOH + 4% pMDI. Untreated kenaf and kenaf treated with 2% NaOH have alcoholic O–H stretching absorptions at approximately 3340 cm^{-1}. However, kenaf treated with 4% pMDI and kenaf treated with 2% NaOH + 4% pMDI have overlapping signals of alcoholic O–H stretching with H-bonded absorption and N–H stretching with H-bonded absorption at approximately 3340 cm^{-1}.

TPU, TPU/KF, TPU/KF treated with 2% NaOH, TPU/KF treated with 4% pMDI, and TPU/KF treated with 2% NaOH + 4% pMDI were studied. All of these samples include urethane N–H stretching and N–H bending absorptions at approximately 3324 and 1530 cm^{-1}, respectively, and C=O stretching

absorptions at approximately 1701 cm^{-1}. The stretching absorption of an ether linkage (C–O–C) was observed at approximately 1040 cm^{-1}. In addition, absorption bands arising from –CH$_2$ stretching were found between 2910 and 2985 cm^{-1}, and bending –CH$_2$ band were observed at approximately 1428 and 1323 cm^{-1}.

The main factor contributing to the mechanical properties of the natural fiber composites is H-bonding. It causes shifts and differences in the intensities of the absorptions; all of these shifts are shown in Figure 6. For example, the stretching H-bonding of NH at approximately 3324 cm^{-1} [25] showed the highest absorption intensity from TPU/KF treated with 2% NaOH + 4% pMDI and the lowest absorp-
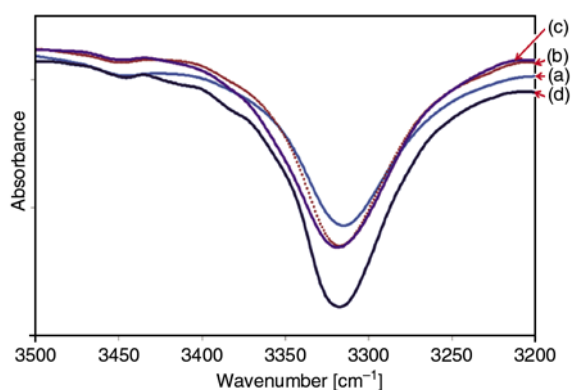
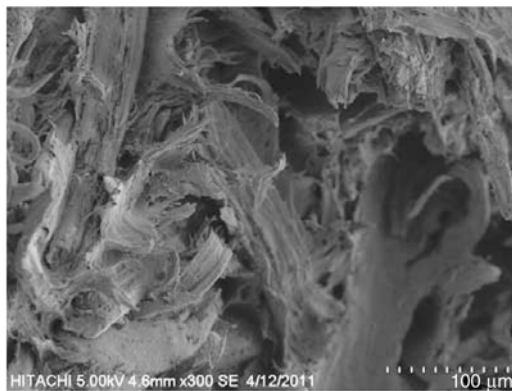**Figure 6.** FTIR spectra in the range between 3500 and 3200 cm^{-1} for (a) COMP1, (b) COMP2, (c) COMP3 and (d) COMP4

tion intensity from untreated TPU/KF, which indicates that the H-bonding increased in the following order: TPU/KF treated with 2% NaOH + 4% pMDI, TPU/KF treated with 4% pMDI, TPU/KF treated 2% NaOH and untreated TPU/KF.
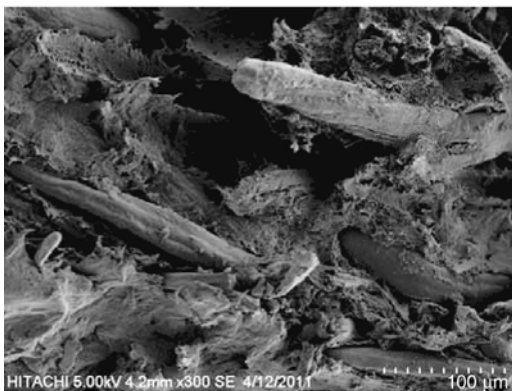
TPU/KF treated with 2% NaOH + 4% pMDI yielded the highest H-bonding and thus, the best tensile properties because undesirable materials were removed from the kenaf by the NaOH treatment, and then the fibers were treated with pMDI to create chemical crosslinking between the fiber bundles. By following these steps, the degree of polymerization might have increased. In addition, urethane groups were formed, which made the fibers capable of transferring greater loads. Therefore, the tensile properties were enhanced.

3.3. SEM of the fracture surface of tensile specimens

Both fiber breakage and fiber pull-out are shown on the fracture surface of the untreated TPU/KF (Figure 7a), which indicates that the fiber-matrix adhesion is quite good. Figure 7b shows the fracture surface of TPU/KF treated with 2% NaOH, in which
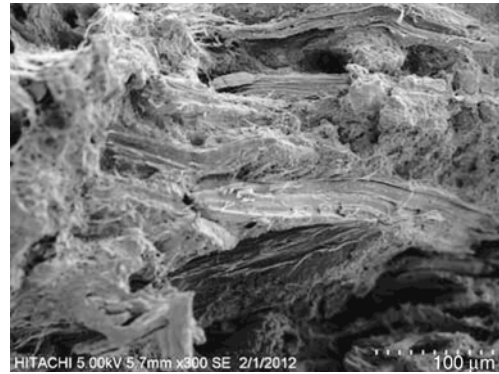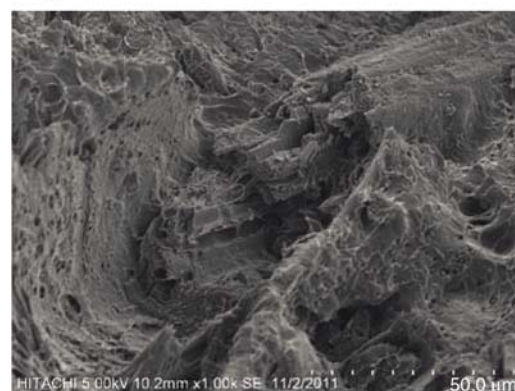

Figure 8. SEM of TPU/KF treated with 4% pMDI chemical treatment

poor fiber-matrix adhesion is confirmed by the presence of gaps between the fibers and the matrix and fiber pull-outs.

Treatment of TPU/KF with 4% pMDI also led to a mix of fiber breakage and pull-outs Figure 8. However, when TPU/KF was treated with 2% NaOH + 4% pMDI, fiber breakage became dominant, as shown in Figure 9a, which confirms the strong fiber-matrix adhesion. Furthermore, no gaps were seen between the fibers and the matrix in Figure 9b, which is a high magnification image of Figure 9a,

Figure 7. SEM of (a) untreated TPU/KF and (b) TPU/KF treated with 2% NaOH [10]

Figure 9. SEM of TPU/KF treated with 2% NaOH + 4% pMDI; (a) low magnification, (b) high magnification

indicating better wetting and adhesion between the fibers and matrix.

4. Conclusions

While the treatment of composites with NaOH alone led to a deterioration of their properties, pMDI chemical treatment increased the properties of the composite only slightly. However, the treatment of kenaf fibers with NaOH followed by pMDI had a significant effect on the composite, which was evident in the 30% increase in the tensile strength and approximately 42% increase in the tensile modulus. The FTIR spectra also provided evidence that the NCO groups of pMDI covalently linked with the OH groups of kenaf fibers and that there was strong H-bonding in the composite treated with NaOH + pMDI. The SEM morphological study shows that the composites treated with NaOH + pMDI have better fiber-matrix adhesion and wettability.

References

[1] Bachtiar D., Sapuan S. M., Hamdan M. M.: The effect of alkaline treatment on tensile properties of sugar palm fibre reinforced epoxy composites. Materials and Design, **29**, 1285–1290 (2008).
DOI: 10.1016/j.matdes.2007.09.006

[2] Bachtiar D., Salit M. S., Zainudin E., Abdan K., Mohd Dahlan K. Z. H.: Effects of alkaline treatment and a compatibilizing agent on tensile properties of sugar palm fibre-reinforced high impact polystyrene composites. BioResources, **6**, 4815–4823 (2011).

[3] Viet Cao X., Ismail H., Rashid A. A., Takeichi T., Vo-Huu T.: Mechanical properties and water absorption of kenaf powder filled recycled high density polyethylene/natural rubber biocomposites using MAPE as a compatibilizer. BioResources, **6**, 3260–3271 (2011).

[4] Wirawan R., Sapuan S. M., Yunus R., Abdan K.: Properties of sugarcane bagasse/poly(vinyl chloride) composites after various treatments. Journal of Composite Materials, **45**, 1667–1674 (2011).
DOI: 10.1177/0021998310385030

[5] Nosbi N., Akil H. M., Mohd Ishak Z. A., Abu Baker A.: Behavior of kenaf fibers after immersion in several water conditions. BioResources, **6**, 950–960 (2011).

[6] Paridah M. T., Basher A. B., Syeed O. A., Ahmed Z.: Retting process of some bast plant fibres and its effect on fibre quality: A review. BioResources, **6**, 5260–5281 (2011).

[7] Ibrahim M., Wan Daud W. R., Law K-N.: Comparative properties of soda pulps from stalk, bast, and core of Malaysian grown kenaf. BioResources, **6**, 5074–5085 (2011).

[8] El-Shekeil Y. A., Salit M. S., Abdan K., Zainudin E. S.: Development of a new kenaf bast fiber-reinforced thermoplastic polyurethane composite. BioResources, **6**, 4662–4672 (2011).

[9] Rashdi A. A. A., Sapuan S. M., Ahmad M., Abdan K. B.: Review of kenaf fiber reinforced polymer composites. Polimery, **54**, 775–788 (2009).

[10] El-Shekeil Y. A., Sapuan S. M., Khalina A., Zainudin E. S., Al-Shuja'a O. M.: Effect of alkali treatment on mechanical and thermal properties of Kenaf fiber-reinforced thermoplastic polyurethane composite. Journal of Thermal Analysis and Calorimetry, **109**, 1435–1443 (2012).
DOI: 10.1007/s10973-012-2258-x

[11] El-Shekeil Y. A., Sapuan S. M., Khalina A., Zainudin E. S., Al-Shuja'a O. M.: Effect of isocyanate additive on mechanical and thermal properties of kenaf fiber-reinforced thermoplastic polyurethane composite. Bulletin of Material Science, in press (2012).

[12] Thomas S., Pothan L.: Natural fibre reinforced polymer composites: From macro to nanoscale. Old City Publishing, Pothen (2009).

[13] Chen F., Liu L. S., Cooke P. H., Hicks K. B., Zhang J.: Performance enhancement of poly(lactic acid) and sugar beet pulp composites by improving interfacial adhesion and penetration. Industrial and Engineering Chemistry Research, **47**, 8667–8675 (2008).
DOI: 10.1021/ie800930j

[14] Jiang L., Chen F., Qian J., Huang J., Wolcott M., Liu L., Zhang J.: Reinforcing and toughening effects of bamboo pulp fiber on poly(3-hydroxybutyrate-*co*-3-hydroxyvalerate) fiber composites. Industrial and Engineering Chemistry Research, **49**, 572–577 (2009).
DOI: 10.1021/ie900953z

[15] Sahoo S., Misra M., Mohanty A. K.: Enhanced properties of lignin-based biodegradable polymer composites using injection moulding process. Composites Part A: Applied Science and Manufacturing, **42**, 1710–1718 (2011).
DOI: 10.1016/j.compositesa.2011.07.025

[16] Wang Z., Wang E., Zhang S., Wang Z., Ren Y.: Effects of cross-linking on mechanical and physical properties of agricultural residues/recycled thermoplastics composites. Industrial Crops and Products, **29**, 133–138 (2009).
DOI: 10.1016/j.indcrop.2008.04.016

[17] El-Shekeil Y. A., Sapuan S. M., Abdan K., Zainudin E. S.: Influence of fiber content on the mechanical and thermal properties of Kenaf fiber reinforced thermoplastic polyurethane composites. Materials and Design, **40**, 299–303 (2012).
DOI: 10.1016/j.matdes.2012.04.003

[18] Mwaikambo L. Y., Ansell M. P.: Chemical modification of hemp, sisal, jute, and kapok fibers by alkalization. Journal of Applied Polymer Science, **84**, 2222–2234 (2002).
DOI: 10.1002/app.10460

[19] John M. J., Anandjiwala R. D.: Recent developments in chemical modification and characterization of natural fiber-reinforced composites. Polymer Composites, **29**, 187–207 (2008).
DOI: 10.1002/pc.20461

[20] Nevell T. P., Zeronian S. H.: Cellulose chemistry and its applications. Ellis Horwood, Chichester (1985).

[21] Liu X. Y., Dai G. C.: Surface modification and micromechanical properties of jute fiber mat reinforced polypropylene composites. Express Polymer Letters, **1**, 299–307 (2007).
DOI: 10.3144/expresspolymlett.2007.43

[22] Thomson T: Polyurethanes as specialty chemicals: Principles and applications. CRC press, West Newbury (2004).

[23] Fávaro S. L., Ganzerli T. A., de Carvalho Neto A. G. V., da Silva O. R. R. F., Radovanovic E.: Chemical, morphological and mechanical analysis of sisal fiber-reinforced recycled high-density polyethylene composites. Express Polymer Letters, **4**, 465–473 (2010).
DOI: 10.3144/expresspolymlett.2010.59

[24] Karmarkar A., Chauhan S. S., Modak J. M., Chanda M.: Mechanical properties of wood–fiber reinforced polypropylene composites: Effect of a novel compatibilizer with isocyanate functional group. Composites Part A: Applied Science and Manufacturing, **38**, 227–233 (2007).
DOI: 10.1016/j.compositesa.2006.05.005

[25] Silverstein R., Webster F.: Spectrometric identification of organic compounds. Wiley, New York (2006).